

Magnetic Properties of Surface Adsorbed Metal Adatoms and Dimers

Présentée le 29 juillet 2022

Faculté des sciences de base
Laboratoire de nanostructures superficielles
Programme doctoral en physique

pour l'obtention du grade de Docteur ès Sciences

par

Dante Philippe SBLENDORIO

Acceptée sur proposition du jury

Prof. A. Pasquarello, président du jury
Prof. H. Brune, directeur de thèse
Prof. . S. Loth, rapporteur
Prof. M. Ternes, rapporteur
Prof. O. Yazyev, rapporteur

Acknowledgements

I would like to thank my thesis advisor, Prof. Harald Brune, for providing the opportunity to continue my exploration of the fundamental mysteries of the universe in the collaborative and supportive environment that is his research group, the Laboratory of Nanostructures at Surfaces (LNS).

I would also like to thank Dr. Marina Pivetta, Dr. Stefano Rusponi, and Dr. François Patthey for their patience, understanding, guidance, and good humor in my pursuit to advance my experimental and theoretical knowledge of physics. The lectures of Dr. Stefano Rusponi were invaluable in studying the systems presented in this thesis, as were the decades of experimental experience of Dr. Marina Pivetta and Dr. François Patthey.

I would also like to express my sincere gratitude to the other members of LNS, for cultivating a pleasurable, supportive, and rewarding social and scientific environment that not only advanced my scientific perspectives but also my social understanding of the world. Specifically, I would like to thank Dr. Alberto Curcella for his support and collaborative effort throughout the entirety of my studies.

Of course, none of this thesis would have been possible without the support of my parents, siblings, and grandparents. The decisions they made, long before I was born, culminated in the opportunity for me to pursue studies in a field of my choice. I truly stand on the shoulders of their successes.

Last but not least, I would like to thank my lovely wife, Dr. Gabrielle Anne Sblendorio, for motivating me in times of doubt, having patience with my sometimes questionable decisions, offering a unique, yet soundly objective perspective, and most importantly for encouraging me to pursue a PhD in the first place.

Lausanne, 29 July 2022

D. P. S.

Abstract

This thesis investigates the magnetic properties of single atoms and dimers adsorbed on graphene and oxide decoupling layers supported by single crystal metal substrates, using scanning tunneling microscopy (STM) and spin-polarized scanning tunneling microscopy (SP-STM). The goal is twofold: to use SP-STM to further advance the understanding of the interactions that determine the magnetic stability of Dy adatoms on graphene/Ir(111) and Ho adatoms on MgO/Ag(100), and to use insights from these systems to motivate the study of new systems—mainly, IrCo heterodimers on graphene/Ir(111).

For Dy adatoms on graphene/Ir(111), the characteristic lifetime of the spin system is measured as a function of temperature and tunnel bias, probing the available magnetization reversal pathways in the energy level diagram. The necessity of including the intra-atomic exchange to correctly describe spin lifetimes is demonstrated. In addition, naturally abundant Dy isotopes possess two possible nuclear spin values. Models of both nuclear spin cases of Dy are compared, and shown to produce similar behavior in the temperature and bias ranges probed by SP-STM. Furthermore, accounting for both nuclear spin cases allows for modeling of X-ray magnetic circular dichroism (XMCD) magnetization sweeps.

For Ho adatoms on MgO/Ag(100), novel measurement protocols are used to determine the zero-field stability, and the correct ground state model. These protocols are also used to induce magnetic state reversal via Landau-Zener tunneling at avoided level crossings due to the hyperfine interaction.

Finally, the study of the IrCo heterodimer adsorbed on graphene is motivated with stability considerations derived from the studies of Dy adatoms on graphene/Ir(111) and Ho adatoms on MgO/Ag(100), in addition to calculations based on density function theory (DFT). Strategies of engineering these heterodimers using statistical growth and atomic manipulation are successfully implemented. The heterodimer is highly mobile on graphene/Ir(111) and displays geometric instability, consistent with its predicted upstanding geometry. Despite this, measurement via STM and SP-STM is demonstrated. Observations are consistent with the robust magnetic stability expected from DFT studies, but additional investigation is needed to disentangle the measurements made thus far.

Keywords: scanning tunneling microscopy, spin-polarized scanning tunneling microscopy, single atom magnets, transition metal dimers, spin dynamics, spintronics, open quantum systems, quantum computing

Résumé

Cette thèse étudie les propriétés magnétiques d'atomes isolés et de dimères adsorbés sur des couches de découplage de graphène et d'oxyde supportées par des substrats métalliques monocristallins, en utilisant la microscopie à effet tunnel (STM) et la microscopie à effet tunnel polarisée en spin (SP-STM). L'objectif est double : utiliser la SP-STM pour mieux comprendre les interactions qui déterminent la stabilité magnétique des atomes de Dy sur graphène/Ir(111) et des atomes de Ho sur MgO/Ag(100), et utiliser les connaissances acquises sur ces systèmes pour motiver l'étude de nouveaux systèmes, principalement des hétérodimères IrCo adsorbés sur graphène/Ir(111).

Pour les adatoms de Dy sur graphène/Ir(111), la durée de vie caractéristique du spin est mesurée en fonction de la température et de la tension tunnel, selon les chemins de renversement de la magnétisation disponibles dans le diagramme des niveaux d'énergie. La nécessité d'inclure l'interaction d'échange intra-atomique pour décrire correctement la durée de vie des spins est démontrée. En outre, les isotopes naturels du Dy présentent deux valeurs de spin nucléaire. Les modèles correspondant aux deux cas de spin nucléaire sont comparés, et il est démontré qu'ils produisent un comportement similaire dans les plages de température et de tension tunnel sondées par SP-STM. En outre, la prise en compte des deux cas de spin nucléaire permet de modéliser les courbes de magnétisation mesurées par dichroïsme circulaire magnétique de rayons X (XMCD).

Pour les adatoms de Ho sur MgO/Ag(100), de nouveaux protocoles de mesure sont utilisés pour déterminer la stabilité du système à champ nul et l'état fondamental correct. Ces protocoles sont également utilisés pour induire un renversement de l'état magnétique via un effet tunnel Landau-Zener aux croisements évités de niveaux d'énergie, en raison de l'interaction hyperfine.

Enfin, l'étude de l'hétérodimère IrCo adsorbé sur le graphène est motivée par des considérations sur la stabilité dérivées des études des adatoms de Dy sur graphène/Ir(111) et de Ho sur MgO/Ag(100), ainsi que des calculs basés sur la théorie de la fonctionnelle de la densité (DFT). Des stratégies d'ingénierie de ces hétérodimères utilisant la croissance statistique et la manipulation atomique sont mises en œuvre avec succès. L'hétérodimère est très mobile sur

le graphène/Ir(111) et présente une instabilité géométrique, ce qui peut refléter la géométrie verticale prédite par les calculs DFT. Malgré cela, la possibilité de mesurer ce système par STM et SP-STM est démontrée. Les premières observations sont cohérentes avec la stabilité magnétique robuste attendue des études DFT, mais des recherches supplémentaires sont nécessaires pour interpréter et confirmer les mesures effectuées jusqu'à présent.

Mots clefs : microscopie à effet tunnel, microscopie à effet tunnel à polarisation de spin, aimant à atome unique, dimères de métal de transition, dynamique de spin, spintronique, systèmes quantiques ouverts, informatique quantique

Contents

Acknowledgements	i
Abstract	iii
List of Figures	ix
List of Tables	xi
1 Introduction	1
2 Methods	5
2.1 Scanning Tunneling Microscopy	5
2.1.1 Tunneling theory	7
2.1.2 Spin-polarized tunneling theory	11
2.1.3 Atomic manipulation	13
2.1.4 Experimental apparatus	14
2.2 Modeling spin systems	15
2.2.1 Exchange interaction	16
2.2.2 Spin-orbit coupling and the Zeeman effect	18
2.2.3 Crystal field interaction	19
2.2.4 Hyperfine interaction	21
2.2.5 Spin-phonon coupling	21
2.2.6 Kondo-like spin tunneling	24
2.2.7 Quantum tunneling of magnetization	26
3 Measuring the impact of the intra-atomic exchange	29
3.1 A choice of basis	29
3.2 The characteristic lifetime τ^*	30
3.3 Distinguishing between the two models	32
3.4 Modeling the spin system	36
3.4.1 The spin Hamiltonian	36
3.4.2 Master equation	38
3.4.3 Fitting parameters	39
3.4.4 Transition rates	41
3.5 Hyperfine considerations	44
	vii

3.6	Magnetization curves	48
3.7	Outlook	54
4	The role of the hyperfine interaction in state reversal	55
4.1	Reading the magnetic state	56
4.2	A modified read protocol	58
4.3	Modeling the spin system	60
4.4	A write protocol	63
4.5	Reconciling with recent developments	64
4.6	Outlook	67
5	Engineering transition metal heterodimers	69
5.1	Theoretical motivation	69
5.2	Approaches for creation and identification	75
5.2.1	Statistical growth	76
5.2.2	Choice of metal substrate	77
5.2.3	Beyond statistical growth	77
5.2.4	Atomic manipulation	78
5.3	Species observations	79
5.3.1	Deposition of Ir alone	79
5.3.2	Deposition of Co alone	82
5.3.3	Deposition of both Co and Ir	84
5.4	Magnetic signatures	85
5.5	Outlook	87
6	Outlook	89
	Bibliography	91
	Curriculum Vitae	107

List of Figures

2.1	Essential elements of the STM	6
2.2	Tunneling across a single barrier	8
2.3	Two families of atomic manipulation	13
2.4	Direct, Orbach, and Raman phonon processes.	22
2.5	Simplified sketch of the scattering processes.	25
2.6	Real level crossing and avoided level crossing	28
3.1	Comparing 4f and 4f5d6s models	31
3.2	Reading the magnetic quantum states of Dy SAMs	33
3.3	Writing the magnetic quantum states of Dy SAMs	34
3.4	HC occupancy and electron and phonon scattering contribution	40
3.5	Transition rates of the 4f vs 4f5d6s model	42
3.6	Bias dependent transition rates of the 4f5d6s model	43
3.7	Comparing the 4f5d6s model with and without nuclear spin I	45
3.8	Extended Zeeman diagram of the $ m_{\pm 7}\rangle$ states at zero field.	46
3.9	Zero-field level crossings of the 4f5s6s model with nuclear spin I	47
3.10	Zeeman diagram of the 4f5d6s model and XMCD magnetization curve.	49
3.11	Non-zero-field level crossings of the 4f5s6s model with nuclear spin I	51
3.12	Magnetization curves of the 4f5d6s model for both nuclear spin cases $I = 0$ and $I = 5/2$	53
4.1	Level diagram comparison for the $J_z = \pm 7$ and $J_z = \pm 8$ models	56
4.2	Three phases of the read measurement protocol	57
4.3	A modified read protocol	59
4.4	Extended Zeeman diagram for the $J_z = \pm 7$ and $J_z = \pm 8$ models with nuclear spin I	62
4.5	Comparison between simplified and complete 2-phonon Raman models	66
5.1	Schematics of the adsorption site geometry of dimers on graphene	73
5.2	Deposition of Ir on graphene/Ir(111)	80
5.3	Creation of Ir ₂ dimers on graphene/Ir(111)	81
5.4	Deposition of Co on graphene/Ir(111)	83
5.5	Appearance of IrCo heterodimer on graphene/Ir(111) with a non-magnetic tip	85
5.6	Appearance of IrCo heterodimer on graphene/Ir(111) with a magnetic tip	86

List of Tables

3.1	CF Stevens Parameters for the 4f and 4f5d6s models	37
3.2	Fitting parameters used for the 4f and 4f5d6s models	39
4.1	State Preservation of the read protocol with retracted tip	58
4.2	State Preservation of the modified protocol with N tip retractions	60
4.3	CF Stevens Parameters for the $J_z = \pm 7$ and $J_z = \pm 8$ ground state model	60
4.4	Observed switching probabilities for state inversion through Landau-Zener tunneling.	64
5.1	Calculated MAEs of transition metal dimers in various configurations	72

1 Introduction

The first recorded empirical observation of magnetism is attributed to a Greek philosopher in the 6th century BCE by the name of Thales of Miletus, who noted that a magnet possesses the ability to move iron [1]. For much of human history, observations of magnetism were limited to those surrounding lodestones, or naturally magnetized pieces of magnetite. It wasn't until the 11th century CE that Chinese scientist Shen Kuo described how iron needles magnetized with a lodestone and the astronomical concept of true north could be utilized for navigational purposes [2]. Several centuries later, the English scientist William Gilbert performed experiments that led him to conclude that compasses point north because the Earth is magnetic [3]. He also made a distinction between magnetic forces and those forces caused by static electricity. This relationship between electricity and magnetism arose again in 1819 when Hans Christian Ørsted observed the movement of a compass needle when near a current carrying wire [4]. The University of Copenhagen professor was the first to link the two phenomena, and his experiment was followed by a series of discoveries by André-Marie Ampère, Carl Friedrich Gauss, Jean-Baptiste Biot and Félix Savart, and Michael Faraday that culminated in the formulation of distinct equations unifying electricity, magnetism, and optics into the field of electromagnetism by James Clerk Maxwell [5].

The groundbreaking electromagnetic experiments of the 19th century, and the resulting formulation of Maxwell's equations, offered insights into the material origin of magnetism by introducing the idea, among others, that circular currents induce magnetic moments. The proliferation of electrification and the prevalent use of electromagnets allowed for more widespread experimentation on the behavior of magnetic materials as a function of applied magnetic fields and temperatures. This led to discoveries such as the spontaneous magnetization of ferromagnetic materials, and the concepts of anisotropy, susceptibility, remanance and coercivity, and Curie temperature. In 1906, Pierre-Ernest Weiss proposed a model of ferromagnetism, where a macroscopic ferromagnet consisted of microscopic magnetic domains, each comprised of a large number of magnetic moments [6]. Each moment "feels" the effect of its neighbors, thus aligning the moments and creating a ubiquitous field throughout the material. This model was consistent with the idea proposed by Ampère following the Ørsted

experiment, whereby circular currents within a material create magnetic moments [7]. The Weiss model successfully explained some of the experimental observations made at the time, but failed to justify the exact origin of these magnetic moments. It wasn't until the formulation of quantum mechanics that this was fully understood.

The foundations of quantum mechanics were established by Max Planck in 1900, when he introduced his quantum of action to describe the black-body radiation spectrum [8]. Early atomic models failed to accurately predict the energies of the spectral lines of hydrogen until Niels Bohr utilized Planck's quantum of action, quantizing the possible values of energy and angular momentum for electrons surrounding a positively charged nucleus [9]. In 1922, the Stern-Gerlach experiment demonstrated the first direct evidence of this quantization of angular momentum and the spin-1/2 nature of electrons, from which atomic magnetic moments are wholly derived [10]. In the following years, Erwin Schrödinger, Werner Heisenberg, and Paul Dirac cemented the modern theory of quantum mechanics, further solidifying the atomic origin of magnetism [11–13].

In the decades that followed, attempts to explain specific phenomena of macroscopic magnetism utilized models founded upon quantum theory such as those put forth by Heisenberg (1928), Stoner (1948), Anderson (1961) and Hubbard (1963) [14–17]. Two approaches were employed to describe the $3d$ and $4f$ valence shells of magnetic atoms: a localized or correlated electron behavior and an itinerant, band-like behavior. Both approaches found success in different macroscopic systems, reflecting the competition that occurs between band-like and localized magnetism. These models serve as the cornerstones of the modern theory of magnetism, and are just as relevant now as they were when first published.

Beginning in the second half of the 20th century, fundamental research in magnetism was largely driven by technological innovation. The proliferation of computation and magnetic-based memory technologies provided ample opportunity for progress in the study of magnetic systems and the experimental techniques used to do so. Bulk techniques like neutron diffraction dominated the earlier decades when bulk magnetism was most prevalent in technological applications. As functional devices approached nanoscales, the high surface sensitivity of electron, X-ray, and optical methods supplanted bulk techniques. Undoubtedly, these approaches have ushered in the current age of spintronics and quantum computation. However, their ensemble nature—measuring a large number of spins simultaneously, offers only so much insight into the properties at the nanoscale. For ensembles composed of non-interacting well-defined units, such as single atoms or mono-dispersed clusters, these measurements reveal the characteristic properties of each individual nanostructure. But for systems composed of a multitude of different species, complementary techniques capable of nanometer resolution on surfaces provide the higher specificity that eludes ensemble measurements. Scanning tunneling microscopy (STM) and spin polarized scanning tunneling microscopy (SP-STM) are two such techniques, capable of not only measuring sub-nanometer spatial resolutions, but also extracting quantitative magnetic information from nanoscale spin systems, as the past two decades of research has demonstrated. These techniques have been used to study

thin films, nanostripes, nanowires, and magnetic vortex cores [18–21], as well as nanoislands and clusters [22–30], revealing properties such as magnetic domain size, magnetic ordering and electronic structure, and magnetization dynamics as a function of size, shape, and temperature. These studies highlight the unique properties that arise at the nanoscale. As the size of functional magnetic devices approach just a few atoms, the magnetic properties are increasingly sensitive to differences in charge state, adsorption site and geometry. STM and SP-STM allow subtle distinction between subspecies such as these. Via inelastic electron tunneling spectroscopy (IETS), STM has been used to detect changes in the magnetic state of individual adatoms [31], measure inter-atomic exchange coupling in structures composed of less than 10 atoms [32, 33], determine magnetic ground state and anisotropy energy of adatoms and clusters [34–36], and more recently, directly measure the intra-atomic exchange coupling in rare-earths [37]. Furthermore, SP-STM has successfully measured magnetization curves on single adatoms [38], ascertained spin relaxation times [39–42], and directly accessed and manipulated spin states [43–47]. Thus, these tools are ideal complements to ensemble techniques in acquiring magnetic information of spin systems.

In 2016, the first single atom magnets (SAMs) were discovered with X-ray magnetic circular dichroism (XMCD). Both Dy atoms on graphene/Ir(111) [48] and Ho atoms on MgO/Ag(100) [49] exhibited magnetic remanence, indicating magnetic lifetimes of greater than 10^3 seconds at 2.5 K and 10 K, respectively. These results warranted further investigation by local techniques in order to confirm, and discern the origin of, their remarkable stability. For the Ho system, reading and writing of the Ho magnetic state via SP-STM was performed in 2017 [47]. Following this, investigations of the thermal and magnetic field stability in 2018 observed a coercive field of more than 8 T and magnetic bistability at 35 K [42]. Measurements of the Zeeman splitting as a function of applied field estimate a magnetic moment of $(9.5 \pm 1.1) \mu_B$ [42]. This is consistent with previous STM electron spin resonance (ESR) measurements of the stray field seen by Fe adatoms placed in close proximity to the Ho moment of $(10.1 \pm 0.1) \mu_B$, but much larger than the XMCD results [47]. Despite these measurements, the magnetic ground state at zero field remains undetermined, but constrained to either $J_z = \pm 7$ or $J_z = \pm 8$ [42]. For the Dy system, the XMCD results are consistent with a $4f^{10}$ occupation and a $J = 8$ total angular moment, identical to Dy in the gas phase. They also indicate a $J_z = \pm 7$ out-of-plane magnetic ground state [48, 50]. However, in all XMCD measurements, photon-induced secondary electrons may significantly limit the lifetimes [48–53]. Thus, the resulting measurement represents a lower-bound estimate. SP-STM does not rely on high-energy photons, and therefore can reveal much longer lifetimes, as shown in the case of the Ho system [42, 47]. In light of these observations, the goal of this thesis is twofold: to use SP-STM to further advance our understanding of the interactions that determine the magnetic stability of these SAMs, and to use insights from these systems to search for new systems exhibiting similar, if not more exceptional, magnetic characteristics. In light of these goals, the structure of this thesis is as follows:

- **Chapter 1** is the present Chapter, and introduces the greater scientific framework in which the contents of this thesis fit, and enumerates the structure of said thesis.

- **Chapter 2** reviews the experimental techniques, mainly STM and SP-STM used to study the SAM systems in this thesis. The methods used to prepare samples of these systems and the STM tips are also described. In addition to the experimental techniques, the theoretical foundations upon which models of these systems are constructed are also introduced. The intra-atomic exchange interaction, the Zeeman interaction, the spin-orbit interaction, the hyperfine interaction, the interaction of orbital shells within a crystal field, the spin-phonon interaction, and Kondo-like spin tunneling are all described.
- **Chapter 3** presents the results of our study of the spin dynamics of Dy adatoms on graphene/Ir(111). Two models to explain the experimental trends are proposed: the first considering the $4f$ shell and an unpolarized external $5d6s$ shell, while the second considers the $4f$ shell and a polarized external $5d6s$ shell. The latter of which possesses a non-zero intra-atomic exchange interaction between the shells. The magnetic relaxation processes and implications of each model are discussed. In addition, the effect of the hyperfine interaction is considered in light of previously measured XMCD magnetic hysteresis loops.
- **Chapter 4** addresses the stability of Ho adatoms on MgO/Ag(100) at low magnetic field. A measurement scheme is presented that allows for the determination of the systems magnetic ground state, as well controllable state switching via the stray magnetic field of the SP-STM tip. The implications for previously proposed level schemes are discussed.
- **Chapter 5** investigates the formation of Ir-Co heterodimers on graphene/Ir(111) by means of conventional statistical growth and via atomic manipulation. The Ir-Co heterodimer is predicted to be upstanding, with the Co atom sitting closer to the graphene, and adsorbed in the 6-fold coordinated hollow site. An extremely high magnetic anisotropy energy (MAE) of 204 meV, along the dimer axis, is also predicted, making it a promising candidate for study via SP-STM.
- **Chapter 6** summarizes the work done in this thesis and presents a roadmap for future work.

2 Methods

As discussed in the Introduction, STM and SP-STM are excellent complements to ensemble techniques to discern magnetic information from single spins on surfaces. These are the primary methods of study used in this thesis. The experimental insights that these techniques offer are instructive only in the context of models of these systems. The relevant interactions for a given spin system are best formulated by a spin Hamiltonian, where different terms express the interaction of the spin with the surrounding environment. These interactions ultimately determine the magnetic characteristics of the system, and therefore, inform the search for novel systems with desired properties. Despite this, it is typically not trivial to disentangle the different interactions with one experimental technique alone. Thus, where necessary, XMCD data complements SP-STM results to provide further robustness to the proposed models.

The first part of this chapter briefly reviews the capabilities of STM and SP-STM. A few models of electron tunneling are discussed, with emphasis on the information that can be derived from these models. Following this, descriptions of the tip and samples used in this thesis are given. In the second part, the relevant terms of the spin Hamiltonian that determine the magnetic states of single ions are presented. Rates are derived for the perturbation terms used to model spin dynamics.

2.1 Scanning Tunneling Microscopy

The implications of the quantum theory put forth in the beginning of the 20th century were profound. Perhaps one of the more counter-intuitive phenomenon predicted by the theory is that of quantum tunneling, whereby a particle impinging a potential barrier can in fact cross it, even with a kinetic energy lower than the potential barrier itself. This classically forbidden phenomenon enables isotopes to undergo decay, nuclei to fuse in stars, and like many phenomena in physics, experimental applications to be designed upon. The scanning tunneling microscope is one such application—relying on the tunneling of electrons through a vacuum gap between a sharp conductive tip and sample to map the surface with sub-

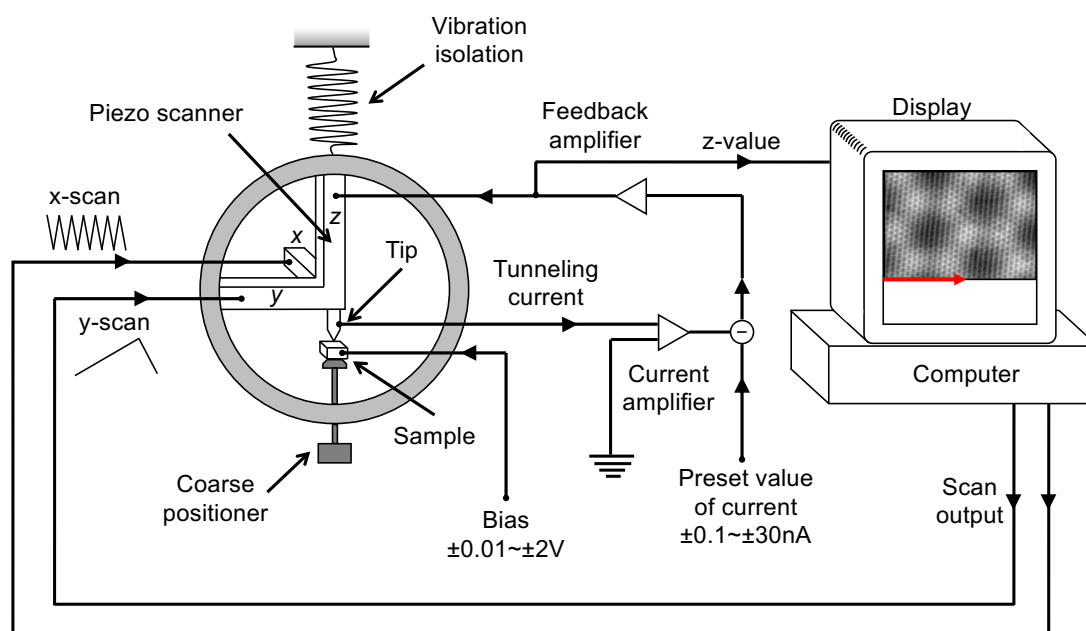


Figure 2.1: **Essential elements of the STM.** A reproduction of the schematic published in C.J. Chen's *Introduction to Scanning Tunneling Microscopy* in 1993 [57]. An induced tunnel current occurs between the tip and sample when a bias voltage is applied. Waveforms injected into the x and y piezos produce a raster scan motion of the tip. A feedback loop changes the z-value to maintain the set current. By recording the z-value at each (x,y) point, a contour image is created (pictured in the Display).

nanometer resolution. This technique was first successfully implemented by Binnig, Rohrer, Gerber, and Weibel in their 1982 paper, *Surface Studies by Scanning Tunneling Microscopy*, where they resolved monoatomic steps and surface reconstructions for the (110) surfaces of CaIrSn_4 and Au [54]. The essential elements of the microscope are pictured in Figure 2.1. Their success was, in part, owed to the implementation of a very similar instrument a decade before, known as the topografiner [55, 56].

In an ultra-high vacuum (UHV) environment, a conductive tip is attached to a piezodriven consisting of piezoelectric transducers that expand or contract with an applied bias. The piezos are positioned to allow 3 dimensional movement of the tip on the nanometer scale. A coarse positioner and the z piezo adjusts the tip-sample distance to within a few hundred picometers (z direction in Figure 2.1). The overlap of the tip and sample wavefunctions produces a tunnel conductance, such that when a tunnel bias is applied to the junction, a net tunnel current flows between tip and sample. By setting a value of the current, and implementing a feedback loop on the z piezo, the position of the tip is changed to maintain the set current. To do so, the feedback loop has a current-to-voltage amplifier. The difference of the logarithm of the measured current and the logarithm of the set current is an error signal that is proportional to the change in distance. This signal is integrated with a given time constant, then amplified and sent to the z piezo to move the tip. Applying a sawtooth voltage waveform to the x piezo

and a ramp voltage waveform to the y direction produces tip motion resembling that of a raster scan in the xy plane. Recording the z -value as the scan executes results in a topographic image of the surface (pictured in the Display).

The image consists of a z -value for each (x,y) point representing a constant-current surface. This can be better visualized as a greyscale image (or any other colormap) where brighter points indicate higher z -values and darker points indicate lower z -values. Typically, nanometers (nm) are used for the dimensions of x and y , and picometers (pm) for z . At these scales, the performance of the STM is heavily dependent on its isolation from any source of vibration within the local environment. Without this dampening, achieving stable scanning conditions is not possible, as evidenced by the earlier work on the topografiner [56].

Despite being implemented 40 years ago, the fundamental design of the STM has basically remained the same. Of course, modifications can be made to improve the stability and resolution of the images, such as operating below room temperatures or within an anechoic chamber, or to expand the measurement capabilities, such as using a magnetic tip, or implementing variable magnetic field or temperature conditions. The ensuing decades saw an expansion of the STMs capabilities into a larger family of scanning probe microscopies (SPMs) that drove interest from the physical, biological, chemical, and material sciences all looking to tour the atomic landscape [58]. The large diversity of microscopy and spectroscopy techniques found applications in condensed matter physics (surface science, magnetism, superconductivity, and charge density waves), chemistry (surface reactions and electrochemistry), organic materials (molecular thin films and nanostructures), metrology, and nanotechnology (nanometer-scale functional devices and fabrication methodology) [59].

Deriving quantitative information from the STM relies on a comprehensive understanding of the phenomena it utilizes— electron tunneling. Fortunately, previous investigations into metal-oxide-metal tunnel junctions established descriptions of tunneling before the development of the STM [60–66]. These descriptions were adapted by the early STM community to advance interpretation of the observations made. A few of these illustrations are discussed, with emphasis on the insights that can be gleaned from them. An in-depth historical review of electron tunneling can be found Ref. [57].

2.1.1 Tunneling theory

The simplest description of electron tunneling considers a one-dimensional rectangular potential barrier, pictured in Figure 2.2a. A single particle with energy E and mass m , described by wavefunction $\psi(z)$, must satisfy the Schrödinger equation for the potential $U(z)$ in each region I, II, and III:

$$-\frac{\hbar^2}{2m} \frac{d^2}{dz^2} \psi(z) + U(z)\psi(z) = E\psi(z) \quad (2.1)$$

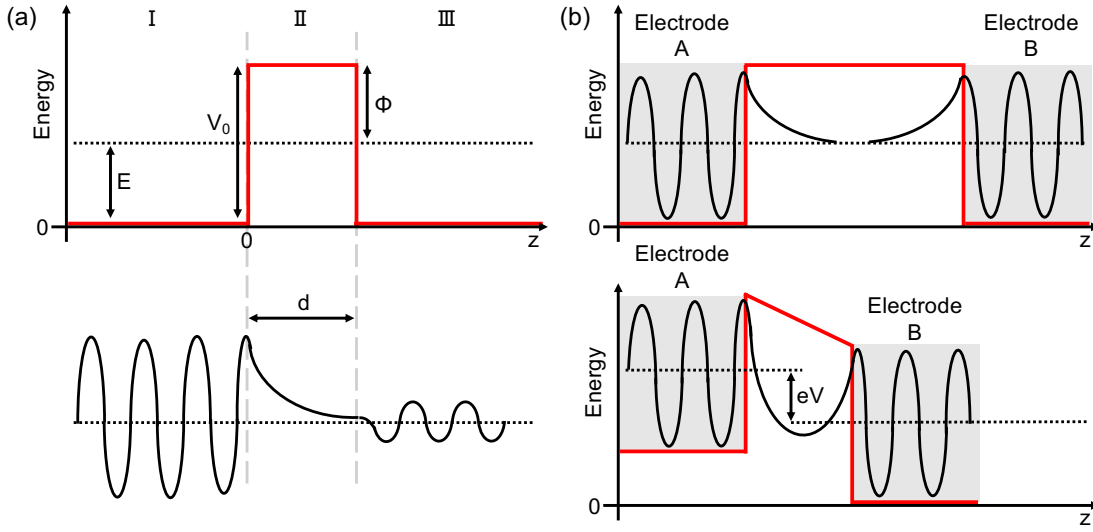


Figure 2.2: **Tunneling across a single barrier.** (a), Electron tunneling through a one-dimensional rectangular potential barrier (red) of thickness d . E is the energy of the electron, V_0 is the barrier height, and ϕ is the work function. Below, the shape of the wavefunction is illustrated for each of the three regions (I, II, III). Note the exponential decay in region II. (b), A simplified sketch of a tunnel junction. When a large gap separates the electrodes, there is no overlap of their wavefunctions and tunneling cannot occur (top). When the gap is sufficiently small and a tunnel bias V is applied, their wavefunctions overlap and tunneling can occur (bottom).

The potential $U(z) = 0$ in regions I and III and $U(z) = V_0$ in region II. Assuming the particle is incident from the left, a steady-state solution to Schrödinger's equation in each region is given by:

$$\psi(z) = \begin{cases} Ae^{ikz} + Be^{-ikz} & z < 0 \\ Ce^{\kappa z} + De^{-\kappa z} & 0 \leq z \leq d \\ Fe^{ikz} & z > d \end{cases} \quad (2.2)$$

where the wave numbers are given by $k = \sqrt{2mE/\hbar^2}$ and $\kappa = \sqrt{2m(V_0 - E)/\hbar^2}$, respectively. In region I and II, the first terms in the wavefunction describe an incident wave travelling in the $+z$ direction, while the second terms describe reflected waves at $z = 0$ and $z = d$ traveling in the $-z$ direction. In region III, no such reflection can occur. The probability of observing an electron at point z is given by the square of the wave function $|\psi(z)|^2$. Thus, there is a non-zero probability of observing the electron within region II and furthermore, penetrating the barrier in either direction is possible. A transmission coefficient ($|F|^2$ in Eq. 2.2) describing the amount of incident wavefunction that penetrates the barrier can be obtained through the imposition of a continuity condition for the wavefunction and its derivatives at $z = 0$ and $z = d$. Most relevant to the STM, this transmission coefficient is directly related to the amount of current that tunnels through the barrier as a function of thickness d . As one might expect, the

height of the barrier determines how much current is transmitted and to estimate this, a few assumptions must be made. For metal-vacuum-metal tunneling, the work function ϕ must be considered. This is defined as the difference in the energy of the highest occupied state, or the Fermi level, of the metal and the vacuum energy ($\phi = V_0 - E$ in Figure 2.2a). The effective barrier height for the electron in region II is simply ϕ . For tunneling to occur from region I to III, there must be unoccupied states available in the metal of region III. By applying a bias V between the two metals, the Fermi level in each is shifted by an energy $\pm eV/2$, opening up available states such that tunneling occurs. Assuming both metals have the same work function, the energy shift $\pm eV/2$ is small relative to the work function, $\kappa z \gg 1$, and that $A = 1$, the transmission coefficient T can be expressed as:

$$T = |F|^2 = \exp(-2\kappa z) \quad (2.3)$$

where $\kappa = \sqrt{2m\phi}/\hbar \approx 5.1 \sqrt{\phi} \text{ nm}^{-1}$, and ϕ is in eV. The metals used in STM typically have work functions around 5 eV. This implies that the current transmitted through the barrier decreases about one order of magnitude for a change in z -value of only $\Delta z = 100 \text{ pm}$. Under ideal conditions then, STM is extremely sensitive to changes in sample topography and should provide excellent resolution in the xy image plane as the majority of tunneling current originates from a singular apex atom on the tip. Hence, a relatively simple description can no doubt be illustrative.

Some of the earliest tunneling models were used to explain empirical observations such as α -decay [67], the field emission of electrons from cold metals [68], and the field-ionization of the hydrogen atom [69]. When tunneling effects were observed in metal-oxide-metal junctions [61], these models were adapted with great success. The approach, first applied by Bardeen in 1961 [70], uses time-dependent perturbation theory to obtain an expression for the tunnel current. This is done by treating each electrode wavefunction independently, such that they are approximately orthogonal. As pictured in Figure 2.2b, when the width of the barrier is large, there is no interaction between the two wavefunctions, and each decays into vacuum. This is the unperturbed state. When the width of the barrier is small, the wavefunctions begin to overlap, perturbing the system. This interaction allows electrons to transfer from a state in one electrode to a state in the other. Under second quantization formulation, the total energy of this system can be expressed as [70, 71]:

$$\mathcal{H} = \mathcal{H}_A + \mathcal{H}_B + \mathcal{H}_t \quad (2.4)$$

where \mathcal{H}_A is the Hamiltonian of the left electrode (in Figure 2.2b), \mathcal{H}_B is the Hamiltonian of the right electrode, and \mathcal{H}_t is the transfer Hamiltonian, which describes tunneling between the two electrodes. The terms of the individual unperturbed systems are:

$$\mathcal{H}_A = \sum_{\mu} E_{\mu} \hat{a}_{\mu}^{\dagger} \hat{a}_{\mu} \quad \mathcal{H}_B = \sum_{\nu} E_{\nu} \hat{b}_{\nu}^{\dagger} \hat{b}_{\nu} \quad (2.5)$$

where $\hat{a}_{\mu}/\hat{b}_{\nu}$ are the annihilation operators and $\hat{a}_{\mu}^{\dagger}/\hat{b}_{\nu}^{\dagger}$ are the creation operators. The indices μ

and v sum over the available states in electrode A and B, respectively. The transfer Hamiltonian is given by:

$$\mathcal{H}_t = \sum_{\mu\nu} \delta(E_\mu - E_\nu) \left[M_{\mu\nu} \hat{a}_\mu^\dagger \hat{b}_\nu + M_{\mu\nu}^* \hat{b}_\nu^\dagger \hat{a}_\mu \right] \quad (2.6)$$

where E_μ and E_ν are the energy eigenvalues of Schrödinger's equation for the unperturbed systems A and B. $M_{\mu\nu}$ is the tunnel matrix element for state μ and ν , and is expressed as:

$$M_{\mu\nu} = \frac{-\hbar^2}{2m} \int_{\Sigma} \left(\chi_\mu^* \nabla \psi_\nu - \psi_\nu \nabla \chi_\mu^* \right) \cdot d\mathbf{S} \quad (2.7)$$

where ψ_μ and χ_ν are the wavefunctions describing electrode A and B and the integrand is known as the current density operator. Σ is any separation surface defined between the two electrodes. The choice of the separation surface does not change the result of the integral appreciably. Notice that information about the potential barrier is not explicitly stated. Rather, only information of the two wavefunction, and their derivatives, on any separation surface is needed. How these wavefunctions are treated determines the accuracy of Bardeen's formalism. ψ_μ and χ_ν are not necessarily the wavefunctions of the unperturbed Hamiltonian $\mathcal{H}_A + \mathcal{H}_B$ (although this is what Bardeen initially assumed), but can be corrected for distortions that occur in the potentials of each electrode when the distance between them is small (Figure 2.2b, lower) [57]. The form of each wavefunction can be chosen based on the shape and composition of each electrode. For the metal-oxide-metal junctions in question, Bardeen assumes a generalized wavefunction that exponentially decays within the barrier [70]. Regardless of this choice, Equation 2.6 is clearly a tunneling process: the first term annihilates a state in electrode B and creates a state of the same energy in electrode A, while the second term annihilates a state in electrode A and creates a state of the same energy in electrode B. The delta function $\delta(E_\mu - E_\nu)$ ensures energy conservation during the tunneling process. Also of note, due to the orthogonality of wavefunctions ψ_μ and χ_ν , a basis for \mathcal{H} must include all wavefunctions of electrode A and electrode B. Under this formalism, Bardeen showed that in the limit of low tunnel biases, the current is given by:

$$I = \frac{2\pi e^2}{\hbar} V |M|^2 \rho_B \rho_A \quad (2.8)$$

where M are the matrix elements summed over the indices μ and ν and ρ_B and ρ_A are the densities of state of the electrodes B and A at their respective Fermi level E_F . This also assumed that the densities of state are relatively constant in the energy range probed. Thus, Bardeen's model provides a better understanding of the tunneling process. The current is intimately linked to the density of states of both the electrodes, which in the case of STM correspond to the tip and the sample. Therefore, the changes in recorded z -values are the convolution of topography, or actual distance between tip and surface, and the density of states of both tip and sample at the Fermi level.

As mentioned, the form of the chosen wavefunctions is integral to the form of Equation 2.8,

and therefore, the interpretation of the constant-current image. While the statement in the previous paragraph linking the z -value and density of states is true in the context of Equation 2.8, a more nuanced interpretation can be made by choosing different wavefunction forms. For example, Tersoff and Hamann adapted Bardeen's method and assumed a spherically symmetric tip with an s -type tip wavefunction [72, 73]. With this assumption, the STM images represent countour maps of constant-surface local density of states at the Fermi level, but evaluated at the center of curvature of the tip. This also allows for a relaxation of the assumption of a constant density of states within the region of energy probed, and therefore accounts for changes in the DOS as a function of energy. This is particularly relevant when performing spectroscopy measurements with STM, which measure changes in current with respect to changes in tunnel bias. Later, Chen explored d -type tip wavefunctions to explain the higher STM resolutions observed that could not be explained with s -type wavefunctions [74]. In this picture, the equilibrium position of the tip throughout the STM image represents the derivatives of the wavefunction of the sample, which exhibit a much stronger atomic corrugation, and result in a clearer image of the atomic positions. The result of Tersoff and Hamann can be further generalized to capture the following relationship for the tunneling current in STMs:

$$I \propto \int_0^{eV} \rho_T(\pm eV \mp E) \rho_S(E) T(E, eV) dE \quad (2.9)$$

where ρ_T and ρ_S are the local density of states of tip and sample, and the transmission coefficient $T(E, eV)$ contains the tunnel matrix elements and therefore the exponential dependence on distance [57, 75]. All energies in Equation 2.9 are taken with respect to the Fermi level E_F . It is clear that the tunneling current is exponentially dependent upon the tip-sample distance, but also dependent on the density of states of both the tip and sample. By varying the tunnel bias (*i.e.*, measuring $dI/dV(V)$), the local density of states of both the tip and sample can be probed. This is the basis of spectroscopy measurements with STM, where any local vibrational, rotational, or spin excitations present in the tunnel junction may produce a change in tunnel conductance. As we shall see, the dependencies of Equation 2.9 that hold for non-magnetic tip also hold true for magnetic tips, where the density of states of *each* spin population must be considered.

2.1.2 Spin-polarized tunneling theory

To extend Bardeen's original approach to cases when either the tip or sample is magnetic, the wavefunctions are replaced with spinors of the general form [75–77]:

$$\Psi = \begin{pmatrix} \psi_{\mu\uparrow}(\mathbf{r}) \\ \psi_{\mu\downarrow}(\mathbf{r}) \end{pmatrix} e^{-iE_{\mu}t/\hbar} \quad (2.10)$$

Two spin states are described, spin up and spin down. As a result of the two states, the potentials of the tip and sample each now take the form of a 2×2 matrix with components

corresponding to each possible two component spin orientation: up-up $U_{\uparrow\uparrow}$, up-down $U_{\uparrow\downarrow}$, down-down $U_{\downarrow\downarrow}$, and down-up $U_{\downarrow\uparrow}$. To ensure diagonalization, a coordinate transformation consisting of a rotation of angle θ is made to express the surface potentials in the reference frame of the tip $U^S \rightarrow U(\theta)U^T$. A set of matrix elements exists for each potential:

$$M_{\nu\sigma,\mu\sigma} = \langle \psi_{\nu\sigma}^T | U_{\sigma\sigma}^T | \psi_{\mu\sigma}^S \rangle \quad (2.11)$$

where $\sigma = \uparrow, \downarrow$. For example, for $U_{\uparrow\uparrow}$, the tunnel matrix elements are given by:

$$M_{\mu\uparrow\nu\uparrow} = \frac{-\hbar^2}{2m} \int_{\Sigma} (\chi_{\mu\uparrow}^* \nabla \psi_{\nu\uparrow} - \psi_{\nu\uparrow} \nabla \chi_{\mu\uparrow}^*) \cdot d\mathbf{S} \quad (2.12)$$

As expected, Equation 2.12 is identical to Equation 2.7, except the wavefunctions are replaced with their spin-up components. It follows that the tunnel current consists of 4 spin-dependent components:

$$I = \frac{2\pi e^2}{\hbar} V \left(\rho_{\uparrow}^T \rho_{\uparrow}^S |M_{\uparrow\uparrow}|^2 + \rho_{\uparrow}^T \rho_{\downarrow}^S |M_{\uparrow\downarrow}|^2 + \rho_{\downarrow}^T \rho_{\uparrow}^S |M_{\downarrow\uparrow}|^2 + \rho_{\downarrow}^T \rho_{\downarrow}^S |M_{\downarrow\downarrow}|^2 \right) \quad (2.13)$$

where $\rho_{\uparrow,\downarrow}^{T,S}$ are the spin-dependent densities of states for the tip and sample. This equation can be simplified by defining the following quantities:

$$\rho_T = \rho_{\uparrow}^T + \rho_{\downarrow}^T, \quad \rho_S = \rho_{\uparrow}^S + \rho_{\downarrow}^S, \quad \mu_T = \rho_{\uparrow}^T - \rho_{\downarrow}^T, \quad \mu_S = \rho_{\uparrow}^S - \rho_{\downarrow}^S, \quad (2.14)$$

and introducing the tip and sample polarizations:

$$P_T = \mu_T / \rho_T, \quad P_S = \mu_S / \rho_S, \quad (2.15)$$

to finally obtain:

$$I = \frac{2\pi e^2}{\hbar} V |M|^2 \rho_T \rho_S (1 + P_T P_S \cos \theta) \quad (2.16)$$

Thus, Equation 2.16 indicates the current consists of two elements, a spin-independent and a spin-dependent component. When either the tip or sample has no polarization (*i.e.*, $P_T = 0$ or $P_S = 0$), Equation 2.16 reduces to Equation 2.8. Also note that ρ_T and ρ_S reflect the density of states at the Fermi level E_F .

Evidently, the tunnel current is sensitive to the magnetic properties of the tip and sample. If at least one of the electrodes local spin-up density of states ρ_{\uparrow} is different from the local spin-down density of states ρ_{\downarrow} , an additional current, known as a spin-polarized or magnetoresistive current, is measured. This was first observed in tunnel junctions by Tedrow and Meservey in 1971 [78] and then by Jullière in 1975 [79]. In the following decades, this phenomenon was further developed, culminating in the discovery of nearly 100 % magnetoresistance by Fert and Grünberg in Fe-Cr thin films [80, 81], for which they were awarded a Nobel prize [82]. In STM, spin-polarized current was first observed in 1990 by Wiesendanger *et al.*

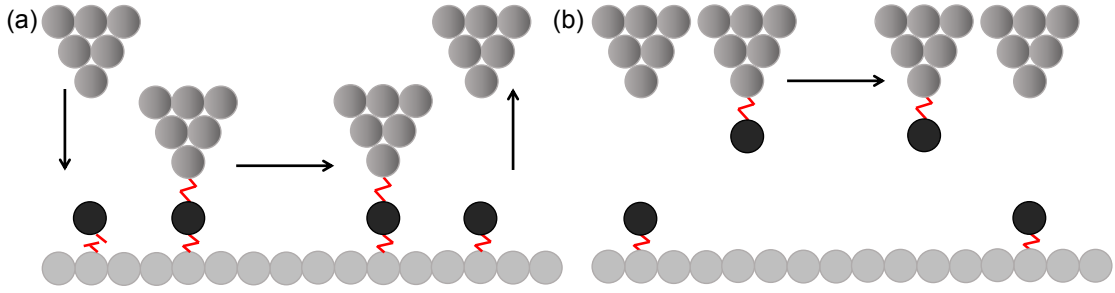


Figure 2.3: **Two families of atomic manipulation.** Schematic depicting the parallel (a) and perpendicular (b) atomic manipulation method. In (a), the STM tip approaches the adatom until a temporary adatom-tip bond is formed (red). The tip is then moved laterally across the surface, maintaining the tip-adatom and substrate-adatom bond throughout the motion. Once the desired location is reached, the tip is retracted. In (b), the adatom-substrate bond is broken as the atom is picked up by the tip. After the tip is moved to the desired location, the tip-adatom bond is broken and the adatom reforms its bond to the substrate.

[83] by using a ferromagnetic CrO_2 tip to measure the surface of single crystal $\text{Cr}(001)$. $\text{Cr}(001)$ exhibits topological antiferromagnetic ordering, such that terraces separated by atomic steps have alternating magnetization directions. This results in an increase in the measured current when the surface polarization P_S and the tip polarization P_T at the Fermi level E_F are aligned $I_{\uparrow\uparrow} = I_0(1 + P_T P_S)$ and a decrease in measured current when antialigned $I_{\uparrow\downarrow} = I_0(1 - P_T P_S)$. For constant-current images, terraces aligned with the tip appear at higher absolute z -values. As the current is kept constant, the conductance of the junction is higher and therefore the feedback maintains a higher distance for the same set-point current. On the other hand, for terraces anti-aligned with the tip, the conductance of the junction is lower and the feedback maintains a lower distance for the same set-point current. Thus, they appear at lower absolute z -values. The higher and lower z -values are taken with respect to measurements done with a non-magnetic tip that only measures I_0 . This is indeed what Wiesendanger *et al.* observed. Since then, SP-STM has been used to study the magnetic properties of nanoscale spin structures on surfaces [18–20, 23–25, 27], and eventually individual spins [38–41, 43–47]. For further information on SP-STM, see Refs. [21, 75, 84].

2.1.3 Atomic manipulation

Naturally, the accessibility to the atomic scale that STM provides at surfaces invites the question of how such a tool can be used to manipulate matter on the same scale. Following the invention of the STM, strategies to do so quickly materialized. Atomic manipulations can be categorized into two families, one consisting of atomic displacement processes parallel to the surface (Figure 2.3a) and the other of perpendicular atomic displacements (Figure 2.3b) [85, 86]. The former consists of approaching the target adatom until a temporary bond with the tip apex is formed. The tip is moved laterally along the surface, maintaining this bond until the desired location is reached and the tip is retracted, breaking this bond. In order for this manipulation to be successful, a stable equilibrium between the tip-adatom and substrate-adatom

bond must be achieved. This is done by tuning parameters such as tip-adatom distance, tunnel bias, and choice of tip or substrate material. The latter atomic manipulation method consists of using the tip to pick up the atom, therefore breaking the substrate-atom bond and retracting, then moving in the xy plane to drop of the atom in a new location, forming a new bond. In general, both processes are extremely sensitive to the tip configuration and composition at the apex, which can be difficult to ascertain. Despite this, consistent manipulation procedures for several tip-adatom-substrate systems has been demonstrated [32, 34, 39, 45, 46, 87–98].

2.1.4 Experimental apparatus

STM Chamber

All measurements are done with a home-built STM [99] operating at liquid He temperature. The exact temperature on the sample is measured with a Cernox sensor, placed on the STM head. The base pressure during measurements is below $p = 1 \times 10^{-10}$ mbar. The tip is at virtual ground and the tunnel voltage is applied to the sample. Thus, for negative bias voltages, electron tunneling occurs from sample to tip, and for positive bias voltages, from tip to sample. Unless stated otherwise, W tips are used and images are acquired in constant-current mode.

For SP-STM measurements, antiferromagnetic $\text{Mn}_{88}\text{Ni}_{12}$ tips are used. They are produced following Ref. [100], where commercially available 0.25 mm thick $\text{Mn}_{88}\text{Ni}_{12}$ foil is cut into rods, electrochemically etched, then sputtered with Ar^+ ions once in an UHV environment before being placed in the STM for use.

Sample Preparation Chamber

The STM chamber sits adjacent to a sample preparation chamber, connected by a sample and tip UHV transfer stage. Two monocrystalline metal substrates with electron and phonon decoupling layers are grown in this chamber, and used in this thesis: a single layer of graphene grown on Ir(111) and a MgO film 1-2 monolayers thick grown on Ag(100). Before the decoupling layer is grown, the substrates are cleaned by repeated Ar^+ sputtering ($T = 300$ K) and annealing ($T_{\text{Ag}} = 800$ K, $T_{\text{Ir}} = 1600$ K) cycles.

To grow the graphene on Ir(111), low-pressure chemical vapor deposition (CVD) is utilized by exposing the bare metal to 100 Langmuir of ethylene (C_2H_4) at 1350 K [48, 50, 101, 102]. The reaction is self-limiting, as it requires direct access to the bare substrate for the precursor to disassociate.

To grow the MgO film on Ag(100), the bare metal is exposed to an Mg flux from a Knudsen cell evaporator in an oxygen partial pressure of 1×10^{-6} mbar at 770 K [42, 49, 100, 103]. This corresponds to a growth rate of 0.1-0.2 monolayers (MLs) per minute. One monolayer (ML) of MgO is defined as one Mg atom per substrate Ag atom.

Following the growth of the decoupling layer, the sample is transferred from the preparation chamber into the STM chamber through a transfer stage, without breaking UHV. Once in the STM chamber, transition metal and lanthanide atoms are deposited. The STM offers a low temperature environment in which diffusion is inhibited. To ensure minimal contamination of the sample, these atoms are deposited from thoroughly degassed, high purity rods (99.9%) with an electron beam evaporator at a substrate temperature of roughly 10-12 K. The coverage of adatoms is given in monolayers (ML). For graphene, the coverage of $\Theta = 1$ ML corresponds to one adsorbate atom per unit cell, while for MgO, it corresponds to one adsorbate atom per oxygen atom.

2.2 Modeling spin systems

Before the formulation of quantum theory, classical models of magnetism attempted to explain the spontaneous magnetization of ferromagnetic materials through the introduction of the Weiss molecular field [6]. The field coupled the individual magnetic moments, inducing preferential alignments below some temperature threshold. While successful in predicting the characteristics of bulk ferromagnets at high temperatures and applied magnetic fields, there was little justification for introducing such a field. About a decade and a half later, the Stern-Gerlach experiment demonstrated for the first time that electrons had non-zero, quantized magnetic moments [10]. Although this was a significant step towards the confirmation of the Bohr-Sommerfeld hypothesis of discrete orbitals and energy levels within the atom, the result was inconsistent with the prediction of the non-relativistic Schrödinger equation: that a single s electron has a magnetic moment of zero [104]. The discrepancies between theory and experiment were quickly resolved with further developments in relativistic quantum theory [14, 105, 106], resulting in the introduction of concepts such as electron spin, exchange and spin-orbit coupling. Most notably, Dirac's relativistic correction of Schrödinger's equation necessitated two component wavefunctions, justifying the existence of electron spin. In addition, the relativistic expansion terms of the electron energy clearly describe Zeeman and spin-orbit interactions. These interactions are fundamental to the modern theory of magnetism, and are therefore integral to any modeling of spin systems.

The spin Hamiltonian offers a powerful tool for experimentalists to model spin systems. Pryce first introduced this approach to investigate the effect of the Zeeman and spin-orbit perturbation terms on the magnetic properties of $3d$ paramagnetic ions [107], successfully reproducing experimental observations. In this section, the interactions relevant to the systems studied within this thesis are introduced. The exchange interaction, spin-orbit coupling, and the Zeeman effect, the influence of a crystal field and the nuclear magnetic moment are discussed. In the context of this thesis, these terms form the unperturbed Hamiltonian, unless otherwise stated, and determine the magnetic states of the system. When modeling the dynamics of spin systems, additional perturbation terms are needed, mainly spin-phonon coupling and Kondo-like spin tunneling. Rates for these terms are described, and the concept of quantum tunneling of magnetization is introduced.

2.2.1 Exchange interaction

In pursuit of a quantum mechanical formulation of a spin-spin interaction that could explain the observed spontaneous magnetization of ferromagnets, and therefore justify the existence of Weiss' molecular field, both Dirac and Heisenberg independently considered the effect of the Coulomb interaction energy $\hat{\mathcal{H}}$ between two 1/2-spin electrons near each other (e.g., two orbitals on the same atom, or on adjacent atoms) [105, 106]. The overall wavefunction for this two-electron system with total spin S_{tot} can be composed of the product of the single electron wavefunctions of the form $\psi\chi$, where ψ and χ are the spatial and spin components, respectively. If we ascribe $\psi_a(r_1)$ to the first electron, and $\psi_b(r_2)$ to the second, where r_1 and r_2 are spatial coordinates, the joint wave functions that satisfy exchange symmetry are [108]:

$$\begin{aligned}\Psi_S &= \frac{1}{\sqrt{2}} [\psi_a(r_1)\psi_b(r_2) - \psi_a(r_2)\psi_b(r_1)] \chi_S \\ \Psi_T &= \frac{1}{\sqrt{2}} [\psi_a(r_1)\psi_b(r_2) + \psi_a(r_2)\psi_b(r_1)] \chi_T\end{aligned}\tag{2.17}$$

where Ψ_S is the singlet state corresponding to total spin $S = 0$ and Ψ_T is the triplet state corresponding to total spin $S = 1$. The overall wave function must be antisymmetric for fermions, thus the spin part of the wavefunction χ must be antisymmetric for the singlet state and symmetric for the triplet state. Assuming the spin part is normalized, the corresponding energy of each state is given by:

$$\begin{aligned}E_S &= \int \Psi_S^* \hat{\mathcal{H}} \Psi_S dr_1 dr_2 \\ E_T &= \int \Psi_T^* \hat{\mathcal{H}} \Psi_T dr_1 dr_2\end{aligned}\tag{2.18}$$

Most relevant is the *difference* in energy between these two states:

$$E_S - E_T = 2 \int \psi_a^*(r_1) \psi_b^*(r_2) \hat{\mathcal{H}} \psi_a(r_2) \psi_b(r_1) dr_1 dr_2\tag{2.19}$$

Solely due to a Coulomb interaction and obeying exchange symmetries, non-degenerate states are obtained. The Hamiltonian can be parameterized by noting the relationship $\hat{S}_{tot}^2 = \hat{S}_1^2 + \hat{S}_2^2 + 2\hat{S}_1 \cdot \hat{S}_2$. Thus, for the singlet state $S = 0$, $\hat{S}_{tot}^2 = S(S+1) = 0$, and $\hat{S}_1 \cdot \hat{S}_2 = -1/4$ and for the triplet state $S = 1$, $\hat{S}_{tot}^2 = 2$, and $\hat{S}_1 \cdot \hat{S}_2 = 1/4$. An effective Hamiltonian describing the system is given by:

$$\mathcal{H} = \frac{1}{4} (E_S + 3E_T) - (E_S - E_T) \hat{S}_1 \cdot \hat{S}_2\tag{2.20}$$

such that the energy of each state E_S and E_T is recovered in the case of the singlet or triplet state. The first term is constant in energy and spin-independent, while the second directly

describes the spin-spin interaction. Defining the exchange integral as:

$$J = \frac{E_S - E_T}{2} = \int \psi_a^*(r_1) \psi_b^*(r_2) \hat{\mathcal{H}} \psi_a(r_2) \psi_b(r_1) dr_1 dr_2 \quad (2.21)$$

the spin-dependent term in the effective Hamiltonian can be expressed as:

$$\mathcal{H}_{spin} = -2J \hat{S}_1 \cdot \hat{S}_2 \quad (2.22)$$

So, the spin-spin interaction between two electrons is characterised by the sign and magnitude of the exchange integral. Calculating this is typically not trivial, and dependent on the physical situation being considered. However, Equation 2.22 indicates that when $J > 0$, E_S is greater than E_T and the triplet state $S = 1$ is favoured. This corresponds to a parallel alignment of the electron spins. When $J < 0$, E_S is less than E_T and the singlet state $S = 0$ is favoured, corresponding to an antiparallel alignment of electron spins. Due to the conditions of exchange symmetries for fermions, electrons of the same spin cannot be in the same spatial position and prefer to avoid each other to minimize their Coulomb repulsion energy. Thus, when considering electrons on the same atom, their preference is to have greater spatial separation and parallel alignment of their spin. This is known as Coulomb exchange. When considering multiple adjacent atoms where electrons can hop between them, the situation is slightly more complicated. The degree of orbital overlap and filling determines whether parallel or antiparallel alignment is preferred. An electron is allowed to hop between atomic sites only if a spin state is available to do so. This idea, known as kinetic exchange, competes with the single-site Coulomb exchange to determine how neighboring spins couple to each other in a crystal lattice. In this situation Equation 2.22 can be generalized to capture the interaction between all spins in a given lattice:

$$\mathcal{H} = -2 \sum_{i>j} J_{ij} \hat{S}_i \cdot \hat{S}_j \quad (2.23)$$

where i and j collectively define the spin sites. In this picture, the Weiss molecular field can be interpreted as the spatial average of the exchange coupling J across the entire lattice. Equation 2.23 can manifest differently for different elements and crystal structures, producing a range of exchange-mediated magnetic orders. These mechanisms can be categorized into two broad families: direct exchange between spins and indirect exchange between spins mediated by some intermediary. Further descriptions of all the different manifestations of exchange interactions can be found in Refs. [108–110].

For the systems studied within this thesis, the ferromagnetic intra-atomic exchange between shells on a single atom is most relevant. This interaction is generalized as [37]:

$$\mathcal{H}_{intra} = - \sum_{i \neq j} A_{ij}^{ex} \hat{S}_i \cdot \hat{S}_j \quad (2.24)$$

\hat{S}_i are the spin operators and A_{ij}^{ex} is the exchange coupling between shells i and j .

2.2.2 Spin-orbit coupling and the Zeeman effect

In a classical picture, the electromagnetic interaction between the electron's spin and its orbital motion about the positively charged nucleus couples the spin s and orbital ℓ moments. In other words, the motion of a charged particle in an electric field creates an apparent magnetic field seen from the electrons perspective. The interplay of the electron spin with this field is effectively a Zeeman interaction. This effect is purely relativistic, typified by Dirac's correction to the relativistic Hamiltonian of an electron of mass m_e and charge e in a hydrogenic atom [110]:

$$\mathcal{H} = \left[\frac{\hbar^2}{2m_e} (\hat{p} + eA)^2 + V(r) \right] - \frac{|p|^4}{8m_e^3 c^2} + \frac{e}{m_e} (\nabla \times A) \cdot \hat{s} + \frac{1}{2m_e^2 c^2 r} \frac{dV}{dr} \hat{\ell} \cdot \hat{s} - \frac{1}{4m_e^2 c^2} \frac{dV}{dr} \quad (2.25)$$

where $V(r)$ is the spherical Coulomb potential of the nucleus, A is the vector potential of the effective magnetic field, c is the speed of light, \hat{s} are the Pauli spin operators, and $\hat{\ell}$ is the orbital moment operator. The first term is the non-relativistic Hamiltonian containing both a kinetic term and potential term. Of key interest here are the third and fourth terms, that describe Zeeman and spin-orbit interactions of the electron, respectively. The complete¹ Zeeman interaction is given by:

$$\mathcal{H}_Z = \frac{e}{2m_e} (\hat{\ell} + 2\hat{s}) \cdot B_{int} \quad (2.26)$$

where B_{int} is the apparent magnetic field seen from the electrons perspective. This can be generalized to a multi-electron atom experiencing the effect of any applied field B :

$$\mathcal{H}_Z = \frac{e}{2m_e} (\hat{L} + 2\hat{S}) \cdot B \quad (2.27)$$

In the presence of large spin-orbit coupling, \hat{L} and \hat{S} are not good quantum numbers. Thus, we can re-express Equation 2.27 as a function of the total angular momentum operator \hat{J} . This can be done by recognizing $\hat{L} + 2\hat{S} = \hat{J} + \hat{S}$. \hat{S} can be expressed as the time-averaged value projected onto \hat{J} :

$$\hat{S}_{avg} = \frac{(\hat{S} \cdot \hat{J})}{J^2} \hat{J} \quad (2.28)$$

and

$$\hat{S} \cdot \hat{J} = \frac{1}{2} (J^2 + S^2 - L^2) = \frac{\hbar^2}{2} [j(j+1) + s(s+1) - l(l+1)] \quad (2.29)$$

The Zeeman term can then be expressed as:

$$\mathcal{H}_Z = \frac{e}{2m_e} (\hat{J} + \hat{S}_{avg}) \cdot B = \frac{e\hbar^2}{2m_e} \left[1 + \frac{j(j+1) - l(l+1) + 3/4}{2j(j+1)} \right] \hat{J} \cdot B \quad (2.30)$$

¹This is done by combining the third term with paramagnetic and diamagnetic terms that arise from the expansion of the first term. See for example Ref. [110] pg. 88-89 or Ref. [108] pg. 18-19.

The quantity in the square brackets is known as the Landé g -factor and relates the orbital and spin moment to the magnetic moment. $s(s+1)$ is replaced with $3/4$ for spin-1/2 electrons. Using the definition of Bohr magneton $\mu_B = e\hbar/2m_e$ and choosing z -axis to lie along the field:

$$\mathcal{H}_Z = \mu_B g B \hat{J}_z \quad (2.31)$$

SP-STM tips are known to produce non-negligible dipolar and exchange fields [100, 103, 111]. The stray magnetic fields originating from the SP-STM tip are modeled as a Zeeman interaction of this form. Now considering the fourth term of Equation 2.25, the spin-orbit interaction for a single electron is parameterized by the coupling strength λ :

$$\mathcal{H}_{so} = \frac{1}{2m_e^2 c^2 r} \frac{dV}{dr} \hat{\ell} \cdot \hat{s} = \lambda \hat{\ell} \cdot \hat{s} \quad (2.32)$$

For hydrogenic orbitals, this coupling strength is:

$$\lambda = \frac{m_e}{2} Z^4 \alpha^4 c^2 \frac{1}{n^3 l(l + \frac{1}{2})(l + 1)} \quad (2.33)$$

where $\alpha = e^2/4\pi\epsilon_0\hbar c$. Equation 2.33 clearly demonstrates the strong dependence of the coupling strength on the effective charge of the nucleus Z . Thus, heavier elements and shells closer to the nucleus have much higher values of λ . $3d$ electrons typically have values of several tens of meV while $4f$ electrons can be several hundreds of meV. To extend to a multi-electron atom, the LS-coupling scheme (where the total angular moment $L = \sum l$ couples to the total spin moment $S = \sum s$) can be used for both $3d$ and $4f$ electrons. For heavier atoms where the spin-orbit coupling dominates, the jj-coupling scheme (where l and s for each electron couples together) provides better agreement with experimental observations of the fine structure [108]. As we shall see, the interplay between spin-orbit coupling and the crystal field environment is instrumental in determining magnetic properties of spin systems at all scales.

2.2.3 Crystal field interaction

The energy associated with a moments preferred direction of magnetization, relative to energetically unfavorable orientations, is known as magnetic anisotropy. Anisotropy has several geometric origins, but the single-ion anisotropy most relevant to adatoms and dimers on surfaces is magnetocrystalline anisotropy (MCA). Placing an atom within a crystal lattice subjects the orbitals to a Coulomb interaction with the surrounding atoms. This has the effect of stabilizing certain orbitals, and destabilizing others. The spatial dependence of the orbital moment couples the total magnetic moment to the geometry of the crystal via the spin-orbit interaction. The strength of the crystal field interaction relative to the spin-orbit coupling determines the magnitude of the anisotropy. The electric potential $\phi_{CF}(r)$ created by the

surrounding charge distribution $\rho(r)$ can be expressed as [110]:

$$\phi_{CF}(r) = \int \frac{\rho(r')}{4\pi\epsilon_0 |r - r'|} d^3 r' \quad (2.34)$$

It is convenient to re-express this as a function of spherical harmonics. This can be done with:

$$\frac{1}{|r - r'|} = \frac{1}{r'} \sum_{n=0}^{\infty} \frac{4\pi}{(2n+1)} \left(\frac{r}{r'}\right)^n \sum_{m=-n}^n (-1)^m Y_n^{-m}(\theta', \phi') Y_n^m(\theta, \phi) \quad (2.35)$$

and by defining:

$$\gamma_{nm} = \frac{4\pi}{(2n+1)} \int \frac{\rho(r') (-1)^m Y_n^{-m}(\theta', \phi')}{r'^{n+1}} d^3 r' \quad (2.36)$$

Equation 2.34 becomes:

$$\phi_{CF}(r, \theta, \phi) = \sum_{n=0}^{\infty} \sum_{m=-n}^n r^n \gamma_{nm} Y_n^m(\theta, \phi) \quad (2.37)$$

The crystal field Hamiltonian is then defined:

$$\mathcal{H}_{CF} = \int \rho_0(r) \phi_{CF}(r) d^3 r \quad (2.38)$$

where $\rho_0(r)$ is the charge distribution of the atom within the crystal field. For the spatially extended $3d$ orbitals, \mathcal{H}_{CF} is typically much stronger than \mathcal{H}_{so} . This heavily mixes the orbital moment states $|L, L_z\rangle$ and results in a low or zero orbital moment. This is known as quenching. $|L, L_z\rangle$ are no longer good quantum numbers and thus, the magnetic states are better represented by states $|S, S_z\rangle$, as S is still a good quantum number. Additionally, the $3d$ orbitals tend to overlap with the orbitals of the surrounding lattice, making it difficult to distinguish between $\rho_0(r)$ and $\rho(r)$. In this case, \mathcal{H}_{CF} can instead be expressed as a sum of \hat{S}_x , \hat{S}_y , and \hat{S}_z operators, whose order reflects the symmetry of the surrounding lattice. For example, a site with uniaxial symmetry gives a term of the form $D\hat{S}_z^2$, while cubic symmetry gives a term of the form $D_c(\hat{S}_x^4 + \hat{S}_y^4 + \hat{S}_z^4)$, where the strength is parameterized by D and D_c .

For the $4f$ orbitals that sit much closer to the nucleus, \mathcal{H}_{so} is typically much stronger than \mathcal{H}_{CF} . The orbital moments are not quenched and $|J, J_z\rangle$ is a good basis. In this case, it is customary to express Equation 2.38 as the sum of Stevens operators \hat{O}_n^m [112, 113]

$$\mathcal{H}_{CF} = \sum_{nm} B_n^m \hat{O}_n^m \quad (2.39)$$

where \hat{O}_n^m are reformulations of the spherical harmonics $Y_n^m(\theta, \phi)$ written as a function of \hat{J} . In principle, the crystal field parameters B_n^m can be calculated if the charge distribution is known. This can be estimated by density function theory (DFT) or point-charge models, although these may be too rudimentary to accurately reflect any charge redistribution or shielding effects. The Stevens operators are determined by the symmetry of the crystal. For an atom with total

angular momentum J in a site with k -fold symmetry, m takes on even values from 2 to $2J$ and $n = qk$ where $q = 0, 1, \dots, m - 1$ [114]. The interaction between rare-earth adatoms and their surrounding crystal field are modeled with Equation 2.39.

2.2.4 Hyperfine interaction

Up till now, the nuclear magnetic moment has not been considered. Of course, analogous to the spin-orbit interaction, there is an interaction that occurs between the atomic and nuclear moment I . Assuming J is a good quantum number, this takes the form [115]:

$$\mathcal{H}_{hf} = A_{hf} \hat{I} \cdot \hat{J} \quad (2.40)$$

where A_{hf} is the hyperfine coupling constant and typically on the order of a few μeV . Equation 2.40 contains only the dominant term, reflecting dipolar coupling between the two moments, sufficient for the modeling of the systems presented in this thesis. There are, however, additional weaker terms to account for auxiliary interactions (*e.g.* the Zeeman interaction with I). As we shall see, the hyperfine interaction plays a critical role in determining the allowed transitions, and therefore the stability of SAMs, when any two magnetic quantum states are energetically in close proximity.

2.2.5 Spin-phonon coupling

In the systems studied within this thesis, the aforementioned interactions serve as the unperturbed Hamiltonian, from which the magnetic states are determined. Spin systems interact with their surrounding environment, and transitions between these magnetic states can readily occur. One mechanism by which this can happen is through spin-phonon coupling, where lattice vibrations (*i.e.* phonons) oscillate the local charge distribution and induce electromagnetic fields that couple to the spin. This can be treated as a perturbation of the crystal field potential, where phonons create local strain ϵ at the spin site. Orbach was the first to utilize this approach [116]:

$$\phi_{CF} = \phi_{CF}^{(0)} + \epsilon \phi_{CF}^{(1)} + \epsilon^2 \phi_{CF}^{(2)} + \dots \quad (2.41)$$

where the first term is the static crystal field potential, and the second and third terms represent first and second order strain, where $\phi_{CF}^{(1)}$ and $\phi_{CF}^{(2)}$ indicate the first and second derivatives of $\phi_{CF}^{(0)}$ with respect to the displacement of neighboring atoms. There are three relevant processes that result from these terms. Historically, they are known as the direct processes, two-phonon Orbach processes, and the Raman processes (pictured in Figure 2.4) [116–118]. Terms that are higher order in strain are typically not considered. The direct process describes transitions between states $|a\rangle$ and $|b\rangle$ that occur through the absorption or emission of a single phonon of energy $\hbar\omega_a$. To satisfy conservation of energy, the energy of the phonon must be equal to the energy difference between the states $\hbar\omega_{ba} = E_b - E_a$. The rate for this single phonon process

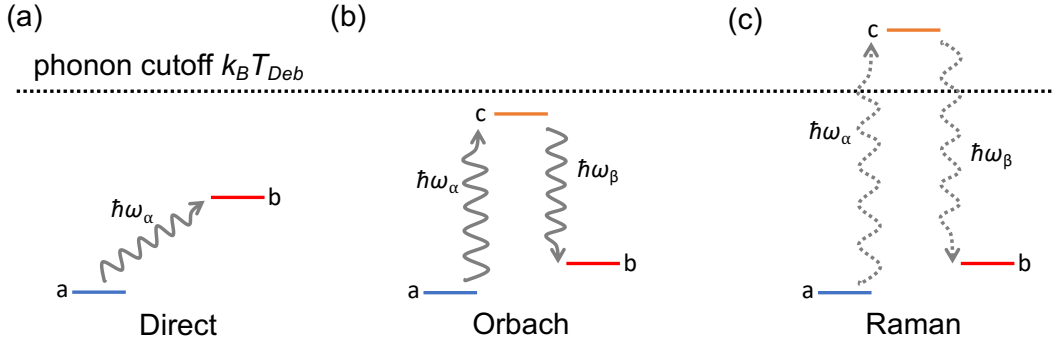


Figure 2.4: Direct, Orbach, and Raman phonon processes. Schematic depicting the direct (a), Orbach (b), and second-order Raman (c) process of phonon scattering. In (a), a single phonon of energy $\hbar\omega_\alpha = E_b - E_a$ is absorbed, exciting the system from state $|a\rangle$ to state $|b\rangle$. In (b), an initial phonon of energy $\hbar\omega_\alpha = E_c - E_a$ is absorbed, exciting the system to state $|c\rangle$, then a second phonon of energy $\hbar\omega_\beta = E_b - E_c$ is emitted, relaxing the system to state $|b\rangle$. Both phonons have energy below the phonon cutoff $\hbar\omega_\alpha, \hbar\omega_\beta < k_B T_{Deb}$. (c) is identical to (b), except the phonons have energy above the allowed frequency $\hbar\omega_\alpha, \hbar\omega_\beta > k_B T_{Deb}$. Note that the first-order Raman process, where $E_a > E_b > E_c$ or $E_a < E_b < E_c$ and both phonons are still above the phonon cutoff energy, is not pictured.

is given by:

$$W_{ba}^{1-ph} = \frac{2\pi}{\hbar^2} \epsilon^2 \left| \langle b | \phi_{CF}^{(1)} | a \rangle \right|^2 G^{1-ph}(\omega_{ba}, \omega_\alpha) \quad (2.42)$$

where conservation of energy, absorption, and emission are described by $G^{1-ph} = \delta(\omega - \omega_\alpha) \bar{n}_\alpha + \delta(\omega + \omega_\alpha) (\bar{n}_\alpha + 1)$ and $\bar{n}_\alpha = [\exp(\hbar\omega_\alpha / k_B T) - 1]^{-1}$ is the Bose-Einstein distribution. The 2-phonon Orbach process involves transitions between states $|a\rangle$ and $|b\rangle$ through some intermediate state $|c\rangle$ that lies below the Debye energy $k_B T_{Deb}$. As pictured in Figure 2.4, a phonon of energy $\hbar\omega_\alpha$ equal to the energy difference between the states $\hbar\omega_{ca} = E_c - E_a$ is absorbed, followed by a subsequent emission of a phonon of energy $\hbar\omega_\beta$ equal to the energy difference between the states $\hbar\omega_{bc} = E_b - E_c$. This rate, first shown by Orbach, is given by [116]:

$$W_{ba}^{2-ph, Orb} = \frac{2\pi}{\hbar^2} \epsilon^2 \frac{\left| \langle b | \phi_{CF}^{(1)} | c \rangle \langle c | \phi_{CF}^{(1)} | a \rangle \right|^2}{\left| \langle b | \phi_{CF}^{(1)} | c \rangle \right|^2 + \left| \langle c | \phi_{CF}^{(1)} | a \rangle \right|^2} G^{2-ph}(\omega_{ba}, \omega_\alpha, \omega_\beta) \quad (2.43)$$

Note that emission, followed by absorption, can occur if $E_a, E_b > E_c$. Of course, the reverse situations are also possible, where the initial and final states are simply reversed. These are included through G^{2-ph} , which is defined here as:

$$G^{2-ph} = \delta(\omega_{ba} - \omega_\alpha + \omega_\beta) \bar{n}_\alpha (\bar{n}_\beta + 1) + \delta(\omega_{ba} + \omega_\alpha - \omega_\beta) (\bar{n}_\alpha + 1) \bar{n}_\beta \quad (2.44)$$

where the first term describes the initial absorption of a phonon of energy $\hbar\omega_\alpha$ followed by the emission of a phonon of energy $\hbar\omega_\beta$ while the second term describes the reverse process

of emission followed by absorption. Note that energy conservation is always guaranteed by the Dirac-delta function δ , such that the difference in phonon energies is always equal to the energy difference of the initial and final states $\hbar\omega_{ba}$. This 2-phonon Orbach process can be interpreted as a higher-order direct process [119]. Indeed, the result is identical to two consecutive direct processes except for the scaling that occurs as a result of the denominator of Equation 2.43. In the case where $\hbar\omega_\alpha$ and $\hbar\omega_\beta$ are greater than the Debye energy $k_B T_{Deb}$, this is known as a Raman process, where the intermediate state $|c\rangle$ is considered to be a *virtual, non-stationary* state. In this case, Orbach showed that the rate is given by [116]:

$$W_{ba}^{2-ph,Ram} = \frac{2\pi}{\hbar^2} \epsilon^2 \left(\frac{\langle b | \phi_{CF}^{(1)} | c \rangle \langle c | \phi_{CF}^{(1)} | a \rangle}{|\hbar\omega_\beta| + |\hbar\omega_\alpha|} \right)^2 G^{2-ph}(\omega_{ba}, \omega_\alpha, \omega_\beta) \quad (2.45)$$

where G^{2-ph} is the same as above, and ensures that the total energy of the phonons is identical to the difference in energy between initial and final states $|a\rangle$ and $|b\rangle$. The different situations of emission-absorption and absorption-emission described for the Orbach process apply again here. Defining G^{2-ph} as such restricts Equation 2.45 to second-order processes. To include first order Raman processes (describing two consecutive emissions or two consecutive absorptions, if state $|c\rangle$ lies between states $|a\rangle$ and $|b\rangle$), two terms need to be added:

$$G^{2-ph} += \delta(\omega_{ba} + \omega_\alpha + \omega_\beta) (\bar{n}_\alpha + 1) (\bar{n}_\beta + 1) + \delta(\omega_{ba} - \omega_\alpha - \omega_\beta) \bar{n}_\alpha \bar{n}_\beta \quad (2.46)$$

where the first term describes two emissions and the second two absorptions. Note that $+=$ indicates that the two terms are added to Equation 2.44. Thus far, Equations 2.43 and 2.45 have assumed a single intermediate state $|c\rangle$. To generalize Equations 2.43 and 2.45 to systems containing a multitude of magnetic states, a sum over all possible intermediate states must be made. The primary difference between the 2-phonon Orbach and Raman processes is in the interpretation of the intermediate state. For Orbach processes, this state is obviously real and is accessible within the crystal. For the Raman processes, the existence of a virtual state $|c\rangle$ is understood to be an admixture of all the magnetic states of the system, resulting from the phonon perturbation [120]. Depending on the symmetry of the spin site and the phonon modes being considered, $\phi_{CF}^{(1)}$ may contain multiple terms that need to be summed over as well, each with its own magnetoelastic coupling constant. As noted in Ref. [119], terms first order in strain in a 3 dimensional crystal can have a maximum of 81 unique coupling constants. Work has been done to significantly reduce this number using symmetry conditions [121, 122], but the difficulty in estimating their value, experimentally or theoretically, remains. Many studies have taken the same approach as Abragam and Bleaney [117], where the exact form of $\phi_{CF}^{(1)}$ is not as important as the type of transitions (*i.e.*, $\Delta m = 0, \pm 1, \pm 2, \dots$) they produce [123–128]. The magnetoelastic coupling constants are then either left as free parameters, or approximated based on experimental data and assumptions of isotropy. In more recent studies, attempts to calculate the coupling constants based on electrostatic modeling have been made [120, 129].

All forms of phonon scattering are considered in the study of SAMs within this thesis, although they are not always found to be relevant to the dynamics. Direct and Orbach processes tend to dominate at temperatures below 10 K, while Raman processes become more active above this temperature [117, 120, 129]. Regardless, a more comprehensive model is no doubt useful. In implementing the rates of Equations 2.42, 2.43 and 2.45, we follow the same procedure as our predecessors and use a form of $\phi_{CF}^{(1)}$ that results in $\Delta m = \pm 1, \pm 2$ transitions, with a single isotropic magnetoelastic coupling constant as a free parameter. In addition, we assume a 2D Debye model to relate the strain ϵ to the phonon density of states ρ_{ph} through [117]:

$$\epsilon^2 = \frac{\rho_{ph} d\omega}{2\rho c^2} \quad (2.47)$$

where ρ is the crystal mass density and c is the speed of sound in the crystal. As an example, and following the formalism used in [119] (see Equations 5.39 and 5.41), the direct absorption and emission rates for Dy adatoms on graphene are given by:²

$$W_{MM'}^{1-ph} = \begin{cases} \frac{\nu_{ph}}{\rho_{gr} c^4 \hbar^3} \frac{E_{MM'}^2}{\exp(\beta E_{MM'}) - 1} w_{4f,MM'} \\ \frac{\nu_{ph}}{\rho_{gr} c^4 \hbar^3} E_{MM'}^2 \left(1 + \frac{1}{\exp(\beta E_{MM'}) - 1} \right) w_{4f,MM'} \end{cases} \quad (2.48)$$

where ρ_{gr} is the 2D mass density of graphene and c is the speed of sound in graphene. For these quantities, we use $\rho_{gr} = 7.7 \times 10^{-7} \text{ kg/m}^2$ and $c = 2.1 \times 10^4 \text{ m/s}$ [130]. $w_{4f,MM'}$ are the phonon matrix elements squared (acting only on the 4f shell) and $\beta = 1/k_B T$. We also include a coefficient ν_{ph} to account for the magnetoelastic coupling between graphene and the Dy adatom and for any other proportionality factors not explicitly mentioned in Equation 2.48 (see Refs. [119, 128]). Note that in theory ν_{ph} can be different for transitions with $\Delta m = \pm 1$ and $\Delta m = \pm 2$, but for simplicity, we use the same value for all transitions and all tunneling conditions.

2.2.6 Kondo-like spin tunneling

STM and SP-STM require electron tunneling to function. When investigating the magnetic properties of single adatoms and dimers, the effect of this tunneling current must be considered. Fortunately, the situation of a magnetic moment in the tunnel junction of an STM is very similar to a magnetic impurity sitting within a nonmagnetic metal. The conduction electrons of the nonmagnetic metal interact with the localized moment of the impurity, modeled by

²The 2D rate expression in the Supplementary Information of Ref. [128] is valid only for phonon absorption. To obtain an expression for emission in 2D, one must recompute the integral in Equation 5.41 of Ref. [119] in 2D rather than 3D.

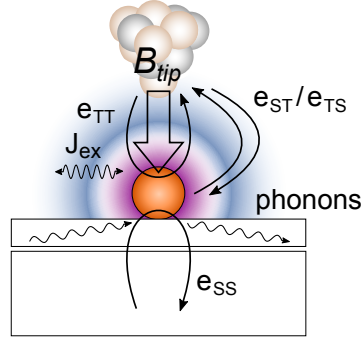


Figure 2.5: **Simplified sketch of the scattering processes.** The relevant processes that influence the spin lifetimes and occupancy in tunneling conditions are the scattering with phonons and with substrate and tip electrons, J_{ex} represents the intra-atomic exchange interaction, and B_{tip} the magnetic field produced by the tip.

an s - d exchange interaction. This situation was first explored by Anderson in 1961 [16] and by Kondo in 1964 [131] to explain low temperature behavior of conduction electrons in metals. Their formulations were shown to be identical under a transformation by Schrieffer and Wolff [132], and later extended by Appelbaum to explain anomalous zero-bias conductance measurements in tunnel junctions [133]. As STM and SP-STM opened the door to directly study individual spins on surfaces, this model was adopted to describe the scattering of tip and substrate tunneling electrons with localized spins [40, 134–138]. We utilize this model in the study of the spin dynamics of Dy adatoms on graphene/Ir(111), where tunneling electrons can scatter with the $4f$ or $5d6s$ shells. This Kondo-type Hamiltonian has the form [136]:

$$\mathcal{H}_{te} = \sum_{\alpha, \lambda, \lambda', \sigma, \sigma'} T_{\alpha, \lambda, \lambda'} \frac{\tau_{\sigma\sigma'}^{(\alpha)}}{2} \hat{S}_{\alpha} c_{\lambda\sigma}^{\dagger} c_{\lambda'\sigma'} \quad (2.49)$$

where α can take on the values x, y, z , and 0 . $\lambda = (k, \eta)$ defines the single particle state k in the electrode η together with the spin σ of the tunnel electrons. We consider the electrodes $\eta, \eta' \in \{S = \text{surface}, T = \text{tip}\}$, where prime indicates the final electrode while unprimed indicates the initial electrode. $\tau^{(\alpha)}$ and \hat{S}_{α} correspond to the Pauli matrices and spin operators, respectively. The spin operators correspond to the shell of the Dy adatom in which tunneling occurs. For $\alpha = 0$, $\tau^{(0)}$ is defined as the identity matrix, and T_0 is the Coulomb potential scattering interaction parameter. For $\alpha = x, y$, and z , T_{α} corresponds to the exchange-tunneling interaction parameter for each direction. The exchange-tunneling interaction is spin-rotational invariant, thus, $T_x = T_y = T_z \equiv T_k$.

\mathcal{H}_{te} describes four types of electronic interactions (pictured in Figure 2.5): substrate-substrate scattering (e_{SS}), tip-tip scattering (e_{TT}), and tip-substrate/substrate-tip scattering (e_{TS}/e_{ST}). In the case of e_{SS} and e_{TT} scattering, the creation or annihilation of an electron hole pair in the electrodes may scatter with the adatom, but do not contribute to the tunneling current like e_{TS} and e_{ST} . To derive the scattering rates that result from Equation 2.49, we follow the

formalism presented by Delgado *et al.* [136]. The electron-induced transition rates from an initial state M in electrode η to final state M' in electrode η' can be compactly written as:

$$W_{MM'}^{\eta\eta'} = \sum_{\alpha=+, -, z} |\langle M' | \hat{S}_\alpha | M \rangle|^2 R_{\alpha,\eta\eta'} \quad (2.50)$$

Spin operators that allow $\Delta m = 0, \pm 1$ transitions are allowed. $R_{\alpha,\eta\eta'}$ has four components that correspond to the processes described above:

$$\begin{aligned} R_{\alpha,ST} &= \frac{2\pi}{\hbar} \zeta^2 \zeta_S \zeta_T Q_{\alpha,ST} F_{ST}(E_{MM'}, \pm eV_b) \\ R_{\alpha,SS} &= \frac{2\pi}{\hbar} \zeta^2 \zeta_S^2 Q_{\alpha,SS} F_{SS}(E_{MM'}, eV_b = 0) \\ R_{\alpha,TS} &= \frac{2\pi}{\hbar} \zeta^2 \zeta_T \zeta_S Q_{\alpha,TS} F_{TS}(E_{MM'}, \pm eV_b) \\ R_{\alpha,TT} &= \frac{2\pi}{\hbar} \zeta^2 \zeta_T^2 Q_{\alpha,TT} F_{TT}(E_{MM'}, eV_b = 0) \end{aligned} \quad (2.51)$$

in which $\zeta = T_k/T_o$ is the ratio between inelastic and elastic tunneling strengths, V_b is the tunnel bias, tip-adatom and substrate-adatom transmissions are parameterized by the coefficients ζ_T and ζ_S , and $F_{\eta\eta'}$ is:

$$F_{\eta\eta'}(E_{MM'}, \pm eV_b) = \frac{E_{MM'} \pm eV_b}{\exp[(E_{MM'} \pm eV_b)\beta] - 1} \quad (2.52)$$

and $Q_{\alpha,\eta\eta'}$ accounts for the polarization of the electrodes:

$$Q_{+, \eta\eta'} = \rho_{\downarrow}^{\eta} \rho_{\uparrow}^{\eta'} \quad Q_{-, \eta\eta'} = \rho_{\uparrow}^{\eta} \rho_{\downarrow}^{\eta'} \quad Q_{z, \eta\eta'} = \rho_{\uparrow}^{\eta} \rho_{\uparrow}^{\eta'} + \rho_{\downarrow}^{\eta} \rho_{\downarrow}^{\eta'} \quad (2.53)$$

$E_{MM'}$ is the energy difference between the state M and M' . The sign in $E_{MM'} \pm eV_b$ in Equation 2.52 is positive for surface to tip tunneling (e_{ST}) and negative for tip to surface tunneling (e_{TS}). Some of the parameters within Equation 2.51, such as $E_{MM'}$, can easily be determined from the Hamiltonian. For others, such as ζ and the polarizations ρ of Equations 2.53, reasonable estimates can be made. Regardless, all are system dependent and will be discussed in further detail in later Chapters.

2.2.7 Quantum tunneling of magnetization

In the classical picture, a magnetic moment with uniaxial anisotropy has two stable orientations, embodied by the well-known double well potential. Starting from one well, the moment can be rotated continuously, climbing the anisotropy barrier until the top is reached, and the moment relaxes into the opposite well, corresponding to the opposite orientation. An energy equal to the height of the barrier must be expended to reverse the moment. In the quantum regime, the continuity is superseded by discrete levels characterized by the spin states $|S, S_z\rangle$ or $|J, J_z\rangle$, depending on the choice of basis. Quantum mechanics also tells us that coherent

tunneling between states through the barrier is possible for certain double well shapes (*i.e.*, when states on either side of the barrier are close in energy). The shape of the double well, and whether tunneling occurs between two states, is determined by the spin Hamiltonian, specifically the crystal and magnetic field terms. Restricting the discussion to the cases when J is a good quantum number, the terms that do not commute with J_z , typically crystal field terms that dependent on J_x or J_y or a magnetic field B_x or B_y , induce state mixing. For example, consider the two state system, $|J_z\rangle$ and $|-J_z\rangle$, that intersect at a given energy and magnetic field. Figure 2.6 illustrates two level crossing scenarios. In (a), the states are not mixed by any transverse terms, so they remain eigenstates of the spin Hamiltonian through the real level crossing. The energy difference between the two states can be made arbitrarily close to 0. In (b), the states are mixed, and a tunnel splitting energy Δ exists between the states (*i.e.*, degeneracy never occurs). In this region, known as an avoided level crossing, the eigenstates of the spin Hamiltonian are composed of a superposition of both states, $|J_z\rangle$ and $|-J_z\rangle$. In fact, if the system remains within the level crossing, coherent tunneling between the two states occurs, even if the states sit below the anisotropy barrier of the double well potential. This is called quantum tunneling of magnetization (QTM). The rate at which this tunneling occurs is determined by the size of the tunnel splitting Δ and the strength of the magnetic field. When the Zeeman energy takes on values $-\Delta/2 < \mu_B g J_z B_z < \Delta/2$, the system is in resonance, and the tunneling rate is maximum. As the Zeeman energy departs from this range, the system is out of resonance and the rate drops off quickly. The general expression for this rate, derived by Villain *et al.*, is given by [123]:

$$W_{M,-M}^{QTM} = \frac{2\tau_M^* \omega_o^2}{1 + (\tau_M^* \omega_1)^2} \quad (2.54)$$

where $\omega_o = \Delta E_{M,-M}/\hbar$ in resonance, and $\omega_1 = \Delta E_{M,-M}/\hbar$ out of resonance. τ_M^* of state M is slightly more difficult to determine. It is inversely proportional to the sum of all outgoing scattering contributions from state M : $1/\sum_{M'} W_{MM'}$. The larger Δ is, the more efficient the tunneling process is. This is determined by the strength of the transverse terms in the spin Hamiltonian. Which states are mixed coincides with the order of the transverse term, and therefore the symmetry of the spin site (*e.g.*, cubic symmetry gives a fourth order term, and therefore mixes states separated by $\Delta m = \pm 4$, hexagonal symmetry gives a sixth order term, and therefore mixes states separated by $\Delta m = \pm 6$, etc.). Since state mixing reduces the total energy required for a magnetization reversal, it is integral to the stability of spin systems, and often determines the allowed relaxation pathways. Thus, the symmetry of the spin site is also of great importance. Equation 2.54 gives the tunneling rate for a constant magnetic field. When the field is varied at a constant rate, the Landau-Zener formula for diabatic transitions in a two state system gives the transition probabilities in an avoided level crossing [139]:

$$P_{LZ} = e^{-2\pi\Gamma} \quad (2.55)$$

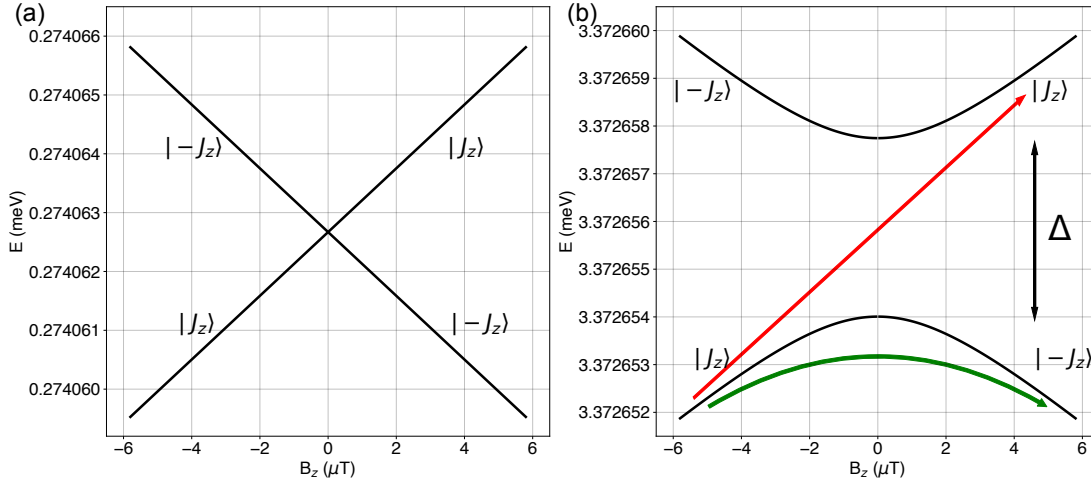


Figure 2.6: Real level crossing and avoided level crossing. In a two state system, $|J_z\rangle$ and $|-J_z\rangle$, a level crossing occurs at a given energy and magnetic field. (a), If $|J_z\rangle$ and $|-J_z\rangle$ are not mixed, they remain eigenstates of the spin Hamiltonian through the crossing and the energy difference between the states can be brought arbitrarily close to 0. (b), If the states are mixed, the eigenstates are a superposition of both $|J_z\rangle$ and $|-J_z\rangle$, with non-degenerate eigenvalues. The minimum difference of these eigenvalues is the tunnel splitting Δ . The red arrow indicates a Landau-Zener transition, where state $|J_z\rangle$ is maintained through the crossing. The green arrow indicates the opposite case, where no Landau-Zener transition occurs, resulting in a state reversal to the $|-J_z\rangle$ state. Level crossings in (a) and (b) are from the Dy SAM discussed in Chapter 3.

where

$$\Gamma = \frac{(\Delta/2)^2 / \hbar}{\frac{dB}{dt} \frac{d}{dB}(E_2 - E_1)} \quad (2.56)$$

dB/dt is the field sweep rate and $(E_2 - E_1)$ is the energy difference between the two states. P_{LZ} is the probability of a Landau-Zener transition, where the system 'jumps' the tunnel splitting Δ (indicated by the red arrow in Figure 2.6). In this case, the magnetic state $|J_z\rangle$ is maintained as the field is swept through the crossing. The probability of a Landau-Zener transition not occurring, and therefore a state to switch from $|J_z\rangle$ to $|-J_z\rangle$, is given by $1 - P_{LZ}$ (indicated by the green arrow in Figure 2.6). Clear from Equation 2.55, the probability is determined by the size of Δ and, most convenient to the experimentalist, the magnetic field sweep rate dB/dt . Thus, by tuning the sweep rate, the probability of a state switch can be adjusted. Equation 2.55 is particularly useful in the interpretation of XMCD magnetization curves, and can be used to determine the strength of the transverse mixing terms in the spin Hamiltonian.

This chapter has reviewed the tools, both experimental and mathematical, used to effectively study individual spin systems. In the following chapters, we will see how these tools can derive magnetic information from such systems, providing insight into the relevant interactions that ultimately determine their stability, motivating and directing the search for new systems.

3 Measuring the impact of the intra-atomic exchange

In 2016, XMCD measurements of Dy adatoms on graphene/Ir(111) indicated magnetic remanence and a spin lifetime of 10^3 s at 2.5 K and 10 mT [48]. These are consistent with a $J = 8$ total angular moment and a $J_z = \pm 7$ out-of-plane magnetic ground state [48, 50]. This stability is attributed to the high symmetry of the adsorption site and the presence of the graphene decoupling layer between the Dy and Ir(111). The Dy adsorbs in the 6-fold symmetric (C_{6v}) graphene hollow site [48], limiting state mixing and therefore reducing relaxation processes due to QTM. In addition, the high stiffness of the graphene layer, the weak coupling to the Ir(111) [140, 141], and the Dirac point close to the Fermi level imply a low scattering probability with substrate electrons and phonons, consistent with the relatively long lifetimes observed. However, the XMCD lifetime measurement represents a lower bound, as a 5-fold increase in photon flux results in a 4-fold decrease in lifetime [48]. Moreover, Dy adatoms on graphene/Ir(111), as other rare earth adatoms on graphene, show high-energy inelastic spectroscopic features, which are a consequence of the intra-atomic exchange between internal and external electronic shells [37]. Whether this exchange interaction affects the spin lifetimes, and influences the stability of the Dy SAM, remains obscured. Here, SP-STM is used to disentangle the mechanisms responsible for the spin dynamics of Dy adatoms on graphene/Ir(111) and demonstrate the critical role played by the intra-atomic exchange.

Work contribution. *A large portion of the results presented in this chapter are being submitted for publication in Curcella, Sblendorio et al. [142]. Measurements were taken by Dr. Curcella, Dr. Patthey, and myself. Analysis was done by myself. Modeling was done by Dr. Rusponi and myself. All authors were involved in writing and discussion.*

3.1 A choice of basis

Magnetism in rare earths mainly originates from the electrons in the $4f$ shell. Due to its strong spatial localization, occupation of the $4f$ orbitals is well described by Hund's rules, resulting in atomic-like spin and orbital moments. A spin polarization of the outer ($5d$ and $6s$) shells is also frequently observed, however, yielding only a small extra contribution to the

total momentum. Consequently, the rare earth's magnetic properties are usually described in terms of the total angular momentum of the $4f$ shell J^{4f} only. In particular, spin dynamics in single-ion magnets (SIMs) and single-atom magnets (SAMs) at surfaces is explained in terms of transitions between states defined by the J^{4f} projection on to the quantization axis $|J_{4f}^z\rangle$ [48, 49, 143–147] (4f model in the following).

Recent works [37, 148–152] have suggested that this description might be too crude. To fully capture the magnetism in bi-metallofullerenes [148], as well as the stability of some SIMs [149–151] and SAMs [152], one has to consider that the intra-atomic exchange ferromagnetically strongly couples the spins of the $4f$ and $5d6s$ shells [37]. With this in mind, the magnetic state of a rare earth atom is better described by the total atom angular momentum $J_{tot} = J^{4f} + S^{sd}$, where we have approximated the total angular momentum of the $5d6s$ shell by the spin momentum only since the orbital moment of these shells is either zero ($6s$) or strongly quenched ($5d$) by the hybridization with the surrounding atoms. Spin dynamics is then determined by the transition probabilities between states described by the projection of J_{tot} on the quantization axis given by $|m_i\rangle = |J_z^{4f}, S_z^{5d}, S_z^{6s}\rangle$ (4f5d6s model in the following).

The effect of the different Hilbert spaces associated to the two models is easily captured by considering that the intra-atomic exchange coupling between J^{4f} and S^{sd} is expected to behave as the hyperfine coupling between electron and nuclear spins, but on a different energy scale owing to the different strength of the two interactions. In this description, for a rare earth atom immersed in a crystal field with k -fold symmetry, QTM is observed between states differing by $\Delta M_{tot} = \Delta J_z^{4f} + \Delta S_z^{5d} + \Delta S_z^{6s} = kn$, $n \in \mathbb{Z}$ in place of the commonly assumed $\Delta J_z^{4f} = kn$.

With this in mind, the two approaches described above result in the energy schemes presented in Figure 3.1. Both energy schemes are consistent with previous XAS and XMCD measurements [48, 50], and IETS measurements of the intra-atomic exchange between the $4f$ and $5d6s$ shells [37]. In the 4f model, the ground doublet is protected from QTM; spin reversal can take place only via excitation to the split doublet originating from the mixing of the $J_z = \pm 6$ states. For the 4f5d6s model, DFT calculations provide values for the spin components of the external shells $S^{6s} = 0.23$ and $S^{5d} = 0.03$ [37]. To properly construct the Hilbert space, we assume half-integer spin for each shell such that $J_{6s} = S^{6s} = 1/2$ and $J_{5d} = S^{5d} = 1/2$. Compared to the 4f model, there are now two distinct pathways for magnetization reversal with different energy barriers governing the spin dynamics of the system.

3.2 The characteristic lifetime τ^*

We utilize SP-STM to distinguish between these two models. Constant-height current traces acquired on top of isolated Dy adatoms show a two-state telegraph signal (TS) [37]. Tunneling current switches between a high conductance (HC) and a low conductance (LC) state, corresponding to parallel and anti-parallel alignment of the majority spin states at the tip Fermi level and the adatom magnetization (Figure 3.2a). From a TS trace we extract the occupancy

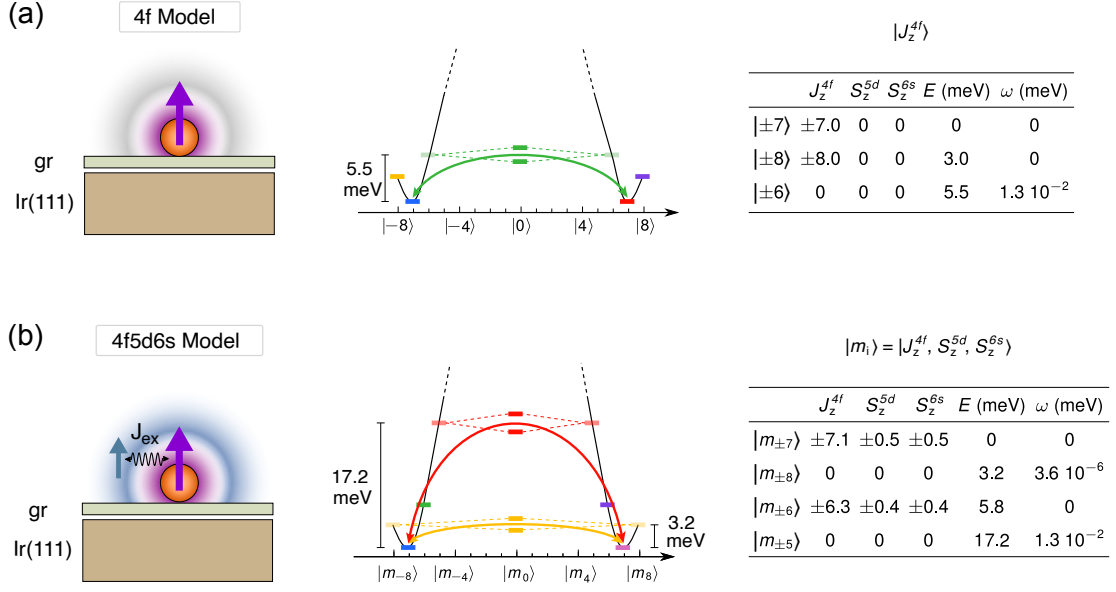


Figure 3.1: **Comparing 4f and 4f5d6s models.** (a), 4f model. Left: sketch of the spin polarization of the Dy electronic shells in the 4f model, that considers only the total angular momentum of the 4f shell (purple arrow). Middle: corresponding level scheme, where the states with the same color are mixed by the crystal field. The green arrow highlights the single QTM path available in this model. Right: out-of-plane projected eigenstates $|J_z^{4f}\rangle$, the corresponding eigenvalues E , and the energy splitting ω of the doublet states. (b), 4f5d6s model. Purple arrow total angular momentum of the 4f, blue arrow spin of the 6s and 5d shells (that are strongly exchange-coupled and can thus be considered as a single spin), J_{ex} between the two arrows represents the intra-atomic exchange coupling. The 4f5d6s model is characterized by QTM paths via two split-doublet states (± 8 yellow and ± 5 red arrows). Table: out-of-plane projected J and S .

of HC and LC states, and the a single effective lifetime τ^* [46]. For brevity, we use indices i and j to refer to the low (LC) and high (HC) conductance states. The probability of switching from i to j at time t is given by p_{ij} , while the probability of remaining in the same state is given by p_{ii} . We neglect any transient state such that: $p_{ij} + p_{ii} = 1$. The time evolution of p_{ii} after time dt is given by:

$$\begin{aligned}
 p_{ii}(t+dt) &= p_{ij}(t) \frac{dt}{\tau_j} + p_{ii}(t) \left(1 - \frac{dt}{\tau_i}\right) = (1 - p_{ii}(t)) \frac{dt}{\tau_j} + p_{ii}(t) \left(1 - \frac{dt}{\tau_i}\right) \\
 &= p_{ii}(t) + \frac{dt}{\tau_j} - p_{ii}(t) \frac{dt}{\tau^*}
 \end{aligned} \tag{3.1}$$

where $p_{ij}(t) \frac{dt}{\tau_j}$ represents the fraction of lifetime measurements of τ_i that contain a switch after time dt while $p_{ii}(t) \left(1 - \frac{dt}{\tau_i}\right)$ represents the fraction that do not contain a switch, for a system governed by an effective lifetime defined as $\frac{1}{\tau^*} \equiv \frac{1}{\tau_i} + \frac{1}{\tau_j}$. Simplifying further from (3.1)

gives:

$$\frac{dp_{ii}(t)}{dt} = \frac{1}{\tau_j} - \frac{p_{ii}(t)}{\tau^*} \quad (3.2)$$

$$p_{ii}(t) = \frac{\tau^*}{\tau_j} - c_1 \exp\left(-\frac{t}{\tau^*}\right) = \frac{\tau^*}{\tau_j} - \frac{\tau^*}{\tau_i} \exp\left(-\frac{t}{\tau^*}\right) \quad (3.3)$$

where we use the condition $p_{ii}(0) = 1$ to determine the value of the constant $c_1 = \frac{\tau^*}{\tau_i}$. Note that Equation 3.2 is completely independent of the initial state i . Thus, the quantity τ^* governs the time evolution of both LC and HC states. The factors $\frac{\tau^*}{\tau_j} = \frac{\tau_i}{\tau_i + \tau_j}$ and $\frac{\tau^*}{\tau_i} = \frac{\tau_j}{\tau_i + \tau_j}$ are the occupancies of the state i and j , respectively.

TS traces are taken with the STM feedback loop open and initialized in the low conductance state. In order to have significant statistics, TS traces are acquired consecutively over several hours (12+ total in Figure 3.2b and 10+ in Figure 3.3a-c), to count at least 300 switches between LC and HC states for each data point. Since the stray field of the tip strongly influences our results, each set of measurements has been acquired with the same tip apex, which is quite challenging given the times mentioned above. Lifetimes of the LC state τ_{LC} and HC state τ_{HC} are determined by fitting the histograms of residence times. Error bars on τ^* and the occupancies are propagated from error bars calculated on τ_{HC} and τ_{LC} , corresponding to 95% confidence intervals constructed using the normal approximation interval.

By varying temperature T and bias voltage V_b , we tune the efficiency of the scattering of the Dy spin with substrate electrons and phonons, as well as with tunneling electrons. This allows us to investigate the spin dynamics of the surface supported adatom both in reading conditions, *i.e.* without external perturbations, and under writing conditions realized by injecting spin polarized currents in the hope of distinguishing which model best describes the system.

3.3 Distinguishing between the two models

The temperature-dependent spin reversal rate is presented in Figure 3.2c in an Arrhenius plot. In order to address the intrinsic lifetimes, the measurements have been performed under reading conditions at bias $V_b = 1$ mV, well below the energy of the first excited doublet and at a low set-point current of $I_t = 10$ pA to avoid spin-pumping by tunneling electrons [40, 41, 46]. $1/\tau^*$ increases with increasing temperature, as expected for thermally assisted reversal mechanisms. The data show a transition between a shallow slope at low T and a much steeper one at high T with the change occurring around 8.3 K. This observation indicates the presence of two different reversal paths, each characterized by its own activation energy. Already from a qualitative inspection of Figure 3.1, this rules out the 4f model that contains only one such transition, and therefore gives rise to only one slope (green line in Figure 3.2c).

The change in slope observed in the experimental data is very well reproduced by the spin

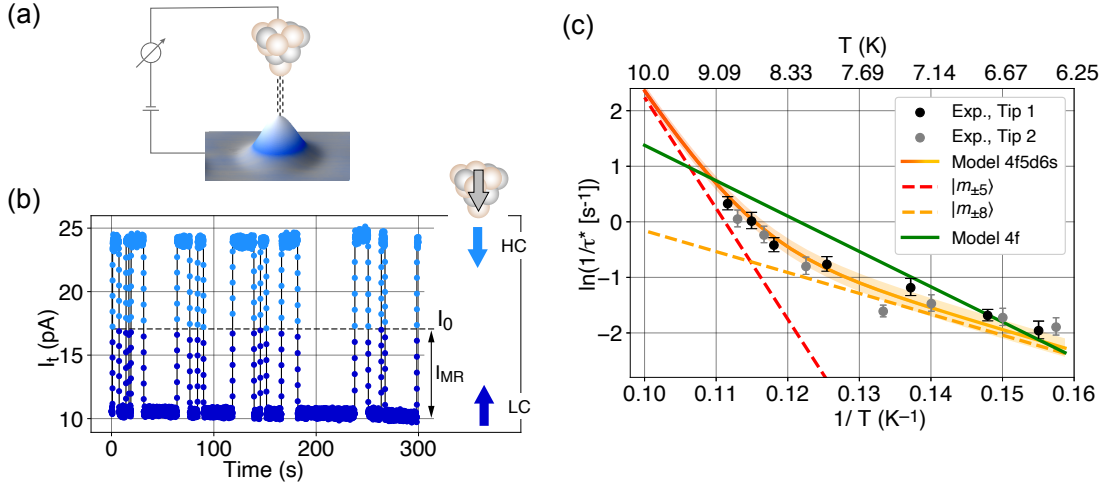


Figure 3.2: Reading the magnetic quantum states of Dy SAMs. (a), Sketch illustrating the STM tip and a 3D-rendered STM image of a Dy adatom on gr/Ir(111). (b), TS trace showing the switching between HC and LC states ($T = 6.3$ K, $V_b = 1$ mV, set current $I_t = 10$ pA in the LC state). The elastic current I_0 is the non-magnetic contribution, and the magnetoresistive component I_{MR} is the absolute difference between I_0 and I_{LC} (or I_{HC}). Sketch of the alignment of tip and Dy magnetization in the HC and LC states. (c), Arrhenius plot of the spin reversal rate (experimental black and grey dots, $V_b = 1$ mV, set current $I_t = 10$ pA, in the LC state) with fits using the 4f5d6s (red/yellow shaded curve) and 4f (green curve) models (tip polarization $\rho_T = -0.8$, $B_{tip} = -60$ mT in both cases). The data show a transition between a shallow slope at low T and a much steeper one at high T with the change occurring around 8.3 K. The shaded area shows the accuracy of the fit with variations of the tip magnetic field within ± 5 mT. The yellow and red dashed lines show the temperature dependence of τ^* with QTM exclusively via $|m_{\pm 8}\rangle$ or $|m_{\pm 5}\rangle$, respectively. Experimental error bars correspond to 95 % confidence intervals calculated using the normal approximation interval.

reversal rates calculated with the 4f5d6s model. At low temperatures, scattering with substrate electrons induces spin transitions ($\Delta m = \pm 1$) driving the Dy spin from the ground-state ($|m_{\pm 7}\rangle$) to the first excited doublet ($|m_{\pm 8}\rangle$), from whence the magnetization reverses via QTM. Note that these states are not mixed in the 4f model, as the six-fold symmetry of the adsorption site forbids it. As we increase the temperature, higher energy states become thermally populated, including the high energy split doublet $|m_{\pm 5}\rangle$. Despite being much less populated than the $|m_{\pm 8}\rangle$, the larger energy splitting of the $|m_{\pm 5}\rangle$ states results in a more efficient QTM (see Section 3.4.4). The transition via $|m_{\pm 5}\rangle$ starts to be activated at about 8.3 K, has a nearly equal weight compared to QTM via $|m_{\pm 8}\rangle$ at roughly 9 K, and largely dominates for $T \geq 10$ K. Conversely, the 4f model, with a single QTM channel between $|\pm 6\rangle$ (Figure 3.1a), shows a single slope (green line) and, consequently, cannot reproduce the experimental trend.

The outer shell polarization plays an equally relevant role in the spin dynamics under writing conditions, as highlighted by the spin-torque experiments reported in Figure 3.3a-c, where spin lifetime, occupancy, and magnetoresistance are reported as a function of bias voltage, at a fixed temperature $T = 6.7$ K. The experimental data show small τ^* variations and an almost

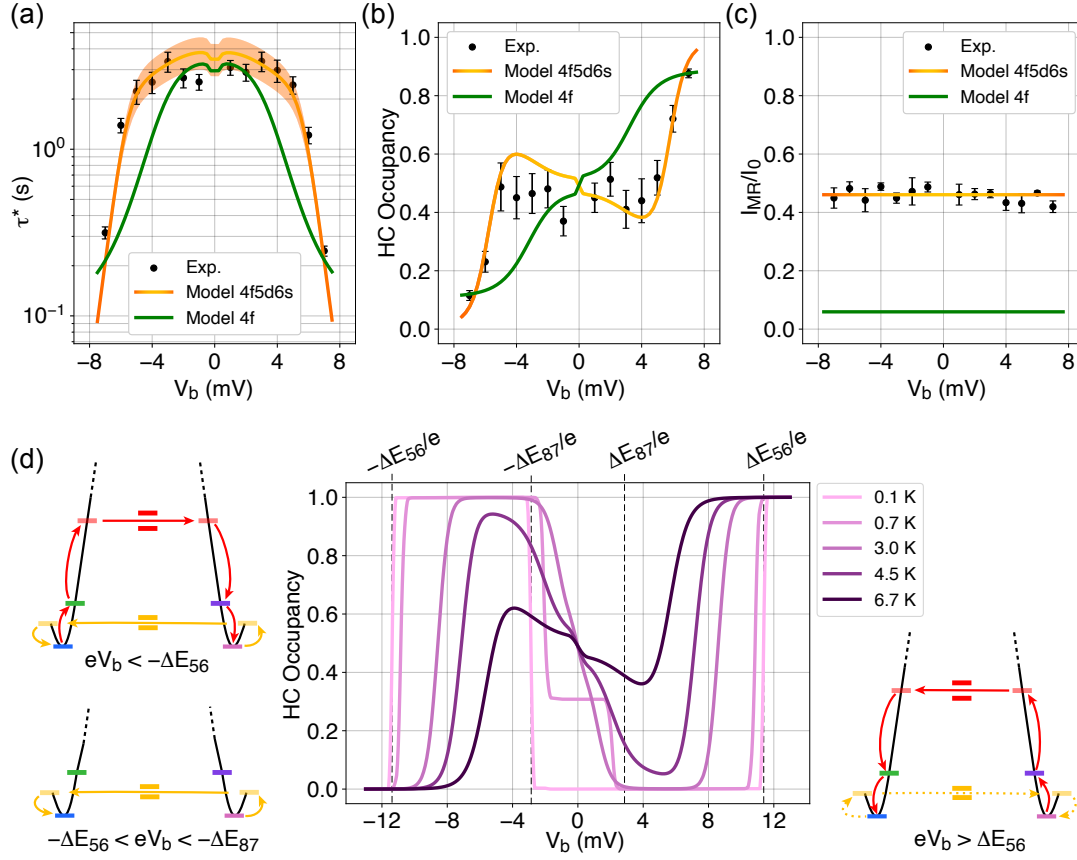


Figure 3.3: Writing the magnetic quantum states of Dy SAMs. (a), Spin lifetimes, (b), occupancy and (c), fraction of magnetoresistive to elastic component ratio of the tunneling current as a function of bias V_b (black dots and error bars, $T = 6.7$ K, set current $I_t = 10$ pA in the LC state). Continuous lines correspond to calculations performed, in the experimental conditions, with the 4f5d6s model (red to orange shaded depending on the weight of the ± 8 or the ± 5 QTM) and the 4f model (green), using $B_{tip} = -45$ mT, $\rho_T = -0.8$, and ζ_S and ζ_T given by Table 3.2 and Equation 3.10. The shaded area shows the accuracy of the fit with variations of tip magnetic field within ± 5 mT. Error bars correspond to 95 % confidence intervals calculated using the normal approximation interval. (d), HC occupancy, at different temperatures, derived from the 4f5d6s model for a fully spin-down polarized tip ($B_{tip} = -45$ mT, $\rho_T = -1.0$). Sketches on the left (right) highlight the spin pathways for the indicated negative (positive) bias settings (a Dy spin-up $|m_7\rangle$ configuration is favoured by the tip magnetic field).

50%-50% flat occupancy for $|V_b| \leq 5$ mV, while the spin lifetime is strongly reduced, and strong spin torque effects are observed at higher biases (Figure 3.3a, b). The experimental behavior, especially in Figure 3.3a and c, is very well reproduced by the 4f5d6s model, while the 4f model shows an earlier decrease of τ^* , fails to reproduce the non-monotoneous behavior of the HC occupancy, and largely underestimates the magnetoresistance.

The thermal broadening of about $5k_B T = 2.9$ meV at our experimental conditions and the partial tip polarization smear out the bias-dependent effects. Figure 3.3d shows the HC occu-

pancy as a function of bias voltage, calculated with the 4f5d6s model at different temperatures, and for a fully spin-down polarized tip ($\rho_T = -1.0$). Note that the stray field of this tip points up.

At 0.1 K, due to the tip magnetic field, only the ground state $|m_7\rangle$, with the Dy moment pointing up, is occupied. For $|V_b| < 3.2$ mV, the system remains frozen in the LC ground state. Increasing $|V_b|$, opens up inelastic scattering to higher energy states, progressively activating additional reversal pathways. Because the tip is fully spin-down polarized, a tunneling electron induces Dy spin transitions with $\Delta m = +1$ ($\Delta m = -1$) for negative (positive) bias. At a negative bias of $eV_b = -\Delta E_{87} = E(|m_8\rangle) - E(|m_7\rangle) = -3.2$ meV, tunneling electrons promote transitions to $|m_8\rangle$, from where the Dy spin tunnels through the barrier to $|m_{-8}\rangle$ (see corresponding sketch on the lower left in Figure 3.3d). From $|m_{-8}\rangle$, the spin easily relaxes to $|m_{-7}\rangle$. Backward paths are forbidden since i) the tunneling current only generates spin-increasing transitions, thus preventing the way back via $|m_{-7}\rangle$ to $|m_{-8}\rangle$; ii) at this bias the electron energy is not enough to promote transitions from $|m_{-7}\rangle$ to $|m_{-6}\rangle$ and farther to the top of the barrier; iii) spin scattering with phonons and surface conduction electrons has negligible effect at this temperature. As a result, the Dy spin state switches from $|m_7\rangle$ to $|m_{-7}\rangle$, corresponding to a HC occupancy of 1 (spin pumping). Moving to farther negative bias, tunneling electrons can promote transitions from $|m_{-7}\rangle$ to $|m_{-6}\rangle$ and successively, for $eV_b \leq -\Delta E_{56} = E(|m_{-5}\rangle) - E(|m_{-6}\rangle) = -11.4$ meV, from $|m_{-6}\rangle$ to $|m_{-5}\rangle$. QTM then induces transitions to $|m_5\rangle$, from where the spin can easily relax to $|m_7\rangle$ (HC = 0). Note that for $eV_b \leq -\Delta E_{56}$ the Dy spin cyclically reverses under the effect of a continuous tunneling current (see corresponding sketch on the upper left in Figure 3.3d); the probability of finding it in the $|m_7\rangle$ state is nevertheless largely dominant. Writing can be obtained by simply stopping the injection of tunneling current in the desired HC or LC state as identified via I_{MR} . At positive bias, tunneling electrons first generate transitions from $|m_7\rangle$ to $|m_6\rangle$, without a change in the HC value, and next, for $eV_b \geq \Delta E_{56} = E(|m_5\rangle) - E(|m_6\rangle) = 11.4$ meV, from $|m_6\rangle$ to $|m_5\rangle$. The spin can then tunnel to $|m_{-5}\rangle$, from where it relaxes to $|m_{-7}\rangle$. Again, under the effect of a continuous tunneling current the spin will cyclically switch back to the $|m_7\rangle$ state, via the yellow dotted path shown in the right sketch of Figure 3.3d. However, the probability of finding it in the $|m_{-7}\rangle$ state is largely dominant. Also in this case, writing can be realized through opportune synchronization of tunneling current injection with the spin state, read via I_{MR} . At higher T , both states of the ground doublet and possibly also higher states are partially populated, smearing the energy threshold of the involved processes; however, the hierarchy of the processes remains unchanged.

Conversely, the 4f model cannot reproduce the experimental observations. Tunneling electrons start to induce spin transitions above 5.5 meV ($|\pm 7\rangle$ to $|\pm 6\rangle$ energy barrier). However, temperature smearing and partial tip polarization result in a monotonic and almost linear occupancy trend (green line, Figure 3.3b). Moreover, the simulated lifetimes already start dropping at ± 2 mV, and the magnetoresistive current I_{MR} is largely underestimated, as shown in Figure 3.3a and c, respectively.

Thus, the 4f5d6s model better describes the system, and motivates the necessity of including the intra-atomic exchange to correctly describe spin lifetimes and reading/writing mechanisms in rare-earth adatoms. The intra-atomic exchange between spin-polarized shells defines the total angular momentum and, thus, the QTM channels available for magnetization reversal. In the following sections, construction of the model is discussed.

3.4 Modeling the spin system

3.4.1 The spin Hamiltonian

In order to determine the magnetic quantum states in the presence of the intra-exchange between the 4f shell and outer shells, the Zeeman energy created by the tip field, the crystal field of the adsorption site, as well as their dynamics under the influence of phonon and electron scattering, we use a Hamiltonian of the following form

$$\mathcal{H} = \mathcal{H}_{intra} + \mathcal{H}_Z + \mathcal{H}_{CF} + \mathcal{H}_{ph} + \mathcal{H}_{te} \quad (3.4)$$

The first term describes the intra-atomic exchange between the partially filled 6s, 5d, and 4f shells. This term, given by Equation 2.24, is the primary novelty of our model and it stems from the recent observation that the external 6s and 5d shells are polarized and only partially filled [37]. The interaction between each shell is considered, thus Equation 2.24 has three terms corresponding to the 4f-5d, 4f-6s, and 5d-6s exchange. For the 4f5d6s model, the magnitude of the exchange between each shell A_{ij}^{ex} is taken from DFT calculations [37, 153]. We need $J_{6s} = S_{6s} = 1/2$ and $J_{5d} = S_{5d} = 1/2$ to properly construct the Hilbert space in the model. The real spin values in these shells are not necessarily 1/2. We take this into account by adapting A_{ij}^{ex} to match the energy of high energy excitations reported in Ref. [37]. Note that for non-polarized external shell (4f model) this term gives a vanishing contribution.

The second term is the Zeeman term of the form of Equation 2.31, describing the influence of a stray magnetic field from the STM tip on the Dy adatom. As its orientation is unknown and as the in-plane component only affects the spin-dynamics above (an unrealistically high value of) 1 T, we consider only a constant out-of-plane component such that, hereafter, B^{tip} indicates B_z^{tip} . We rescale the g -factor for each shell such that the magnetic moments of each shell are consistent with DFT calculations and XMCD spectra [37, 50]. The values are 1.25, 0.54, and 0.54 for the 4f, 5d, and 6s shells, respectively. In the 4f model, the only non-vanishing contribution is the one acting on the internal 4f shell.

The effects of the crystal field are described by the third term of the form of Equation 2.39. The crystal field only acts on the internal 4f shell, the only shell with a non-vanishing orbital magnetic moment. We assume that in the 4f5d6s model the orbital moment of the 5d shell is quenched due to hybridization with graphene π -bands [154]. Due to the sixfold symmetry of

the adsorption site, \mathcal{H}_{CF} can be expressed as the sum of four Stevens operators \hat{O}_m^n [48, 112]:

$$\mathcal{H}_{CF} = B_2^0 \hat{O}_2^0 + B_4^0 \hat{O}_4^0 + B_6^0 \hat{O}_6^0 + B_6^6 \hat{O}_6^6 \quad (3.5)$$

where the parameters B_2^0 , B_4^0 , and B_6^0 determine the total zero field splitting and B_6^6 determines the mixing of the magnetic states. The 4f model values have been taken from Ref. [50] while the 4f5d6s model values are adjusted to take into account the additional spin of the 6s and 5d shells. These values are listed in Table 3.1.

Model	B_2^0 (μeV)	B_4^0 (neV)	B_6^0 (neV)	B_6^6 (neV)
4f	-121	100	1.5	0.3
4f5d6s	-518	1047	-0.476	-7.5

Table 3.1: CF Stevens Parameters for the 4f and 4f5d6s models

In both cases, these values are fixed by the size and location of the steps in the XMCD magnetization curves at ± 2.7 T and ± 5.6 T, which indicate the presence of QTM processes due to level crossings in the energy level diagram. This is discussed in detail in Section 3.6.

The first three terms discussed so far are the unperturbed Hamiltonian. The fourth term is a perturbation due to spin-phonon coupling that occurs between the Dy adatom and the graphene [126, 128]. In the spirit of Equation 2.41, we utilize a perturbation of the form:

$$\phi_{CF}^{(1)} = \hat{S}_{4f,-}^2 + \hat{S}_{4f,+}^2 + \{\hat{S}_{4f,-}, \hat{S}_{4f,z}\} + \{\hat{S}_{4f,+}, \hat{S}_{4f,z}\} \quad (3.6)$$

where $\{, \}$ denotes the anticommutator between the two operators, and $\hat{S}_{4f,+}$, $\hat{S}_{4f,-}$ are the spin ladder operators. Phonons that scatter with the Dy adatom can be treated as perturbations of the crystal field. Similar to \mathcal{H}_{CF} , this term acts only on the internal 4f shell, the only one carrying an orbital component. The orbital moment of the external shells is trivially zero for the 4f model (non-polarized external shell), while it is quenched for the 5d shell in the 4f5d6s model due to hybridization with graphene bands [154]. As discussed in Section 2.2.5, the specific form of \mathcal{H}_{ph} is dependent upon the phonon modes considered and the crystal field symmetry of the adsorption site. Considering only terms linear in strain, $\phi_{ph}^{(1)}$ is composed of terms which produce either first order or second order transitions. The specific weight of each term is proportional to a direction-dependent magnetoelastic coupling [119]. Since this coupling between the Dy adatom and the graphene is unknown, we simply adopt a form of $\phi_{ph}^{(1)}$ that considers both first and second order transitions: the third and fourth term account for first order transitions ($\Delta S = \pm 1$) and the first and second term account for second order transitions ($\Delta S = \pm 2$). Direct, Orbach, and Raman processes were all considered in the fitting the experimental trends. As discussed further in Section 3.4.3, the presence of *any* significant phonon contribution competes with the asymmetry in occupancy at high tunnel bias in Figure 3.3b. Regardless, the small direct phonon contribution is included in the description for completeness. These scattering rates are given by the direct rates of Equation 2.48.

The final term of the Hamiltonian describes the scattering of tunneling electrons with electrons in the outer 6s shell. We use the Kondo-like Hamiltonian of Equation 2.49. In the 4f5d6s model, electron scattering induces spin transitions in the external 5d6s shells. Consequently, the magnetic moment of the 4f shell flips due to the intra-atomic exchange coupling between the shells [37]. Since the substrate has no spin polarization at the Fermi level, e_{SS} scattering events induce symmetric $\Delta m = \pm 1$ transitions and therefore promote equal occupancy between HC and LC states. In the case of tip-tip scattering, the creation or annihilation of an electron hole pair in the tip induces a spin transition ($\Delta m = \pm 1$) in the external 5d6s shell. If the tip is spin polarized at the Fermi level, e_{TT} scattering induces spin-increasing ($\Delta m = +1$) or spin-decreasing ($\Delta m = -1$) transitions in the Dy adatom, for a tip density of states of spin-up electrons of $\rho_{T\uparrow} > 0.5$ and $\rho_{T\uparrow} < 0.5$, respectively.

The electrons that participate in tip-substrate/substrate-tip scattering (e_{TS}/e_{ST}) also induce asymmetric spin transitions due to the spin polarization of the tip. These processes define the inelastic component of the current (I_{in}). The electrons that tunnel through the junction without inducing spin transitions determine the elastic (I_0) and magnetoresistive (I_{MR}) components of the tunneling current [136]. Despite being the only component actively contributing to the spin transitions in the Dy adatoms, I_{in} is orders of magnitude smaller than the elastic components. Thus, in the TS traces we approximate the current of the HC state and LC states as $I_0 + I_{MR}$ and $I_0 - I_{MR}$ (Figure 3.2b).

3.4.2 Master equation

The rates in Equations 2.48, 2.50, and 2.54, are used in a master equation to obtain the diagonal elements of the density matrix, P_M :

$$\frac{dP_M}{dt} = \sum_M P_{M'} W_{MM'}^{el-ph} - P_M \sum_{M'} W_{MM'}^{el-ph} + W_{M,-M}^{QTM} (P_{-M} - P_M) \quad (3.7)$$

in which $W_{MM'}^{el-ph}$ are the total electron-phonon transition rates:

$$W_{MM'}^{el-ph} = W_{MM'}^{TS} + W_{MM'}^{ST} + W_{MM'}^{TT} + W_{MM'}^{SS} + W_{MM'}^{ph} \quad (3.8)$$

The populations derived in Equation 3.7 can then be used to estimate the ratio of the magnetoresistive to the elastic tunneling current picture in Figure 3.3c [136]:

$$I_{MR}/I_0 = 2\zeta \frac{\rho_{T\uparrow} - \rho_{T\downarrow}}{\rho_{T\uparrow} + \rho_{T\downarrow}} \frac{\sum_M \tilde{P}_M \langle M | \hat{S}_{6s,z} | M \rangle}{\sum_M \tilde{P}_M} \quad (3.9)$$

in which \tilde{P}_M represents the equilibrium population of the state $|M\rangle$ and $\frac{\rho_{T\uparrow} - \rho_{T\downarrow}}{\rho_{T\uparrow} + \rho_{T\downarrow}}$ is the tip polarization ρ_T . The description above is also valid in the case of the 4f model, provided we replace the $\hat{S}_{6s,\alpha}$ with $\hat{S}_{4f,\alpha}$ (*i.e.* the electrons scatter directly with the internal 4f shell). This of course changes the value of the matrix elements involving the spin operators, resulting in a

Table 3.2: Fitting parameters used for the 4f5d6s and 4f models

Model	Measurements	B_{tip} (mT)	ζ	ν_{ph}	ζ_S	ρ_T
4f5d6s	Arrhenius	-60 ± 5	0.65	2×10^{-4}	6.5×10^{-2}	-0.8
	Bias	-45 ± 5	-	-	-	-
4f	Arrhenius	-60 ± 5	0.005	1×10^{-6}	6×10^{-2}	-0.8
	Bias	-45 ± 5	-	-	-	-

much lower value of the fitting parameter ζ in the 4f model compared to the 4f5d6s one. This is discussed further in Section 3.4.3.

3.4.3 Fitting parameters

In both the 4f and 4f5d6s model, we choose the fitting parameters that best fit the experimental data. These parameters are listed in Table 3.2. We expect ζ , ν_{ph} , and ζ_S to be independent of measurement conditions within the temperatures and biases probed, while the tip field B_{tip} is allowed to slightly vary for different measurement sets recorded with different tip apexes. The field values used are in agreement with the estimations for MnNi tips reported in Ref. [100, 103]. As indicated with the shading in Figure 3.2b and Figure 3.3a, small fluctuations in B_{tip} produce a noticeable difference in expected lifetime at low temperature and bias. For this reason, we expect any deviations between the experimental points and model predictions to be primarily caused by changes in B_{tip} . In addition, larger field values increase the occupancy asymmetry in the bias regime between $-3.2 \text{ meV} = -\Delta E_{87} < eV_b < \Delta E_{87} = 3.2 \text{ meV}$ due to the lack of available spin pumping pathways. The effect is stronger the closer V_b is to 0 mV due to thermal broadening. This includes the two measurement sets, Tip 1 and Tip 2, in Figure 3.2c, both taken at 1 mV. Figure 3.4a displays the HC occupancy of these two measurement sets and the corresponding 4f5d6s model prediction. Using a value of $B_{tip} = -60 \text{ mT}$ gives reasonable agreement with the experimental points.

From Equations. 2.51 and 3.9, it is clear that ζ defines the electron scattering strength and determines as well the magnitude of the magnetoresistive component of the current. The electron scattering rates scale with ζ^2 , while the magnetoresistive current scales with ζ . In the 4f model, we have to assume that the scattering occurs directly with the internal 4f shell, and therefore need a low value of ζ to compensate for the high value of $|\langle M' | \hat{S}_{4f,\alpha} | M \rangle|^2$. This results in the underestimation of the magnetoresistive current for the 4f model. This problem is not present in the 4f5d6s model, in which the electronic scattering occurs with the external 6s shell. We find a value similar to the ones reported in Refs. [40, 136, 155] that fits the experimental trends as a function of temperature and bias, and correctly predicts I_{MR}/I_0 .

The parameter ν_{ph} describes the magnetoelastic coupling between the Dy adatom and the graphene. The presence of phonons competes with the asymmetry in occupancy in the high bias regime. Thus, in both the 4f and 4f5d6s models, we find that a minimal phonon

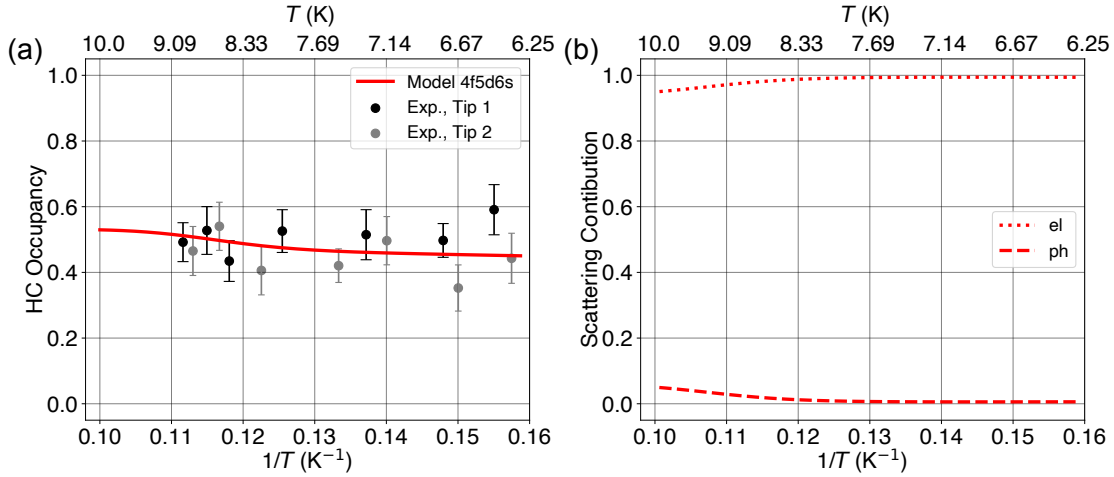


Figure 3.4: **HC occupancy and electron and phonon scattering contribution.** (a), HC occupancy as a function of $1/T$ (black and gray dots and bars, $V_b = 1$ mV, set current $I_t = 10$ pA in the LC state). Continuous red line corresponds to calculations based on the 4f5d6s model using $B_{tip} = -60$ mT, $\rho_T = -0.8$. Experimental error bars correspond to 95 % confidence intervals calculated using the normal approximation interval. (b), The electron (el) and phonon (ph) scattering contribution to the spin reversal rate in the Arrhenius plot of τ^* in the main text and in (a) ($1/\tau_{el+ph}^* = 1/\tau_{ph}^* + 1/\tau_{el}^*$). Each scattering contribution is calculated as the ratio of $1/\tau_{el/ph}^*$ to $1/\tau_{el+ph}^*$.

contribution to the total scattering best describes the system. Direct and Orbach processes are more dominant than Raman processes at temperatures below 10 K [117, 120, 129], so the direct rates of Equation 2.48 are still included in Equation 3.7. The phonon contribution remains below 10% for the temperature range probed, as pictured in Figure 3.4b. This is consistent with the high stiffness of graphene limiting phonon scattering with the Dy adatom. Any higher phonon contribution would compete with the spin-torque effect pictured in Figure 3.3b, and would reduce the occupancy to values inconsistent with what is experimentally observed.

The four types of electron scattering described by Equation 2.51 are dependent on the tip-adatom and substrate-adatom transmission coefficients ζ_T and ζ_S . As described in Refs. [136, 155], these transmission coefficients are dependent on tip-adatom and substrate-adatom hopping integrals and the Coulomb potential scattering interaction T_o . The value of ζ_T is fixed by the experimental value of the elastic current I_0 and by the choice of the substrate-adatom transmission coefficient ζ_S , which we keep as a fitting parameter. From Delgado *et al.*:

$$\zeta_T = \frac{4\hbar I_0}{2e\pi\zeta_S(F(0, eV_b) - F(0, -eV_b))(\rho_{S\downarrow}\rho_{T\uparrow} + \rho_{S\uparrow}\rho_{T\downarrow})} \quad (3.10)$$

in which F is Equation 2.52. As evident from Equation 3.10, the elastic current is proportional to $\zeta_T\zeta_S$, while substrate-substrate scattering and tip-tip scattering are proportional to ζ_S^2 and ζ_T^2 , respectively. While both coefficients are unknown, fixing ζ_S , which we assume to be independent of any measurement conditions, allows for the determination of ζ_T , thereby

reducing the number of fitting parameters needed. Note that the distance dependence of ζ_T , as expected from a hopping integral dependency, is built in to Equation 3.10 for a set of tunneling parameters I_t and V_b . Unlike ζ , ζ_S has a non-trivial effect on the determination of τ^* for changing tunneling parameters I_t or V_b . While this is not relevant for the measurements taken as a function of temperature, as ζ_S simply scales e_{ST}/e_{TS} linearly and e_{SS} quadratically for all temperatures, it is relevant for the measurements taken as a function of tunnel bias V_b . Within the context of the measurements shown in Figure 3.3a, an increase in ζ_S has the effect of decreasing the lifetimes at lower biases (by increasing the strength of substrate scattering), and increasing the lifetimes at higher biases (by decreasing the strength of tip scattering through Equation 3.10). This has the effect of "squeezing" the total range of τ^* spanned in the bias range probed. A decrease in ζ_S has the opposite effect—where the total range of τ^* spanned is "stretched." A modest change of ζ_S by $\pm 10\%$ produces a trend inconsistent with experimental observations. This behavior is true for both the 4f model and the 4f5d6s model. However, it is important to note that this does not influence the fundamental shape of the trend in either case, which is derived solely from the available QTM pathways. Similar to B_{tip} , ρ_T can vary for different measurement sets, resulting in variations in the observed I_{MR} . While the value of ρ_T has a very limited effect on τ^* , as it does not change the total electron scattering strength, it determines the saturation occupancy at high biases in Figure 3.3b. Thus, we match the HC occupancy and I_{MR} experimentally observed, and find a value of $\rho_T = -0.8$ for all measurement sets. This is consistent with calculations of other Mn-based alloys, which calculate 100% polarization at the Fermi energy [156, 157].

3.4.4 Transition rates

To better illustrate the dynamics governing the system, we report the product of equilibrium state occupation and rates (*i.e.* $\tilde{P}_{M'} W_{MM'}^{el-ph}$) for several regimes. Figure 3.5 corresponds to the Arrhenius plot for the low temperature (4f model in (a) and 4f5d6s model in (c), 6.3 K) and the high temperature (4f model in (b) and 4f5d6s model in (d), 10 K) regime. In the low temperature case of the 4f model, the dominant pathway from the ground state $|7\rangle$ that results in a magnetization reversal is $|7\rangle \rightarrow |6\rangle \rightarrow |-6\rangle \rightarrow |-7\rangle$. This is indicated in green in Figure 3.5a. Note that the transition $|7\rangle \rightarrow |8\rangle$ has a larger rate than the $|7\rangle \rightarrow |6\rangle$ transition, yet this does not result in magnetization reversal as the dominant transition from $|8\rangle$ is back to $|7\rangle$. In a similar fashion, the system can relax back to $|7\rangle$ from the $|6\rangle$ state, or traverse the magnetization barrier by tunneling to $|-6\rangle$. The latter results in a reversal, and is favored by at least a factor of 20 to other transitions that also result in a reversal. A similar situation is present in the high temperature case in Figure 3.5b. As expected at higher temperatures, the absolute values of the rates are larger, reflected in lower values of τ^* , but the preferred pathway for magnetization reversal remains the same: $|7\rangle \rightarrow |6\rangle \rightarrow |-6\rangle \rightarrow |-7\rangle$. QTM from $|6\rangle$ to $|-6\rangle$ dominates by a factor of about 20.

In the low temperature case of the 4f5d6s model, we see that the transition from the ground state $|m_7\rangle$ to $|m_8\rangle$ dominates (yellow in Figure 3.5c). From $|m_8\rangle$, magnetization reversal occurs

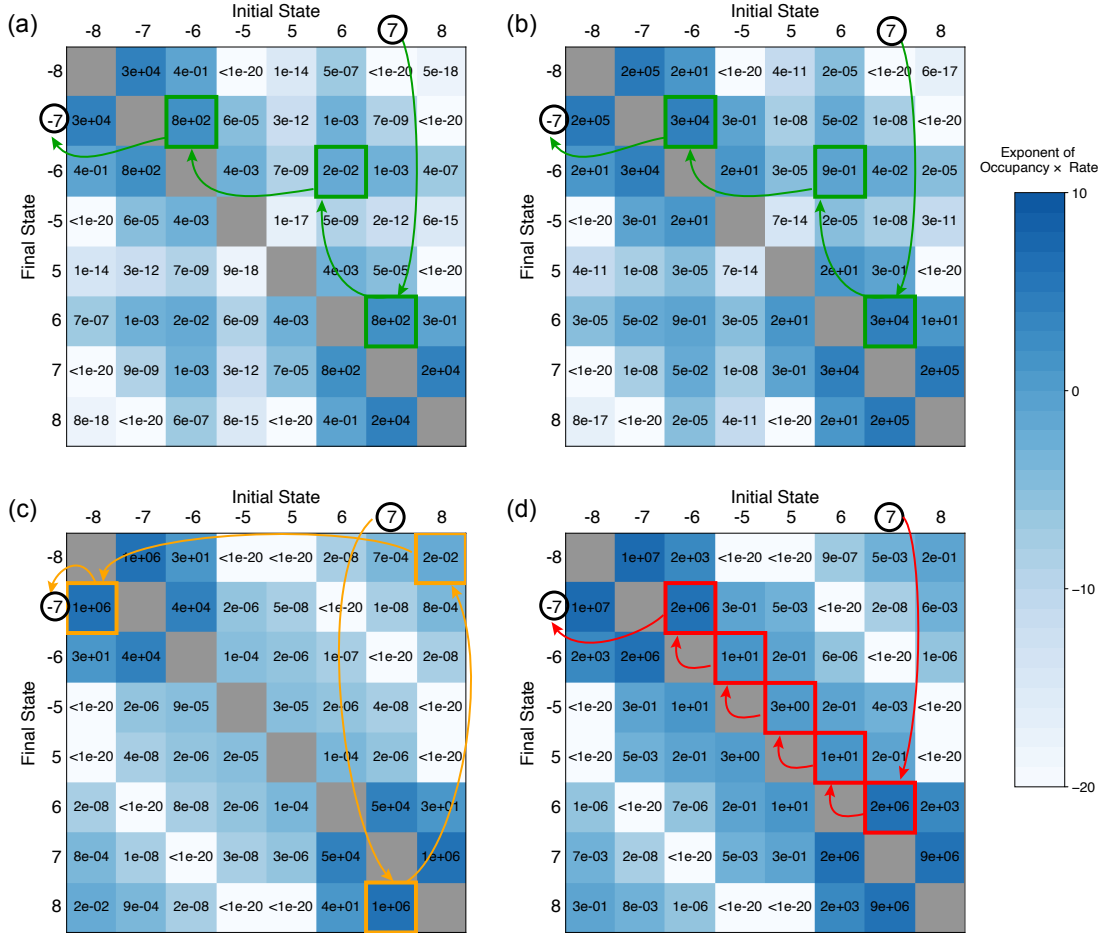


Figure 3.5: Transition rates of the 4f vs 4f5d6s model. The product of state occupation and rate (i.e. $\tilde{P}_{M'} W_{MM'}^{el-ph}$) in equilibrium for the 4f model at (a) 6.3 K and (b) 10 K and for the 4f5d6s model at (c) 6.3 K and (d) 10 K corresponding to the Arrhenius plot in Figure 3.2b. The value is given if larger than 10^{-20} , and the relative strength is indicated through blue shading. Colored arrows and boxes indicate dominant reversal pathways for the 4f model (green) and the 4f5d6s model (yellow and red). At the tip field used for both models, $B_{tip} = -45$ mT, the ground state for the 4f model is $|7\rangle$ and $|m_7\rangle$ for the 4f5d6s model.

through the lower energy QTM pathway to $|m_{-8}\rangle$. This transition is favored by a factor of 25 relative to other transitions that result in a reversal. Even at this temperature, the transition from $|m_7\rangle \rightarrow |m_6\rangle$ occurs, but once in $|m_6\rangle$, only relaxation back to $|m_7\rangle$ is favored. This is in sharp contrast to the situation at high temperature in Figure 3.5d, where reversal through the pathway $|m_7\rangle \rightarrow |m_6\rangle \rightarrow |m_5\rangle \rightarrow |m_{-5}\rangle \rightarrow |m_{-6}\rangle \rightarrow |m_{-7}\rangle$ is now open (red). Note that the reversal through the lower energy pathway $|m_7\rangle \rightarrow |m_8\rangle \rightarrow |m_{-8}\rangle \rightarrow |m_{-7}\rangle$ is still present. However, QTM from $|m_5\rangle \rightarrow |m_{-5}\rangle$ is favored by a factor of about 15 to QTM via $|m_8\rangle \rightarrow |m_{-8}\rangle$. This difference manifests itself in the sharp increase in slope in the high temperature regime of the Arrhenius plot in Figure 3.2, and is in contrast to the situation presented in Figure 3.5a-b for the 4f model, where no change in slope can occur if only a single magnetization pathway is

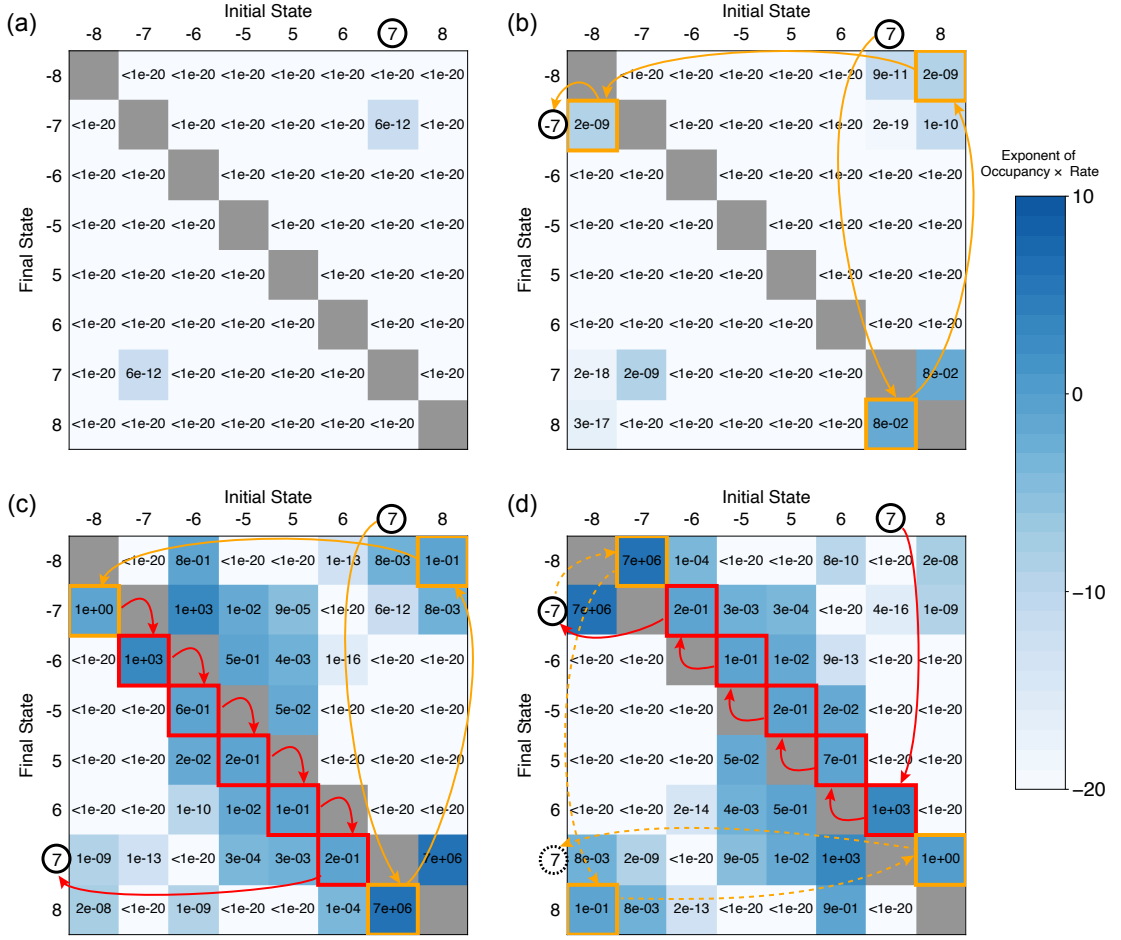


Figure 3.6: **Bias dependent transition rates of the 4f5d6s model.** Similar to Figure 3.5, the product of state occupation and rate (i.e. $\tilde{P}_{M'} W_{MM'}^{el-ph}$) in equilibrium at selected biases of the 0.1 K occupancy trace of Figure 3.3d: (a) -0.5 mV, (b) -4 mV, (c) -12 mV, (d) +12 mV. The value is given if larger than 10^{-20} , and the relative strength is indicated by blue shading. Colored arrows and boxes indicate dominant reversal pathways for the 4f5d6s model (yellow and red). At the tip field used, $B_{tip} = -45$ mT, $|m_7\rangle$ is the ground state.

available.

The reversal mechanisms elucidated thus far describe processes starting from the ground state of $|m_7\rangle$ for the 4f5d6s model and $|7\rangle$ for the 4f model to $|m_{-7}\rangle$ (or $|-7\rangle$). However, looking more closely at the four situations pictured in Figure 3.5 reveals the near symmetry of the rates, such that reversal pathways from $|m_7\rangle \rightarrow |m_{-7}\rangle$ (or $|7\rangle \rightarrow |-7\rangle$) are equivalent to $|m_{-7}\rangle \rightarrow |m_7\rangle$ (or $|-7\rangle \rightarrow |7\rangle$). This is again reflected in the near 50% occupancy calculated in Figure 3.4a, consistent with experimental observations.

In a similar manner, Figure 3.6 reports this same quantity at four different biases of the 0.1 K occupancy plot of Figure 3.3d, calculated with the 4f5d6s model for a fully spin-down polarized

tip ($\rho_T = -1.0$). These conditions allow for a clear determination of the relevant processes influenced by the spin-polarized tip as a function of bias voltage, offering insight into the processes that occur at higher temperature. A spin-down polarized tip implies a HC state corresponds to a preferred state of $|m_{-7}\rangle$. Figure 3.6a contains the transition rates at $V_b = -0.5$ mV. A tip field of $B_{tip} = -45$ mT results in a $|m_7\rangle$ ground state, consistent with an anti-parallel alignment between tip and Dy spin moment and a HC occupancy of 0. At this temperature and bias voltage, no transitions are possible, and the system simply aligns with the field. At $V_b = -4$ mV (Figure 3.6b), the transition $|m_7\rangle \rightarrow |m_8\rangle$ is energetically accessible (yellow), and magnetization reversal through the pathway $|m_8\rangle \rightarrow |m_{-8}\rangle \rightarrow |m_{-7}\rangle$ occurs. At negative bias voltages, corresponding to substrate to tip tunneling, spin decreasing transitions are forbidden due to the fully spin-down polarized tip. Thus, once $|m_{-7}\rangle$ is reached, transitions to other states are hindered and a HC occupancy of 1 is maintained. No additional pathways for magnetization reversal become available until $eV_b \leq -\Delta E_{56} = E(|m_{-5}\rangle) - E(|m_{-6}\rangle) = -11.4$ meV. At $V_b = -12$ mV (Figure 3.6c), this higher energy pathway is accessible (red) and the spin increasing transitions result in a magnetization reversal via $|m_{-7}\rangle \rightarrow |m_{-6}\rangle \rightarrow |m_{-5}\rangle \rightarrow |m_5\rangle \rightarrow |m_6\rangle \rightarrow |m_7\rangle$. Since the lower energy pathway is still accessible, and allowed by the spin-increasing transitions, the Dy spin reverses cyclically through the lower and higher energy pathways. QTM from $|m_{-5}\rangle \rightarrow |m_5\rangle$ is favored by a factor of about 2 to QTM via $|m_8\rangle \rightarrow |m_{-8}\rangle$, thus $|m_7\rangle$ is the preferred state, corresponding to a HC occupancy of 0. The situation is reversed at $V_b = 12$ mV (Figure 3.6d), where tip to substrate tunneling for a fully spin-down polarized tip only allows spin-decreasing transitions. The cycle in Figure 3.6c is flipped, such that reversals occur via $|m_7\rangle \rightarrow |m_6\rangle \rightarrow |m_5\rangle \rightarrow |m_{-5}\rangle \rightarrow |m_{-6}\rangle \rightarrow |m_{-7}\rangle \rightarrow |m_{-8}\rangle \rightarrow |m_8\rangle \rightarrow |m_7\rangle$. Again, QTM from $|m_5\rangle \rightarrow |m_{-5}\rangle$ is favored by a factor of about 2 to QTM via $|m_{-8}\rangle \rightarrow |m_8\rangle$, but in this case $|m_{-7}\rangle$ is the preferred state, corresponding to a HC occupancy of 1.

At higher temperatures and lower tip polarizations, the same processes determine the trend in occupancy; albeit, thermal smearing activates each reversal pathway at lower tunnel biases and there is a greater competition between dominant and non-dominant spin processes due to the unpolarized surface and not fully polarized tip. These processes generally push the occupancy toward 50%-50%.

3.5 Hyperfine considerations

In our SP-STM measurements, the spin-contrast and the spin dynamics of all adsorbed Dy adatoms are identical within our experimental error bars. However, half of the isotopes of Dy (44% natural abundance) have nuclear spin $I = 5/2$ while the remaining isotopes (56% natural abundance) have nuclear spin $I = 0$. To confirm the observed indistinguishability, Figure 3.7 compares the 4f5d6s model with (blue) and without (red) nuclear spin under the same fitting parameters. Note that the model results in Figures 3.2 and 3.3 are identical to the nuclear spin $I = 0$ case presented here. The observed trends in occupancy (Figure 3.7b and d) are nearly indistinguishable, while the 4f5d6s model with nuclear spin exhibits slightly longer lifetimes (Figure 3.7a and c). In all regimes but high temperature, a modest decrease in tip field B_{tip} by

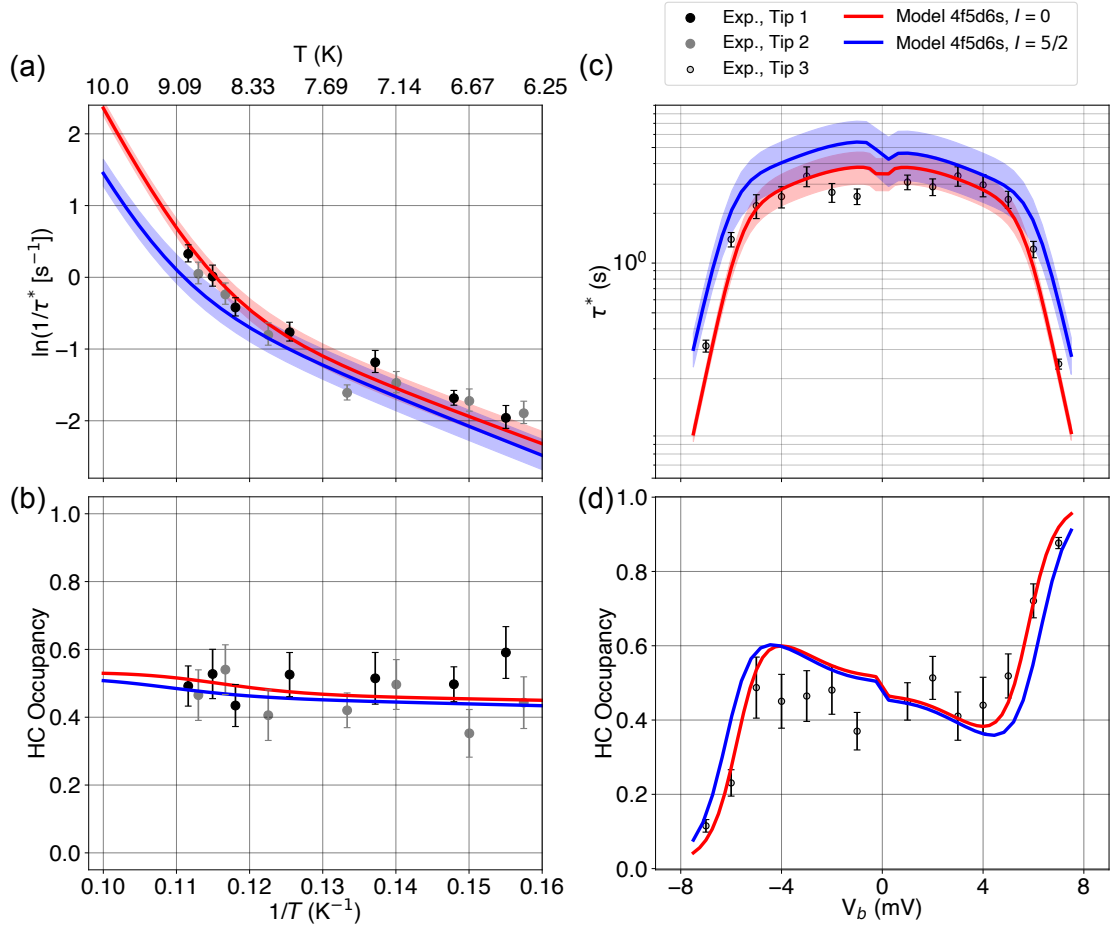


Figure 3.7: **Comparing the 4f5d6s model with and without nuclear spin I .** (a), Arrhenius plot of the spin reversal rate (black and grey dots, $V_b = 1$ mV, set current $I_t = 10$ pA, in the LC state) and corresponding occupancy (b) with fits using the 4f5d6s model with nuclear spin (blue) and without (red) (tip polarization $\rho_T = -0.8$, $B_{tip} = -60$ mT in both cases). (c), Spin lifetimes, (d) occupancy as a function of bias V_b (grey dots with black edges and bars, $T = 6.7$ K, set current $I_t = 10$ pA in the LC state). 4f5d6s model with nuclear spin (blue) and without (red), using $B_{tip} = -45$ mT, $\rho_T = -0.8$. The shaded area shows the accuracy of the fit with variations of tip magnetic field within ± 5 mT. Error bars correspond to 95 % confidence intervals calculated using the normal approximation interval.

5-10 mT is enough to compensate the observed difference. At higher temperatures, the slightly more gradual decrease in lifetimes occurs due to the presence of additional avoided level crossings between $|m_6\rangle$ and $|m_{-6}\rangle$ at zero field. This results in an additional reversal pathway with a lower effective barrier compared to the pathway between $|m_5\rangle$ and $|m_{-5}\rangle$, and therefore more gradual slope. The addition of a hyperfine interaction term of the form of Equation 2.40 in the Hamiltonian (Equation 3.4) changes the basis once again. The basis $|m_i\rangle = |J_z^{4f}, S_z^{5d}, S_z^{6s}\rangle$ becomes $|J_z^{4f}, S_z^{5d}, S_z^{6s}, I_z\rangle$, where I_z can take on values $-5/2, -3/2, -1/2, +1/2, +3/2$, and $+5/2$. The crystal field now mixes the states with $\Delta M_{tot} = \Delta J_z^{4f} + \Delta S_z^{5d} + \Delta S_z^{6s} + \Delta I_z = 6n$, $n \in \mathbb{N}$. For each state $|J_z^{4f}, S_z^{5d}, S_z^{6s}\rangle$ and $|J_z^{4f}, -S_z^{5d}, -S_z^{6s}\rangle$, 36 level crossings exist at zero field.

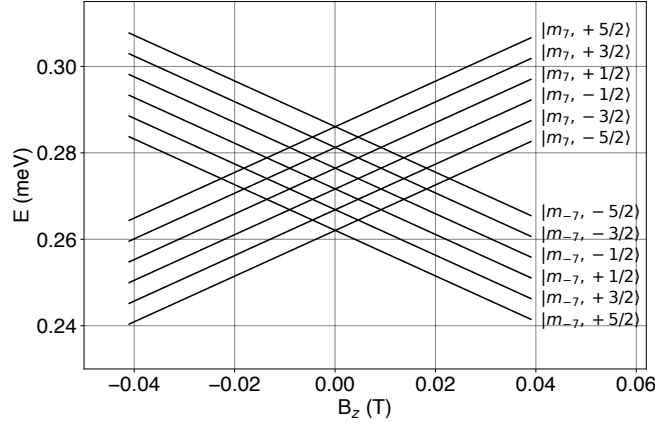


Figure 3.8: **Extended Zeeman diagram of the $|m_{\pm 7}\rangle$ states at zero field.** The hyperfine interaction splits the $|m_7\rangle$ state into 6 states, each with a unique nuclear spin I_z , better represented in the new basis $|m_7, I_z\rangle$. These intersect with the 6 opposing states $|m_{-7}, I_z\rangle$, creating the characteristic diamond shape of 36 level crossings.

To illustrate this, Figure 3.8 displays the level crossings for the $|m_{\pm 7}\rangle$ state, now denoted as $|m_{\pm 7}, I_z\rangle$. The energy spreading of the states $|m_{\pm 7}, I_z\rangle$ is determined by the hyperfine coupling constant; we utilize a value of $0.6 \mu\text{eV}$, consistent with previous studies [158]. As we have seen in the nuclear spin $I = 0$ case, the avoided level crossings dictate the reversal pathways via QTM and therefore the dynamics of the system. It is also (somewhat) trivial to identify the mixed states among only 8. The multiplicity of nuclear spin states slightly increases the complexity of identifying the avoided level crossings. So, to identify and distinguish them from the real crossings, a search algorithm is implemented to first locate each crossing, then minimize the tunnel splitting energy. Each time a crossing occurs, a swap in the order of the states with respect to energy occurs. The algorithm notes the field values where this swap occurs, and the indices of the states that swap. After sweeping through the relevant field range, all the crossing locations in (B_z, E) -space are known. The algorithm then performs a second pass, attempting to minimize the energy difference between each two states. Real level crossings will arbitrarily approach a tunnel splitting of 0, while avoided level crossings will converge onto their non-zero values. A threshold of 10^{-10} meV is set, so that the minimization time is finite. Of course, this implies that any avoided level crossings with tunnel splitting below this value are not considered in the spin dynamics processes.

Figure 3.9 shows the results of this search algorithm. The typical lines representing each state are replaced with points indicating the intersection of two such states. As can be seen in Figure 3.8, the intersections that involve states with equal I_z values lie across the middle of the characteristic diamond shape. Avoided level crossings exist between states $|m_{-5}, I_z\rangle$ and $|m_5, I_z\rangle$ (Figure 3.9a), and $|m_{-8}, I_z\rangle$ and $|m_8, I_z\rangle$ (Figure 3.9d), fulfilling the $\Delta M_{tot} = 6n$, condition with $n = 2$ and $n = 3$ respectively, and $\Delta I_z = 0$. Similar to the $I = 0$ case, the tunnel splitting is larger for the states $|m_{-5}, I_z\rangle$ and $|m_5, I_z\rangle$ than for the states $|m_{-8}, I_z\rangle$ and $|m_8, I_z\rangle$, exhibited by the significant splitting of the upper and lower halves of the diamond. Each

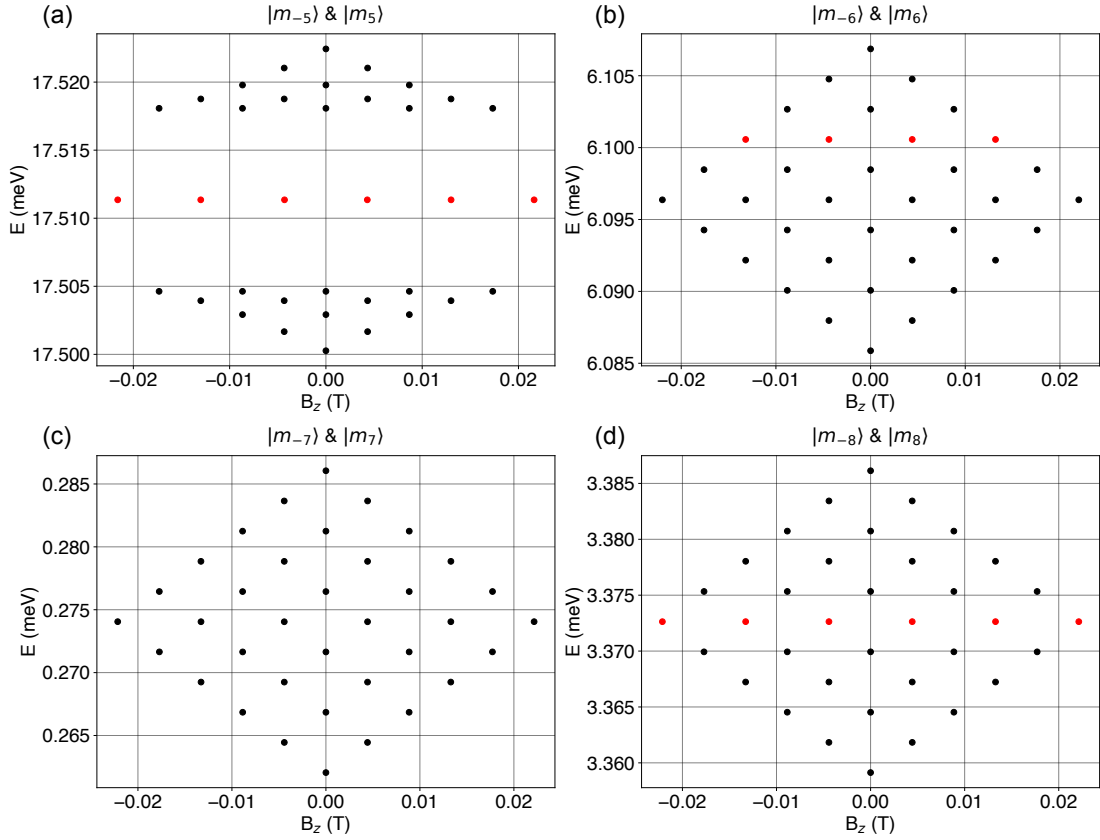


Figure 3.9: **Zero-field level crossings of the 4f5s6s model with nuclear spin I .** Real level crossings (black) and avoided level crossings (red) of the $|m_5\rangle$ and $|m_{-5}\rangle$ states (a), the $|m_6\rangle$ and $|m_{-6}\rangle$ states (b), the $|m_7\rangle$ and $|m_{-7}\rangle$ states (c), and the $|m_8\rangle$ and $|m_{-8}\rangle$ states (d). Crossings are displayed as points located at the center of the crossing, instead of the typical Zeeman diagram lines, for clarity. Note that other crossings do exist, albeit at tunnel splittings below 10^{-10} meV, and are therefore not dominant in the spin dynamics processes.

successive row of intersections, above or below this middle row, correspond to an additional $\Delta I_z = \pm 1$. Thus, the two intersections at the very top and very bottom of the diamond have $\Delta I_z = \pm 5$, and the four intersections second from the top and bottom have $\Delta I_z = \pm 4$, *et cetera*, until the middle row is reached, corresponding to $\Delta I_z = \pm 0$. For the crystal field Hamiltonian \mathcal{H}_{CF} used, the further a crossing is from the middle row, the smaller the tunnel splitting. So, looking back at Figure 3.9b, avoided level crossings exist between states $|m_{-6}, I_z\rangle$ and $|m_6, I_z - 2\rangle$ because $\Delta M_{tot} = 12 + 1 + 1 - 2 = 12$. The states that satisfy this condition (Figure 3.9b in red) are: $|m_{-6}, 5/2\rangle$ and $|m_6, 1/2\rangle$, $|m_{-6}, 3/2\rangle$ and $|m_6, -1/2\rangle$, $|m_{-6}, 1/2\rangle$ and $|m_6, -3/2\rangle$, and $|m_{-6}, -1/2\rangle$ and $|m_6, -5/2\rangle$. These avoided level crossings result in an additional relaxation pathway through the anisotropy barrier, lowering the effective barrier in the high temperature regime of the Arrhenius plot (Figure 3.7a for the $I = 5/2$ case).

Of course, the new basis results in a larger rate matrix in the master equation. The rate tables describing the $I = 0$ case form a modest 8×8 matrix (pictured in Figures 3.5 and 3.6).

The inclusion of the hyperfine interaction produces a larger 48×48 rate matrix. The rates in Equations 2.50 and 2.48 remain the same, as they act only on the external $5d6s$ shells and the $4f$ respectively. On the other hand, the QTM rates of Equation 2.54 are different, as they are dependent on the mixing introduced by the crystal field terms and the choice of basis. Equation 2.54 requires knowledge of the avoided level crossing locations in (B_z, E) -space, as well as the tunnel splitting. Hence, the implementation of the aforementioned algorithm is required to model the lifetimes and occupancies in Figure 3.7.

3.6 Magnetization curves

The magnetic properties of Dy adatoms on graphene/Ir(111) were first assessed by ensemble XMCD measurements [48, 50]. This technique provides direct access to the empty states of the $4f$ shell, by using photons tuned to an energy corresponding to the $M_{4,5}$ absorption edge. The photons excite occupied $3d$ electrons to the unoccupied $4f$ states. The allowed electron transitions are spin-dependent, thus, by probing first with left polarized photons, then with right polarized photons, any difference in absorption spectra will be due to differences in spin populations within the $4f$ shell. Through sum rules, this gives direct access to the magnetic moment of the shell, and tracking this difference as a function of magnetic field allows for magnetization hysteresis measurements. A much more thorough description of the experimental technique and its theoretical background can be found in Refs. [159–164].

Figure 3.10 displays the Zeeman diagram (a) for the $4f5d6s$ model and an XMCD out-of-plane magnetization curve (b) of Dy adatoms on graphene/Ir(111) at 2.5 K [48, 50]. A clear hysteresis is visible, with approximately 30 % of the adatoms retaining their magnetization at zero field. The curve is identical for randomly distributed Dy adatoms and for Dy adatoms arranged in a superlattice, suggesting mutual magnetic interactions are negligible and that the magnetic properties are independent of the adsorption site within the graphene moiré [48]. In the context of single-atom magnets, steps in the hysteresis indicate the presence of a rapid relaxation mechanism (*i.e.*, QTM), and therefore imply the presence of avoided level crossings at the corresponding field values. Figure 3.10b shows two such steps, one at ± 2.7 T and another at ± 5.7 T (indicated with purple arrows). These field values, and their corresponding energies, place constraints on the level diagram of magnetic states. Since the level diagram is determined by the crystal field terms of the spin Hamiltonian, the strength of the crystal field parameters B_n^m in Equation 2.39 can be determined with the help of the magnetization curve. The axial terms (B_2^0 , B_4^0 , B_6^0) determine the shape of the anisotropy barrier and energy difference between the magnetic states. The transverse term (B_6^6) mixes the magnetic states and results in avoided level crossings. Hence, the parameters are tuned to match the indications of avoided level crossings at ± 2.7 T and ± 5.7 T. Note that the level crossings involving the $|m_{\pm 5}\rangle$ states are not accessible with the fields available in our XMCD endstation [164], so their energy cannot be refined with the same precision as for the states with larger out-of-plane projections discussed above.

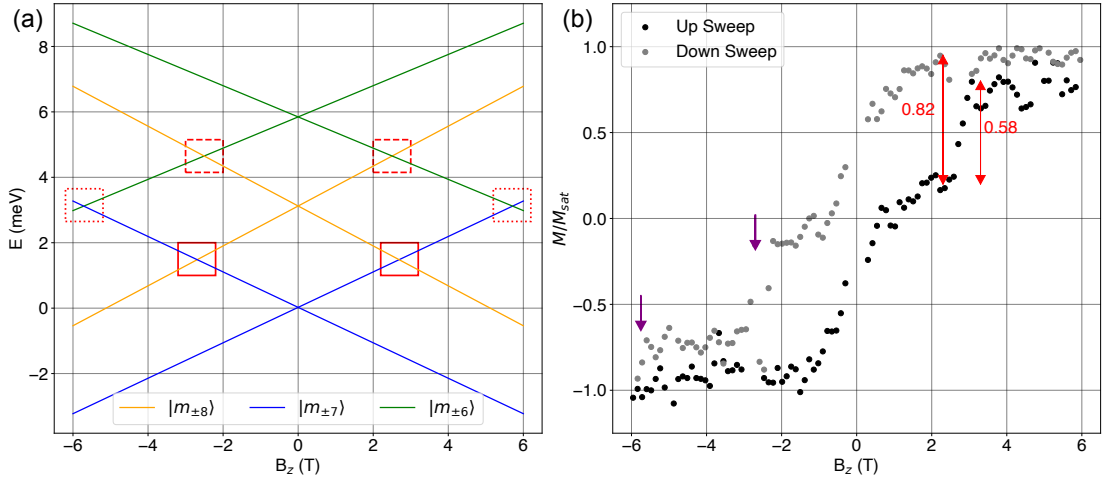


Figure 3.10: **Zeeman diagram of the 4f5d6s model and XMCD magnetization curve.** (a), Zeeman diagram of the lowest lying magnetic levels of the 4f5d6s model between -6 T and 6 T: states $|m_{\pm 7}\rangle$ in blue, states $|m_{\pm 8}\rangle$ in yellow, and states $|m_{\pm 6}\rangle$ in green. The red rectangles mark the non-zero-field level crossings between these states that may be relevant in the magnetization dynamics present in (b). For the nuclear spin $I = 5/2$ case, these rectangles mark the level crossings depicted in Figure 3.11. (b), XMCD magnetization curve of Dy on graphene/Ir(111) ($\phi = 3 \times 10^{-3}$ photons $\text{nm}^{-2} \text{s}^{-1}$, $dB/dt = 33 \text{ mT s}^{-1}$, $T = 2.5 \text{ K}$). Purple arrows mark the relevant steps and red arrows indicate spins available before crossing and the proportion that have reversed.

The Zeeman diagram indicates three crossings (red rectangles) for the 4f5d6s model: $|m_{\pm 6}\rangle$ and $|m_{\mp 8}\rangle$ at ∓ 2.5 T (dashed), $|m_{\pm 8}\rangle$ and $|m_{\mp 7}\rangle$ at ∓ 2.7 T (solid), and $|m_{\pm 6}\rangle$ and $|m_{\mp 7}\rangle$ at ∓ 5.7 T (dotted). The crossing between $|m_{\pm 8}\rangle$ and $|m_{\mp 7}\rangle$ is consistent with the bigger step at ± 2.7 T observed in Figure 3.10b, and the crossing between $|m_{\pm 6}\rangle$ and $|m_{\mp 7}\rangle$ is consistent with the smaller step at ± 5.7 T. Furthermore, by examining the amount of spins available before the magnetization step (indicated with the red arrows on the left in Figure 3.10b for the step at ± 2.7 T) and the relative amount of spins that have reversed (height of the step, red arrow on the right), we can obtain an estimate of the probability of magnetization reversal in the region. For the step at ± 5.7 T, a reversal probability of 1 is observed, as the hysteresis loop closes completely, and all of the remaining spins align with the applied field. For the step at ± 2.7 T, the ratio of reversed spins to available spins is $0.58/0.82$, which gives a reversal probability of 0.71. Knowing that the curve in Figure 3.10b is a convolution of both nuclear spin cases, a total reversal probability for the step at ± 2.7 T is given by $(n_{5/2}/n)P_{5/2} + (n_0/n)P_0 = 0.71$, where $(n_{5/2}/n) = 0.44$ and $(n_0/n) = 0.56$, and corresponds to the natural abundance of the Dy isotopes. To determine the individual probabilities P_0 and $P_{5/2}$, and whether the three crossings in Figure 3.10a are real or avoided, each nuclear spin case must be considered separately.

For the $I = 0$ case: $\Delta M_{tot} = 16$ for the crossing between $|m_{\pm 6}\rangle$ and $|m_{\mp 8}\rangle$ and is therefore real, $\Delta M_{tot} = 17$ for the crossing between $|m_{\pm 8}\rangle$ and $|m_{\mp 7}\rangle$ and is therefore real, and $\Delta M_{tot} = 15$

for the crossing between $|m_{\pm 6}\rangle$ and $|m_{\mp 7}\rangle$ and is therefore real, unless a small $B_6^3 = (2/75)B_6^6$ transverse term is included in \mathcal{H}_{CF} . The non-equivalence of the two graphene sublattices has a measured effect in magnetic adatoms [165], and therefore may be relevant here. The term imposes a $\Delta M_{tot} = 3n$, $n \in \mathbb{N}$ mixing condition on the states, thus a $\Delta M_{tot} = 15$ produces an avoided level crossing. As long as the term is small, it is negligible relative to the $B_6^6 \hat{O}_6^6$ term, and does not change the model results close to zero-field presented in Figures 3.2, 3.3, and 3.7. Thus, Dy adatoms with nuclear spin $I = 0$ have a non-zero-field resonance at ± 5.7 T, and contribute to the relaxation step seen in the magnetization curve. Out-of-resonance relaxation mechanisms, dominant between 0 T and 5.7 T, are limited to electron and phonon scattering from the substrate. As already discussed in Section 3.4.3, phonons do not play a significant role under SP-STM conditions at 6 - 10 K, so the same is expected under XMCD conditions at 2.5 K. On the contrary, significant flux-dependent secondary electrons are generated during XMCD measurements that limit the observed lifetimes [48–53].

In the $I = 5/2$ case, we again implement the same search algorithm described in Section 3.5, with the inclusion of a small $B_6^3 \hat{O}_6^3$ term. Figure 3.11 displays the result of the algorithm. For the crossing between $|m_{\pm 6}, I_z\rangle$ and $|m_{\mp 8}, I_z\rangle$ (a and b), avoided level crossings exist for the condition $\Delta M_{tot} = 16 + \Delta I_z = 3n$, so the possible values of ΔI_z are $-1, +2, -4, +5$. For crossings that satisfy the $\Delta I_z = -1$ condition, the mixing is solely from the $B_6^3 \hat{O}_6^3$ term. These are the only the tunnel splittings above the threshold of 10^{-10} meV, following the trend of smaller tunnel splittings further from the middle row of the diamond. 5 pairs of spin states satisfy this condition in each case: $|m_{\pm 6}, \mp 5/2\rangle$ and $|m_{\mp 8}, \mp 3/2\rangle$, $|m_{\pm 6}, \mp 3/2\rangle$ and $|m_{\mp 8}, \mp 1/2\rangle$, $|m_{\pm 6}, \mp 1/2\rangle$ and $|m_{\mp 8}, \pm 1/2\rangle$, $|m_{\pm 6}, \pm 1/2\rangle$ and $|m_{\mp 8}, \pm 3/2\rangle$, and $|m_{\pm 6}, \pm 3/2\rangle$ and $|m_{\mp 8}, \pm 5/2\rangle$. In the XMCD curve, no step exists at ± 2.5 T, which is consistent with a weak $B_6^3 \hat{O}_6^3$ term such that the above crossings play a negligible role. In addition, $|m_{\mp 8}, I_z\rangle$ is not the ground state, so participating in the avoided level crossings is increasingly unlikely at 2.5 K.

For the crossing between $|m_{\pm 7}, I_z\rangle$ and $|m_{\mp 8}, I_z\rangle$ (d and c), avoided level crossings exist for the condition $\Delta M_{tot} = 17 + \Delta I_z = 3n$, so the possible values of ΔI_z are $+1, -2, +4, -5$. For crossings that satisfy the $\Delta I_z = +1$ condition, the mixing is from the larger $B_6^6 \hat{O}_6^6$ term. 5 pairs of spin states satisfy this condition in each case: $|m_{\mp 7}, \mp 5/2\rangle$ and $|m_{\pm 8}, \mp 3/2\rangle$, $|m_{\mp 7}, \mp 3/2\rangle$ and $|m_{\pm 8}, \mp 1/2\rangle$, $|m_{\mp 7}, \mp 1/2\rangle$ and $|m_{\pm 8}, \pm 1/2\rangle$, $|m_{\mp 7}, \pm 1/2\rangle$ and $|m_{\pm 8}, \pm 3/2\rangle$, and $|m_{\mp 7}, \pm 3/2\rangle$ and $|m_{\pm 8}, \pm 5/2\rangle$. The crossings that satisfy the other ΔI_z conditions are below the threshold, either because they are mixed by the weaker $B_6^3 \hat{O}_6^3$ term or are too far from the center row of the diamond. The biggest step in the XMCD curve lies at ± 2.7 T. This is consistent with a large $B_6^6 \hat{O}_6^6$ term. However, if we assume equal thermal population of nuclear spin states, only 5 out of 6 states go through an avoided level crossing. Therefore a maximum reversal probability due to QTM of $P_{5/2} = 5/6 = 0.83$ is possible, if B_6^6 is large enough to guarantee a magnetization reversal through each crossing. For a single crossing, we can use the Landau-Zener model (Equation 2.55) to ensure the tunnel splitting is large enough to do so. The reversal probability is given by: $1 - P_{LZ} = 1 - \exp(-2\pi\Gamma)$. If the tunnel splitting Δ is greater than or equal to 6.5×10^{-9} , then Γ is greater than or equal to 0.5, and the reversal probability $1 - P_{LZ}$ is greater than or equal to 0.95. A B_6^6 value of -7.5×10^{-6} gives tunnel splittings greater than or equal to

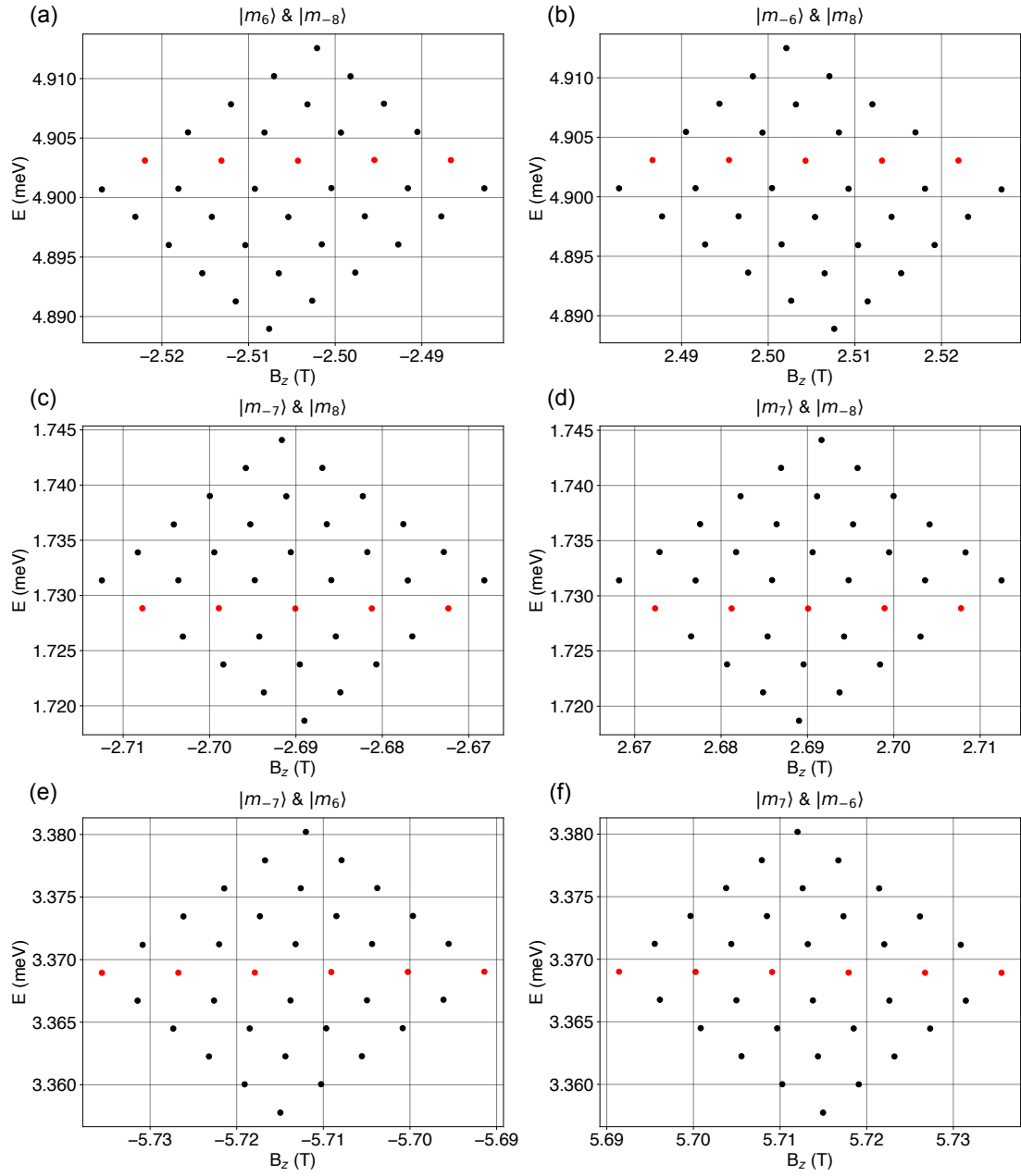


Figure 3.11: **Non-zero-field level crossings of the 4f5s6s model with nuclear spin I .** Level crossings corresponding to the red rectangles of Figure 3.10. Real (black) and avoided (red) crossings of the $|m_6\rangle$ and $|m_{-8}\rangle$ states (a), the $|m_{-6}\rangle$ and $|m_8\rangle$ states (b), the $|m_{-7}\rangle$ and $|m_8\rangle$ states (c), the $|m_7\rangle$ and $|m_{-8}\rangle$ states (d), the $|m_{-7}\rangle$ and $|m_6\rangle$ states (e), and the $|m_7\rangle$ and $|m_{-6}\rangle$ states (f). Crossings are displayed as points located at the center of the crossing, instead of the typical Zeeman diagram lines, for clarity. Note that other crossings do exist, albeit at tunnel splittings below 10^{-10} meV, and are therefore not dominant in the spin dynamics processes.

$\Delta = 6.5 \times 10^{-9}$ for the avoided level crossings between the 5 pairs of spin states listed above, guaranteeing a magnetization reversal through each crossing (*i.e.*, $P_{5/2} = 0.83$). Even with this value, the ensemble reversal probability due to QTM alone $(n_{5/2}/n)P_{5/2} + (n_0/n)P_0 = 0.37$, where $P_0 = 0$ because there is no avoided level crossing at ± 2.7 T in the nuclear spin $I = 0$ case. This is half the observed experimental value of 0.71. Of course, this is without considering the out-of-resonance secondary electron scattering mechanisms.

For the crossing between $|m_{\mp 7}, I_z\rangle$ and $|m_{\pm 6}, I_z\rangle$ (e and f), avoided level crossings exist for the condition $\Delta M_{tot} = 15 + \Delta I_z = 3n$, so the possible values of ΔI_z are 0, -3 , $+3$. For crossings that satisfy the $\Delta I_z = 0$ condition, the mixing is solely from the $B_6^3 \hat{O}_6^3$ term. These are the only tunnel splittings above the threshold. The 6 pairs of spin states that satisfy this condition lie in the center row of the diamond, where I_z is preserved through the crossing: $|m_{\mp 7}, \pm 5/2\rangle$ and $|m_{\pm 6}, \pm 5/2\rangle$, $|m_{\mp 7}, \pm 3/2\rangle$ and $|m_{\pm 6}, \pm 3/2\rangle$, $|m_{\mp 7}, \pm 1/2\rangle$ and $|m_{\pm 6}, \pm 1/2\rangle$, $|m_{\mp 7}, \mp 1/2\rangle$ and $|m_{\pm 6}, \mp 1/2\rangle$, $|m_{\mp 7}, \mp 3/2\rangle$ and $|m_{\pm 6}, \mp 3/2\rangle$, and $|m_{\mp 7}, \mp 5/2\rangle$ and $|m_{\pm 6}, \mp 5/2\rangle$. Every nuclear spin goes through a crossing, and $|m_{\mp 7}, I_z\rangle$ being the ground state ensures the step at ± 5.7 T is significant. Thus both nuclear spin cases participate in the crossing at ± 5.7 T and we expect a significant magnetization reversal probability. Indeed, this is what is experimentally observed.

With all this information in mind, we can adopt the master equation described in Section 3.4.2, and the rates of Equations 2.48, 2.50, and 2.54, to simulate the magnetization loop pictured in Figure 3.10. In the model results presented in Figures 3.2, 3.3, and 3.7, the master equation is solved by initializing the system with 100 % occupation in a single state (*e.g.* $|m_{-7}\rangle$), then letting the system evolve under the phonon, electron and QTM rates (collectively, a rate matrix) as $t \rightarrow \infty$, until the system equilibrates to steady-state occupation values for each magnetic state. How fast the system approaches these equilibrium values is given by τ^* , which is a function of B , and the equilibrium occupations of the $|m_+\rangle$ states and $|m_-\rangle$ states give the occupancy. The difference in occupancy represents the average normalized magnetization. During a magnetization sweep, the system is constantly perturbed by the applied field, preventing the spins from equilibrating. To model this behavior, the system is only allowed to evolve for a time $t_e = \Delta B (dB/dt)^{-1}$ where dB/dt is the experimental sweep rate of 0.033 T/s and ΔB is the step size in field space of the simulation. The total range of simulated field values correspond to the limits of Figure 3.10b (*i.e.*, -6 T to $+6$ T). This is discretized into sufficiently small steps of ΔB , such that within each range the rates do not change significantly. This assumption holds well for out-of-resonance regions of the field sweep. In other words, when there are no avoided level crossings. When there are avoided level crossings, the QTM rates defined by Equation 2.54 change considerably. To capture this behavior, the points corresponding to the exact field values where avoided level crossings occur are included in the sweep simulation from -6 T to $+6$ T. In this case, the evolution time $t_e = \Delta B_{LC} \times (dB/dt)^{-1}$ is calculated using the resonance width of the level crossing $\Delta B_{LC} \approx \Delta/m$ where Δ is the tunnel splitting and m is the magnetic moment of the states involved in the crossing (*i.e.*, slope in Zeeman space). Fortunately, the field values and tunnel splittings are easily found through the search algorithm.

In addition to the phonon scattering rates, the surface-surface scattering rates (e_{SS}) of Equa-

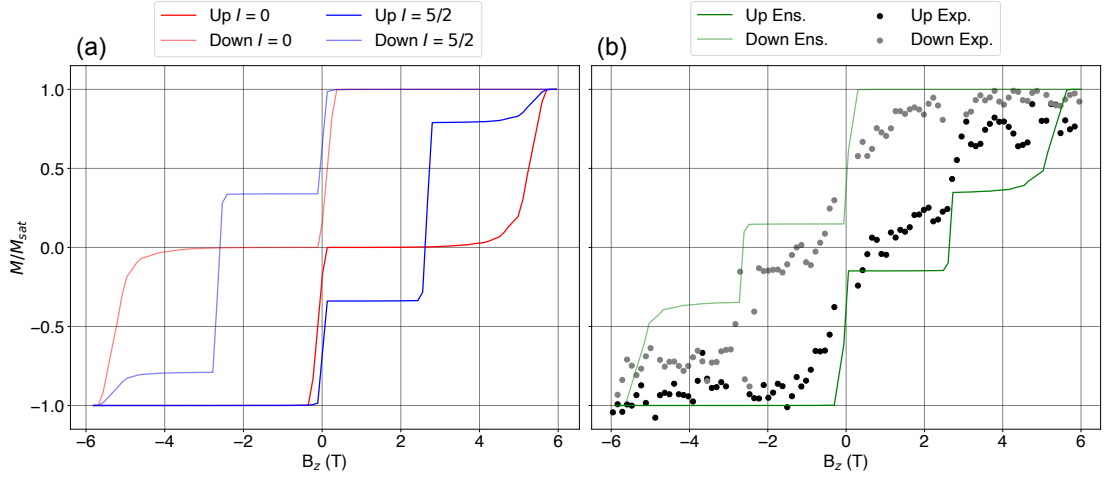


Figure 3.12: **Magnetization curves of the 4f5d6s model for both nuclear spin cases $I = 0$ and $I = 5/2$.** (a), Out-of-equilibrium magnetization sweeps for both nuclear spin cases $I = 0$ (red) and $I = 5/2$ (blue). (b), Ensemble average (green) of the sweeps in (a) to account for the natural abundance of $I = 5/2$ (44%) and $I = 0$ (56%) and the experimental XMCD magnetization curve (black and gray points) depicted in Figure 3.10b ($\phi = 3 \times 10^{-3}$ photons $\text{nm}^{-2} \text{s}^{-1}$, $dB/dt = 33$ mT s^{-1} , $T = 2.5$ K)

tion 2.50 are included in the field sweep simulation, and are given by and ζ_S in Table 3.2, to be consistent with the STM results. Of course, ζ_T is zero, as there is no tunneling current. The other rates are not relevant to XMCD measurements, and are left out. While the implication of secondary electron scattering in lifetime measurements of magnetic systems is well known [48–53], to the best of our knowledge, experimental verification of the energy distribution at the energies relevant here has not been carried out. Extensive experimental studies of the power law dependency of x-ray induced secondary electron energy has been carried out in the 100 eV to 10 keV range, for a variety of standard metals and even insulators [166–171]. However, whether this dependency is accurate in the meV range is unknown. Despite this, and for lack of a more robust model, a power law dependency is implemented to describe the energy distribution of secondary electrons. The scattering rates take the form [166]:

$$W_{MM'}^{se} = \epsilon_{se} \frac{E_{MM'}}{(\phi_{Ir} + E_{MM'})^4} w_{MM'} \quad (3.11)$$

where the matrix elements w are identical to those used for the surface-surface scattering e_{SS} in Equation 2.50 acting on the external shell, ϕ_{Ir} is the work function of Ir, and ϵ_{se} parameterizes the mass photoionization coefficient and the x-ray photon energy. A value of $\epsilon_{se} = 10^6$ best fits the experimental data.

Figure 3.12 shows the result of the magnetization loop simulation. Nuclear spin cases $I = 0$ (red) and $I = 5/2$ (blue) are simulated separately, then the ensemble average (green) is compared with the experimental sweeps. The behavior of each case reflects the level crossing considerations already discussed: the $I = 0$ case has avoided level crossings at 0 and ± 5.7 T, while the $I = 5/2$ case has relevant avoided level crossings at 0, ± 2.7 T, and ± 5.7 T. Also as

expected, the experimentally measured reversal probability at the ± 2.7 T step is larger than the simulated value. This is primarily due to the inability to correctly model the out-of-resonance scattering mechanisms. This inconsistency is also seen in the areas where no avoided level crossings exist (*e.g.*, 0 T to ± 2 T); the relaxation seen in the experimental curve is significantly larger than the simulated curve. Increasing ϵ_{se} better captures the experimental behavior, but also results in a closing of the magnetization loop at 0 T. Despite this, the key characteristics of the experimental curve, such as the energy of the crossings and which are avoided, are reproduced.

3.7 Outlook

This chapter ascertains the necessity of including the intra-atomic exchange to correctly describe spin lifetimes and reading/writing mechanisms in rare-earth adatoms. The intra-atomic exchange between spin-polarized shells defines the total angular momentum and, thus, the QTM channels available for magnetization reversal. The experimental observations cannot be replicated without this consideration. In addition, both nuclear spin cases of Dy are compared, and shown to produce similar behavior in the temperature and bias ranges probed by SP-STM. Determining the avoided level crossings relevant in the spin dynamics for 48 interacting states is not trivial, and we employ an algorithm to locate and determine the tunnel splitting of each. Furthermore, this allows for modeling of XMCD magnetization sweeps, which demonstrate that the crystal field parameters chosen reproduce critical characteristics of the experimental measurements.

In the light of these findings, a revision of previous works should be envisaged for isolated spins, on a surface or in complexes, whenever several electronic shells show spin polarization. This is not restricted to lanthanides, but spans across different species, from 3d elements [172, 173] to actinides [174].

4 The role of the hyperfine interaction in state reversal

In a bout of serendipity, XMCD measurements of an additional system, Ho atoms adsorbed on the oxygen site of MgO films on Ag(100), also exhibited magnetic remanence and a spin lifetime of greater than 10^3 s at 10 K and 10 mT in 2016 [49]. These measurements are consistent with a $J = 8$ total angular moment. Following this discovery, reading and writing of the Ho magnetic state via SP-STM was demonstrated [47] and stability as a function of magnetic field was investigated [42]. These studies observe a coercive field of more than 8 T and magnetic bistability at 35 K, both in agreement with XMCD results. SP-STM measurements of the Zeeman splitting as a function of applied field estimate a magnetic moment of $(9.5 \pm 1.1) \mu_B$ [42]. This is consistent with STM-ESR measurements of the stray field seen by Fe adatoms placed in close proximity to the Ho adatom $(10.1 \pm 0.1) \mu_B$ [47], but much larger than the XMCD estimates of $4.6 \mu_B$ determined by sum rules and multiplet calculations [49]. The STM measurements constrained the magnetic ground state at zero field to either $J_z = \pm 7$ or $J_z = \pm 8$ [42]. Despite this, the zero-field stability of the Ho single atom magnet (SAM) remains an open question. The relaxation times of Ref. [49] were measured down to only 10 mT, and the SP-STM measurements used large magnetic fields ($B \geq 200$ mT) to polarize the paramagnetic tip apex [42, 47]. Here, a SP-STM measurement protocol is implemented to determine the zero-field stability. This permits distinguishability between the proposed ground states, $J_z = \pm 7$ or $J_z = \pm 8$. In addition, we demonstrate controlled magnetic state reversal via Landau-Zener tunneling at avoided level crossings due to the hyperfine interaction.

Work contribution. *A majority of the results presented in this chapter are published in Forrester et al. [175]. Measurements were taken by Dr. Fernandez, Dr. Patthey, and myself. Analysis was done by Dr. Fernandez, Mr. Forrester, Dr. Natterer, and myself. Modeling was done by Mr. Forrester and Dr. Natterer. The linear sweep routine was developed by Mr. Forrester and the experimental design was conceived by Dr. Natterer. All authors were involved in writing and discussion.*

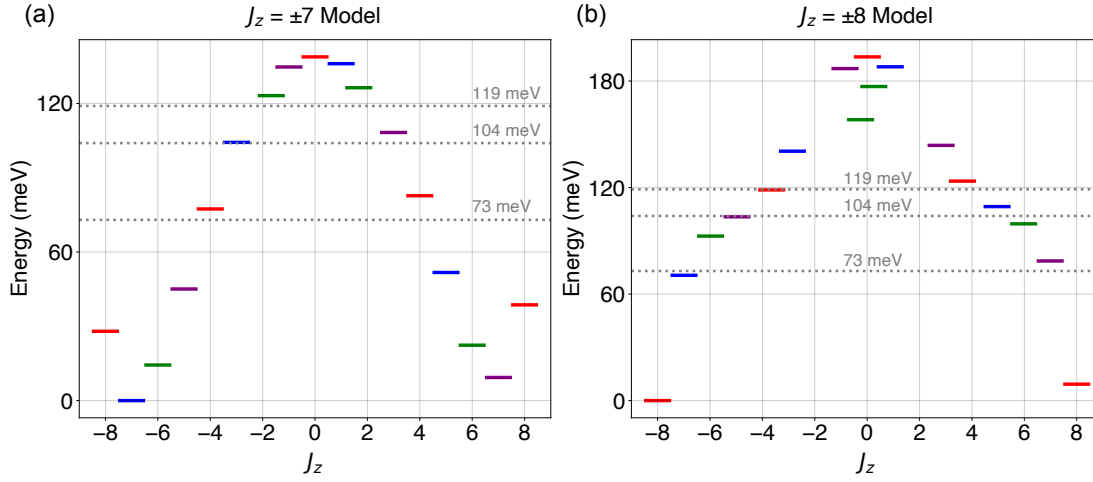


Figure 4.1: **Level diagram comparison for the $J_z = \pm 7$ and $J_z = \pm 8$ models.** Level diagrams for the two models proposed in Ref. [42]. In (a), the ground state corresponds to the $J_z = \pm 7$ state, while in (b), the ground state corresponds to the $J_z = \pm 8$ state. Both level diagrams are calculated at 8 T for consistency with Ref. [42]. The dashed lines display the three tunnel bias thresholds experimentally observed. Same-color states indicate mixing due to transverse crystal field terms.

4.1 Reading the magnetic state

Ho SAMs exhibit a two-state TS above a minimum threshold voltage of $V_t = 73$ mV during constant-height current or constant-current ΔZ traces with SP-STM, in an applied out-of-plane magnetic field of 8 T up to temperatures of 45 K [42]. A magnetic contrast I_{MR}/I_0 of several percent is observed [42, 47, 100]. Above the bias threshold, the atom switches between its two magnetic orientations, denoted high conductance (HC) and low conductance (LC). Below this threshold, remarkable stability is exhibited. Whether this stability is due to the non-zero field present during previous measurements is unresolved. Figure 4.1 displays two level diagrams proposed in Ref. [42] at 8 T. Both level diagrams are consistent with previous STM measurements of the Ho moment [47, 49], and measurements of lifetime as a function of tunnel bias V_b [42]. The lifetime measurements indicated three voltage thresholds where deviations from a linear increase of the switching rate with bias occur: 73 meV, 104 meV, and 119 meV (dotted grey in Figure 4.1). These observed thresholds indicate the presence of additional reversal pathways (*i.e.*, avoided level crossings). In Figure 4.1a, $J_z = \pm 7$ is the ground state. It is protected from direct QTM at zero-field, as the four-fold symmetry of the oxygen adsorption site mixes states separated by $\Delta m = \pm 4$ [176]. In this case, the bias threshold at 73 mV corresponds to QTM via the $J_z = \pm 4$ state. On the other hand, $J_z = \pm 8$ is the ground state for the model in Figure 4.1b. The crystal field mixes the ground doublet, and the observed stability only occurs as a result of the non-zero field values, where the Zeeman energy overcomes the transverse term in the crystal field. The bias threshold at 73 mV corresponds to the $J_z = \pm 7$ state. QTM cannot directly occur between $J_z = \pm 7$, as they are not mixed, however further spin

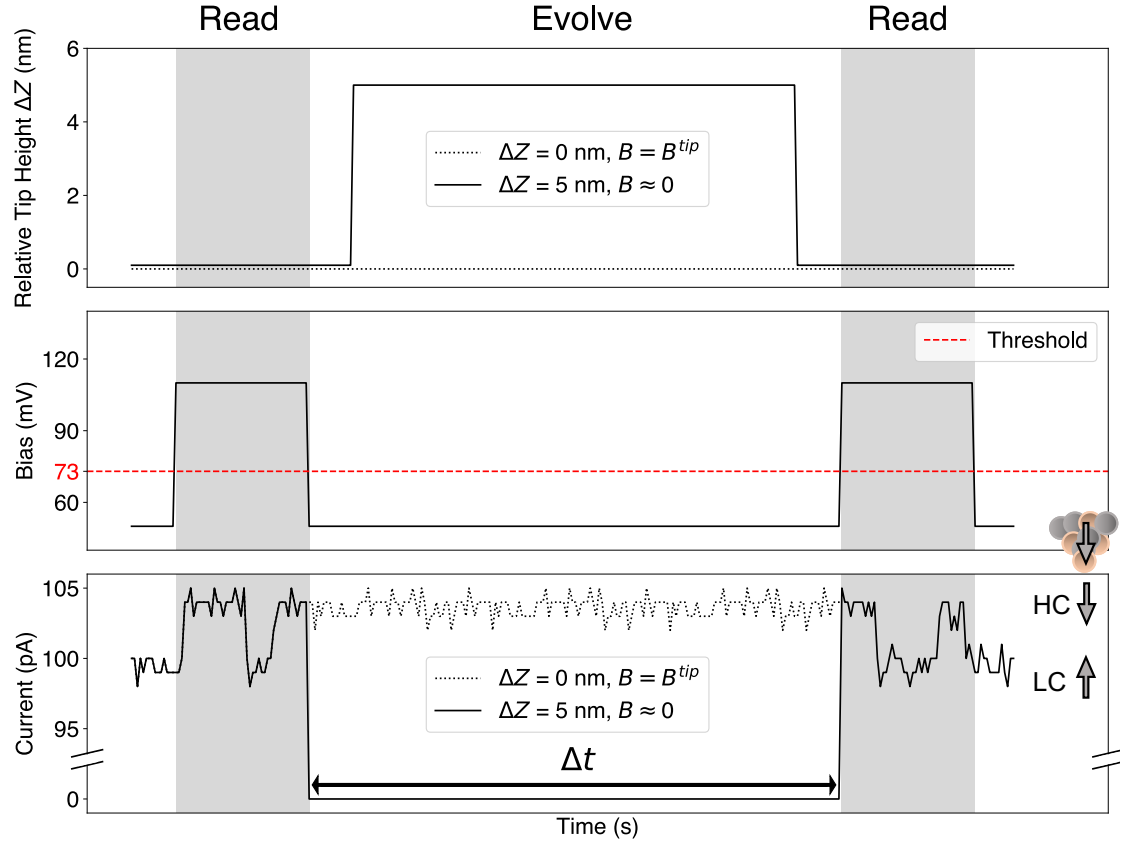


Figure 4.2: **Three phases of the read measurement protocol.** In the first phase (left), the tunnel bias is above the threshold bias (indicated in red, $V_b > V_t$), and the Ho is free to switch between high conductance (HC) and low conductance (LC) states as the SP-STM tip maintains its position above the adatom, reading the state. In the second phase (middle), the tunnel bias is reduced to below the threshold ($V_b < V_t$), and the Ho adatom is allowed to evolve for some time Δt . In the first situation (dotted lines), the relative tip position is maintained $\Delta Z = 0$, and any switches are directly observable through the monitoring of the current (bottom). In this case, the Ho adatom is subject to a tip stray field B^{tip} . In the second situation (solid), the tip is retracted $\Delta Z = 5$ nm, reducing the tip stray field to approximately zero. In the third phase (right), with the tip positioned back near the adatom ($\Delta Z = 0$), the tunnel bias is increased above the threshold bias ($V_b > V_t$), and the state is read. The sketch in the lower right indicates the alignment of tip and Ho moments in the HC and LC states of the trace. In the trace shown, the Ho moment is left in the HC state, the tip is retracted for Δt , and found in the HC state once again.

pumping can result in QTM through higher states.

In order to distinguish between these two models, we employ a measurement protocol using SP-STM, illustrated in Figure 4.2. The magnetic state is read from the TS trace at biases $V_b > V_t$ (left and right). This is done to induce switching events, ensuring correct state identification in the presence of drift. We monitor its evolution at $V_b < V_t$ under two possible situations; either

exposing the atom to the tip stray field, B^{tip} (middle, dotted line), or at zero magnetic field by retracting the tip sufficiently far away (middle, solid line). In the first situation, evolve times as long as $\Delta t = 16$ min at $V_b < V_t$ and $B = B^{tip}$ consistently demonstrate state preservation, as the state in the initial read phase matches the state in the final read phase. This stability is notable, as the atom was exposed to smaller fields than in former STM studies [42, 47]. We estimate the stray field strength B^{tip} to be comparable to those measured for similar antiferromagnetic SP-STM tips (≈ 100 mT) [46, 75, 100, 103, 111].

To determine whether or not this stability is influenced by the stray field, we implement the second situation during the evolve phase, where the STM tip is retracted $\Delta Z = 5$ nm such that the tip stray field experienced by the atom is effectively zero. There are four possible outcomes for such a "read, evolve, read" experiment: the Ho atom either retains its initial state (HC stays HC or LC stays LC), switches from HC to LC, or switches from LC to HC. We repeat this protocol 884 times for various hold times Δt from 0 to 60 s, with 5 different tips. The results are displayed in Table 4.1. Most notable is the overwhelming observation of state conservation. The Ho atoms retain their initial state, irrespective of whether they started in the HC ($99^{+1}_{-2}\%$) or LC ($91 \pm 5\%$) state. However, we do observe a statistically significant occurrence of state reversals, which must have a different origin.

We correct for unseen switching events from finite preamplifier bandwidth, assuming a Markovian probability of state reversal and using measured residence times for the Up and Down states. Error bars represent confidence intervals of one standard deviation calculated using the Agresti-Coull method for binomial processes [177]. Further, this zero-field stability is independent of Δt , the time during which the Ho atom is free to evolve. This proves the excellent magnetic bistability of Ho atoms at zero-field.

4.2 A modified read protocol

To determine whether the magnetic field sweeps, carried out by moving the tip from tunneling distances to full retraction, ΔZ , induce the observed state reversals, we modify the experiment

$\begin{smallmatrix} i \\ f \end{smallmatrix}$	HC	LC
HC	$99^{+1}_{-2} \%$	$9^{+5}_{-5} \%$
LC	$1^{+2}_{-1} \%$	$91^{+5}_{-5} \%$

Table 4.1: State preservation for the read protocol with retracted tip averaged over all hold times (Δt). Columns indicate initial state while rows indicate final state. The protocol was implemented 884 times with 5 different tips.

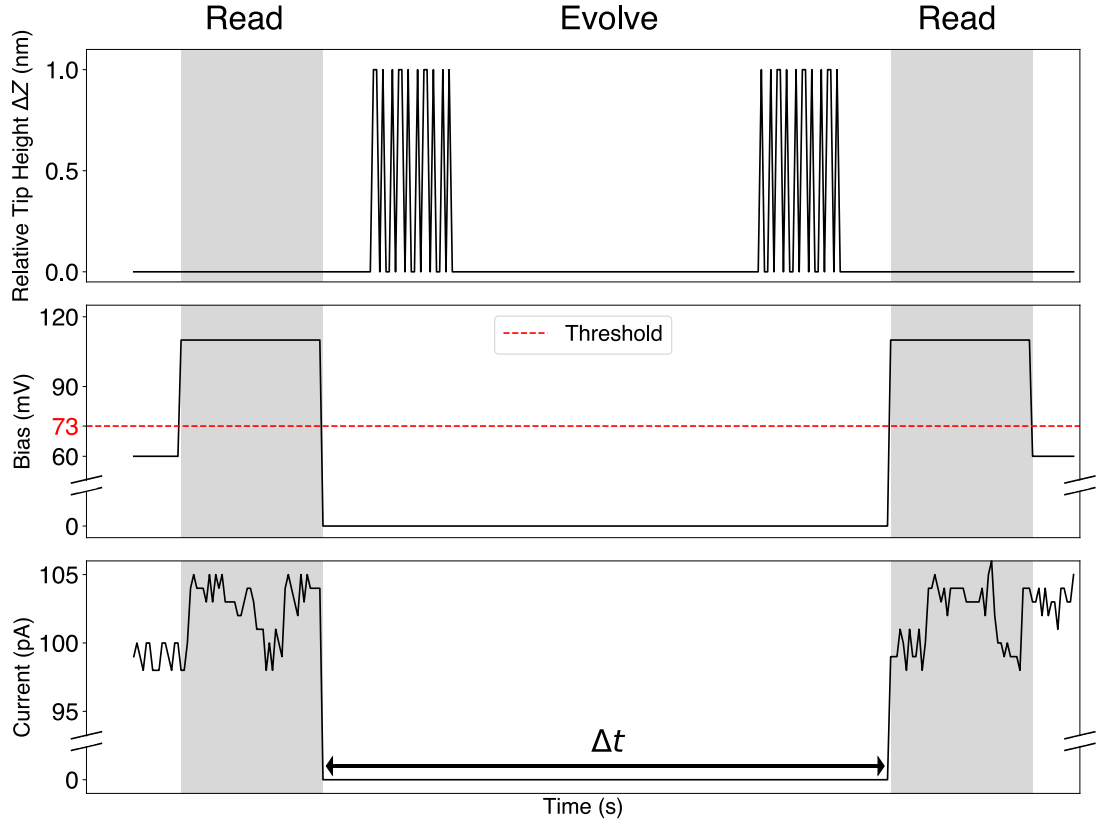


Figure 4.3: **A modified read protocol.** The same protocol pictured in Figure 4.2, except with a modified evolve phase. Instead of retracting the tip once, the tip progresses through N retract/approach cycles with the tunnel bias below the threshold bias ($V_b < V_t$).

sketched in Figure 4.2. This time, we repeatedly retract and approach the tip in the "evolve" phase before reading the state (pictured in Figure 4.3 upper, $V_b < V_t$), instead of merely holding the tip far away from the Ho atom. This is equivalent to several magnetic field sweeps from $B = B^{tip}$ to $B = 0$ T and back, since the tip exposes the Ho atom to some finite stray field, B^{tip} , at tunneling conditions. The occurrence of switches versus the number, N , of tip sweep cycles is displayed in Table 4.2. A single retract/approach cycle ($N = 1$) results in the same negligible occurrence of state reversals: 0_{-0}^{+3} % (starting HC) and 3_{-3}^{+6} % (starting LC). However, when we increase the number of retract/approach cycles in the "evolve" phase ($N = 20$), we see the occurrence of magnetic state reversals grows to 2_{-1}^{+1} % starting HC and 30_{-3}^{+3} % starting LC. For even more retract/approach cycles ($N = 100$), we observe a similar occurrence: 3_{-1}^{+2} % (starting HC) and 28_{-4}^{+5} % (starting LC). Magnetic state reversals starting from the LC state are clearly caused by magnetic field sweeps.

Thus far, we have neglected the hyperfine interaction. To determine whether this is the possible origin of the observed behavior, we add a hyperfine term in the spin Hamiltonian.

Initial State	$N = 1$	$N = 20$	$N = 100$
HC	$0_{-0}^{+3} \%$	$2_{-1}^{+1} \%$	$3_{-2}^{+2} \%$
LC	$3_{-3}^{+6} \%$	$30_{-3}^{+3} \%$	$28_{-4}^{+5} \%$

Table 4.2: State preservation for the modified protocol with N tip retractions.

4.3 Modeling the spin system

To model the system with the hyperfine interaction, we use a Hamiltonian of the following form:

$$\mathcal{H} = \mathcal{H}_{CF} + \mathcal{H}_Z + \mathcal{H}_{hf} \quad (4.1)$$

The effects of the crystal field are described by the first term of the form of Equation 2.39. Due to the fourfold symmetry of the oxygen adsorption site [176], \mathcal{H}_{CF} can be expressed as the sum of the Stevens operators \hat{O}_m^n [112]:

$$\mathcal{H}_{CF} = B_2^0 \hat{O}_2^0 + B_4^0 \hat{O}_4^0 + B_4^4 \hat{O}_4^4 + B_6^0 \hat{O}_6^0 + B_6^4 \hat{O}_6^4 \quad (4.2)$$

where the axial terms ($B_2^0 \hat{O}_2^0$, $B_4^0 \hat{O}_4^0$, and $B_6^0 \hat{O}_6^0$) determine the total zero-field splitting of the magnetic states and the transverse terms ($B_4^4 \hat{O}_4^4$ and $B_6^4 \hat{O}_6^4$) impose a mixing condition $\Delta M_{tot} = 4n$, $n \in \mathbb{N}$ and determine the tunnel splitting Δ of mixed states. As discussed, two sets of crystal field parameters were proposed to explain the three bias thresholds observed in SP-STM [42], but remain consistent with STM-derived magnetic moments [47, 154]. These produce the level diagrams pictured in Figure 4.1, the first consisting of a $J_z = \pm 7$ ground state, and the second a $J_z = \pm 8$ ground state. The values used for each model are taken from Ref. [42]:

Model	B_2^0 (μeV)	B_4^0 (neV)	B_4^4 (neV)	B_6^0 (neV)	B_6^4 (neV)
$J_z = \pm 7$	-670	1600	250	4	-1.5
$J_z = \pm 8$	-835	-1	3700	8.6	0

Table 4.3: CF Stevens Parameters for the $J_z = \pm 7$ and $J_z = \pm 8$ ground state model.

The second term is the Zeeman term of the form of Equation 2.31, to capture the stray magnetic field from the STM tip acting on the $4f$ shell of the Ho adatom. Despite the unknown orientation of the field, an in-plane component only further mixes the J_z states, but this amount is negligible for the field strengths considered, relative to the transverse terms in \mathcal{H}_{CF} . Thus, only the out-of-plane component B_z^{tip} is considered. For brevity, hereafter B^{tip} is used

in place of B_z^{tip} . A different g -factor is used for each model, to ensure a magnetic moment consistent with STM-ESR measurements of $(10.1 \pm 0.1) \mu_B$ [47]. For the $J_z = \pm 7$ ground state model, an effective g -factor of 1.44 is needed, while for the $J_z = \pm 8$ ground state model, a standard value of 1.25 is sufficient. The former requires an additional polarization in the valence shells [42].

The third term of the form of Equation 2.40 captures the hyperfine coupling between the atomic and nuclear moments. Ho has a nuclear spin of $I = 7/2$ (100 % natural abundance), splitting each electron J_z state into $(2I+1) = 8$ non-degenerate states. We use a hyperfine coupling constant of $3.7 \mu\text{eV}$, consistent with previous studies [178–180]. To illustrate the effect this coupling has on the ground states of the level diagrams pictured in Figure 4.1, Figures 4.4a and b show the extended Zeeman diagram for these states, and the resulting 64 level crossings in each case. We use the same search algorithm described in Section 3.5 to determine the avoided and real level crossings.

For the $J_z = \pm 8$ model, the hyperfine interaction leads to 8 non-negligible avoided level crossings at non-zero magnetic fields (red rectangles in Figure 4.4a). These crossings satisfy the mixing condition $\Delta M_{tot} = 4n$, for $n = 4$, as they occur between states $|+8, I_z\rangle$ and $|-8, I_z\rangle$ ($\Delta M_{tot} = 16$). They exhibit a tunnel splitting of $\Delta = 0.19 \mu\text{eV}$. This can be seen in Figure 4.4c, which displays the right-most avoided level crossing demarcated by the red rectangles in Figure 4.4a (around 180 mT). Out of the 64 crossings, other avoided level crossings exist for the condition $\Delta M_{tot} = 16 + \Delta I_z = 4n$, $n \in \mathbb{N}$, but their tunnel splittings fall below the threshold of 10^{-10} meV , and are therefore neglected. Figure 4.4e displays the lowest energy zero-field crossing marked by the purple rectangle in Figure 4.4a. Without the hyperfine interaction, we find the expected zero-field mixing and an avoided level crossing (dashed red curves), while the hyperfine interaction creates a real crossing and thus zero-field stability (solid black curves). This is the case for all $J_z = \pm 8$ zero-field crossings, as they occur between states $|+8, -I_z\rangle$ and $|-8, I_z\rangle$, where ΔI_z can take on only odd values (1,3,5,7), and therefore the mixing condition is never satisfied.

For the $J_z = \pm 7$ model, no avoided level crossings are found above the threshold among the 64 crossings. However, some Ho single ion molecular magnets exhibit $J_z = \pm 7$ electronic ground states in four-fold symmetric crystal fields and host sizeable avoided level crossings but with significantly larger transverse crystal field coefficients (B_4^4 and B_6^4) [181, 182]. We emphasize 6 level crossings that satisfy the mixing condition (orange rectangles in Figure 4.4b). They occur between states with $\Delta M_{tot} = 12$: $|+7, +3/2\rangle$ and $|-7, +7/2\rangle$, $|+7, +1/2\rangle$ and $|-7, +5/2\rangle$, $|+7, -1/2\rangle$ and $|-7, +3/2\rangle$, $|+7, -3/2\rangle$ and $|-7, +1/2\rangle$, $|+7, -5/2\rangle$ and $|-7, -1/2\rangle$, and $|+7, -7/2\rangle$ and $|-7, -3/2\rangle$. The right-most crossing (around 110 mT) is magnified and shown in Figure 4.4d. The zero-field crossings occur between states $|+7, -I_z\rangle$ and $|-7, I_z\rangle$, where ΔI_z can still only take on odd values, and the mixing condition is never satisfied. Thus, the $J_z = \pm 7$ model is stable at zero-field, irregardless of the hyperfine interaction. This can be seen in Figure 4.4f, where the lowest energy crossing (marked by the purple rectangle in Figure 4.4b) between states $|+7, -7/2\rangle$ and $|-7, +7/2\rangle$ is shown. So, in both models, albeit for different

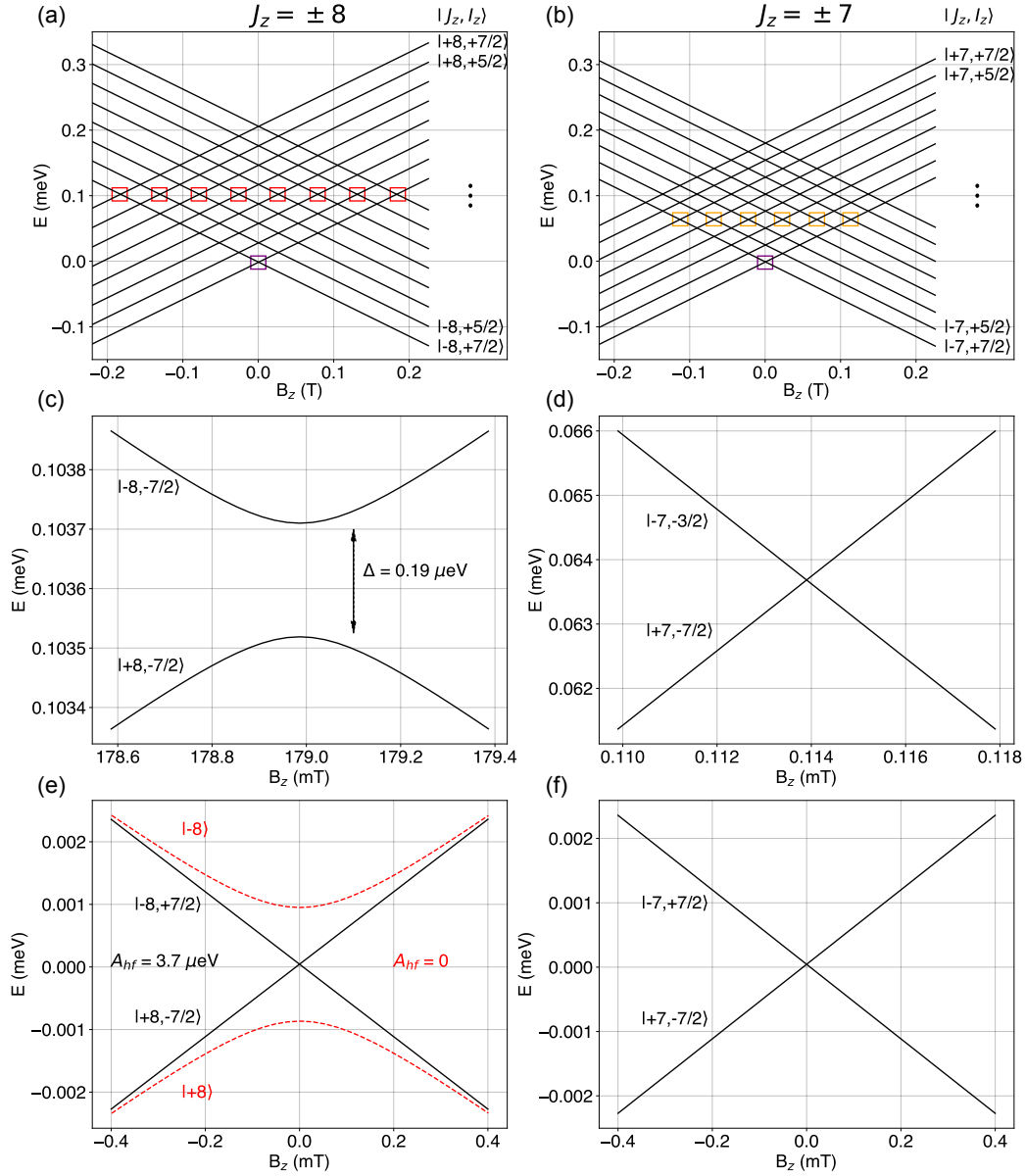


Figure 4.4: **Extended Zeeman diagram for the $J_z = \pm 7$ and $J_z = \pm 8$ models with nuclear spin I .** (a), Extended Zeeman diagram for the $J_z = \pm 8$ electronic ground state highlighting the 8 avoided level crossings (red rectangles) and the lowest energy zero-field crossing (purple rectangle). (b), Same as (a) for $J_z = \pm 7$ model with lowest energy zero-field crossing (purple rectangle) and crossings where the mixing condition $\Delta M_{tot} = 4n$, $n \in \mathbb{N}$ is satisfied (orange rectangles), but no significant tunnel splitting occurs. (c), Right-most avoided level crossing demarcated by the red rectangle around 180 mT in (a) for $J_z = \pm 8$ model. (d), Right-most level crossing demarcated by the orange rectangle around 110 mT in (b) for the $J_z = \pm 7$ model. (e), Lowest energy zero-field crossing corresponding to purple rectangle in (a) with (solid black) and without (dashed red) nuclear spin for $J_z = \pm 8$ model. (f), Real level crossing corresponding to purple rectangle in (b) at zero-field for $J_z = \pm 7$ model.

reasons, none of the zero-field crossings are mixed, implying zero-field stability.

To determine which model is correct, and therefore the ground state, we examine the avoided level crossings at non-zero field values. While the $J_z = \pm 8$ model exhibits 8 such crossings, the $J_z = \pm 7$ model does not host avoided level crossings above the threshold energy of the search algorithm (10^{-10} meV). As discussed in Section 2.2.7, sweeping the magnetic field through an avoided level crossing results in a non-zero probability of magnetic state reversal [139]. Therefore, the increased occurrence of state reversals with an increased number of magnetic field sweeps (tip retract/approach cycles) leads us to conclude that the Ho ground state must be $J_z = \pm 8$.

Note, the magnitude of the hyperfine coupling constant A_{hf} does not influence which crossings are avoided, but only scales the field width of the characteristic diamond of intersecting states in Figure 4.4a and b. Thus, a slightly larger value of A_{hf} only slightly shifts the avoided level crossings to larger values of $|B|$. Our qualitative conclusions therefore remain valid for different values of A_{hf} .

4.4 A write protocol

To demonstrate Landau-Zener tunneling at avoided level crossings [139], we repeat the experiment described in Figure 4.3 with $N = 1$ and different magnetic field sweep rates. In one direction (retract or approach), we use a fast ($dB/dt = 10^5 - 10^7$ T/s) magnetic field sweep rate, and in the other a very slow one ($dB/dt = 10^{-4}$ T/s). The probability of magnetic state reversal is given by $1 - P_{LZ}$, where P_{LZ} is given by Equation 2.55. As can be seen in the definition of Γ in Equation 2.56, the probability of switching approaches 100 % for the slow sweep and is nearly 0 % for the fast one. Performing a fast and slow sweep consecutively (or vice versa) thus results in a net reversal of the spin state. Table 4.4 shows the observed magnetic state reversal for these protocols. Both show state reversal occurrences on the order of 50 % regardless of the initial state, in accordance with the Landau-Zener tunneling process. Note, we expect occurrences near 50 % (instead of 100 %) as a maximum of 4 out of the 8 nuclear spin levels for each manifold host avoided level crossings for the field values used in this experiment ($B = B^{tip} \rightarrow B = 0 \rightarrow B = B^{tip}$, where $B^{tip} \geq 0$). We observe different occurrences of magnetic state reversal depending on the initial Ho state, in agreement with the thermal occupation probability of the states that traverse avoided level crossings for the two spin manifolds (57 % and 43 %, respectively). Accordingly, the efficiency of magnetic state reversal for each initial Ho state reverses when the sweep order is reversed.

Thus, we have demonstrated the zero-field stability of the Ho SAM and the existence of avoided level crossings at certain non-zero field values, allowing us to identify a ground state of $J_z = \pm 8$. We have established a proof of principle experiment that demonstrates our ability to deliberately invert and thus write the magnetic state via QTM at an avoided level crossing.

	Slow–Fast		Fast–Slow	
	Exp.	Theory	Exp.	Theory
HC \rightarrow LC	55^{+15}_{-16} %	57 %	35^{+19}_{-15} %	43 %
LC \rightarrow HC	48^{+17}_{-17} %	43 %	59^{+20}_{-23} %	57 %

Table 4.4: Observed switching probabilities for state inversion through Landau-Zener tunneling. The Write protocol was implemented 110 times with the same tip.

4.5 Reconciling with recent developments

Following the publication of the results presented in Sections 4.1 to 4.4 in 2019, several novel developments justify further consideration of the picture presented in Figure 4.4. The first consists of multiconfigurational *ab initio* calculations and XMCD measurements related to the occupation of the valence shell [152, 183], and the second ascribes a 2-phonon Raman relaxation mechanism thermally activated at low field to the Ho SAM [51]. We first discuss the former.

Without the presence of the Ag(100) substrate, multiconfigurational *ab initio* calculations find the Ho SAM in a $6s^2 6p^0$ ground state configuration, with an additional unpaired electron in an atomic-like $5d_{x^2-y^2}$ orbital [152]. At slightly higher energy, a $6s^2 6p^1$ configuration exists that has a magnetic moment and spin excitations consistent with STM measurements [42, 47]. The authors note that the energy difference between the two configurations is highly sensitive to the treatment of the MgO substrate [152]. The ground state configuration implies a polarized $5d$ shell, and may explain the low magnetic contrast seen in SP-STM measurements. However, this is in contradiction with XMCD measurements at the $M_{2,3}$ edges which indicate a depleted $5d$ shell. The depletion of the shell may be due to the presence of the Ag(100) substrate, whereby a charge transfer from the Ho to the metal occurs [183]. A depleted $5d$ shell is inconsistent with the $J_z = \pm 7$ model, where an additional moment from the valence shell $m_{5d6s} = 1.3 \mu_B$ is required to match the total magnetic moment, lending further confirmation of the $J_z = \pm 8$ model. To reconcile these considerations, a small fractional charge may still be present in the $5d$ shell in the $6s^2 6p^0$ ground state configuration, enough for a slight polarization, and consistent with the magnetic contrast observed. If this is the case, the $5d$ shell needs to be considered in choosing a basis that correctly describes the magnetic quantum states, as we have seen for the Dy SAM.

If a slight polarization is in fact present, albeit below any XMCD measurement threshold due to noise, the avoided level crossings in Figure 4.4a are no longer avoided, but real instead. Similar to the Dy on graphene SAM, a better basis is given by $|J_z^{4f}, J_z^{5d}, I_z\rangle$ instead of the formerly used $|J_z^{4f}, I_z\rangle$. The 8 avoided level crossings at non-zero magnetic fields in Figure 4.4a no longer satisfy the mixing condition $\Delta M_{tot} = 4n$, for $n = 4$. The ΔM_{tot} depends on whether the orbital

moment of the $5d$ shell is quenched or not, quite possibly due to the hybridization with the oxygen atom below. If we assume it is, such that $J_z^{5d} = S_z^{5d} = 1/2$, than an additional $\Delta M = \pm 1$ in ΔM_{tot} is required between the states $|-8, -1/2, I_z\rangle$ and $|+8, +1/2, I_z\rangle$, and $\Delta M_{tot} = 17$. Hence, why they are no longer mixed. However, non-negligible avoided level crossings are still present in Figure 4.4a. Instead of lying in the middle row of crossings, they are shifted up a row in the diamond, which has crossings that satisfy $|-8, -1/2, I_z\rangle$ and $|+8, +1/2, I_z - 1\rangle$ such that $\Delta M_{tot} = \Delta J_z^{4f} + \Delta S_z^{5d} + \Delta I_z = 16 + 1 - 1 = 16$. This implies 7 avoided level crossings, 6 at non-zero field and 1 at zero-field. The results of Section 4.4 remain valid, and the picture of the lowest energy zero-field crossing indicated by the black lines in Figure 4.4e is still the case. The new basis also does not change the situation of the $J_z = \pm 7$ model presented in Figure 4.4b, as no avoided level crossings are found above the threshold of 10^{-10} meV.

The latter development attributes a thermally activated 2-phonon Raman process as the dominant relaxation mechanism for the Ho SAM at low-field values (≤ 0.2 T) and above 10 K [51]. At higher field values, or lower temperatures, this mechanism is suppressed, and spin lifetimes on the order of 10^3 s are observed, only limited by secondary electron scattering. DFT calculations indicate the presence of a local in-plane vibrational mode 4 meV above the ground state [154]. Remarkably, this is consistent with the activation barrier U_{rev} experimentally observed in the lifetime measurements as a function of temperature. Thus, this vibrational mode must dominate the spin-phonon coupling. The fact that it is suppressed at high-field values (*i.e.*, when the two states of the lowest doublet are far apart in energy), and that the observed lifetimes are relatively long, suggest a higher-order process necessitating the simultaneous absorption and/or emission of two phonons via an intermediate state. In the context of the model presented in Ref. [51], this intermediate state is the aforementioned vibrational mode available 4 meV above the ground state. A simplified 2-phonon Raman rate model, consisting of just 3 states (two ground and the vibrational mode), reproduces the experimental trends as a function of magnetic field and temperature reasonably well. However, in the complete picture of the 2-phonon Raman process presented in Ref. [120], the existence of a virtual state $|c\rangle$ is understood to be an admixture of all the magnetic states of the system, resulting from the phonon perturbation itself. In this picture, the sum over all states $|c\rangle$ (Equation 2.45) in the level diagram, or envelope of intermediate excited states, should produce an effective state 4 meV above the ground state, equivalent to the vibrational mode derived from DFT calculations. Of course, the calculation of the envelope of intermediate excited states is dependent on the positions of all the higher energy states in the level diagram, which may be difficult to access experimentally. In light of these considerations, an attempt was made in this thesis to implement the complete Raman rate model (Equation 2.45) using the level diagram of Figure 4.1a. A comparison of the simplified 2-phonon Raman model used in Ref. [51] and the complete 2-phonon Raman model of Equation 2.45 is pictured in Figure 4.5. For the simplified model, the vibrational mode at 4 meV is activated above 10 K (Figure 4.5a), resulting in a reduction of the lifetime τ^* from the photon-limited lifetime due to secondary electron of 1630 s to below 500 s at 22 K. This reproduces the experimental measurement quite well [51]. On the other hand, the complete model does not exhibit any reduction in

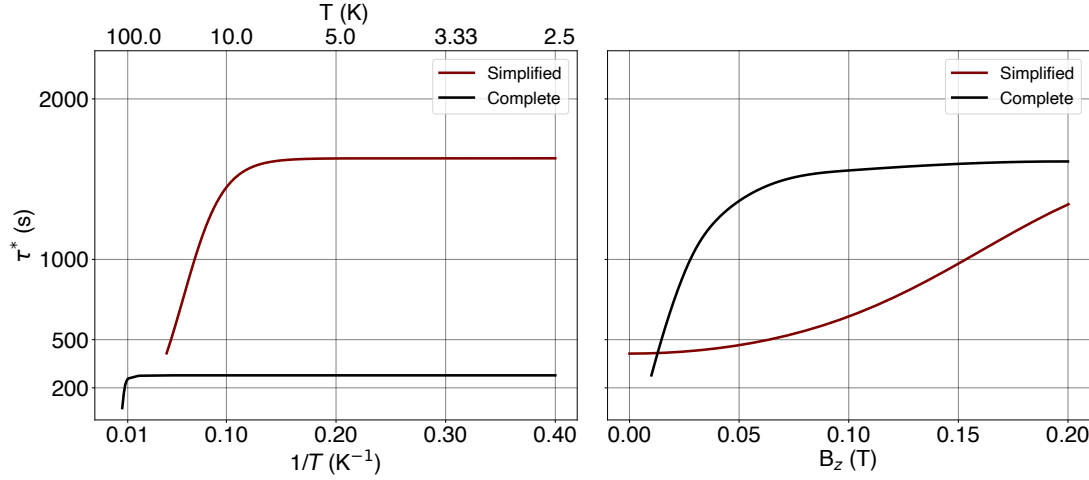


Figure 4.5: **Comparison between simplified and complete 2-phonon Raman models.** (a), Calculated lifetimes at 0.01 T as a function of temperature T for the simplified 2-phonon Raman model from Ref. [51] and for the complete 2-phonon Raman model using Equation 2.45. (b), Calculated lifetimes for both models at 22 K as a function of magnetic field B_z . In the same manner as the Dy SAM, a parameter ν_{ph} is used for the complete model in (a) and (b). The value of $\nu_{ph} = 8 \times 10^{-34}$ is chosen such that the complete model exhibits a lifetime below 500 s at 2.5 K and 0.01 T, similar to experimental observations and the simplified model. In addition, QTM term of the form of Equation 2.54 is added to the complete model. Also note that for the simplified model, the authors of Ref. [51] add a constant photon-limited lifetime due to secondary electron of 1630 s.

lifetime until above 100 K, and the lifetimes at lower temperatures remains considerably lower than the simplified model. Unfortunately, summing over all intermediate states $|c\rangle$ in the $J_z = \pm 8$ model does not produce an effective state that replicates the effect of the in-plane vibrational mode. It is worth noting that the same calculation for the $J_z = \pm 7$ model, using the level diagram in Figure 4.1a instead, also fails to replicate this effect. As a function of magnetic field (Figure 4.5b), the trends displayed by both models are clearly different, with the simplified model exhibiting a more gradual increase in lifetime with an increase in field. At field values above 0.2 T, lifetimes are limited to the secondary electron value of 1630 s. Despite the difference in trends, both models fall reasonably within the error bars of the experimental measurements in the field region pictured [51]. However, the experimental trends above 10 K could not be reproduced by the complete 2-phonon Raman model. This implies that the positions of higher energy states depicted in Figure 4.1b are not correct. This is not surprising, as the SP-STM measurements of Ref. [42], that determined the three tunnel bias thresholds depicted in Figure 4.4, only provide access to the position of 6 states, in principle. Whether crystal field parameters exist that are consistent with all the experimental observations remains an open question: a $J_z = \pm 8$ ground state, an effective state 4 meV above this ground state, and higher energy states consistent with the three tunnel bias thresholds.

In addition to the implementation of the complete 2-phonon Raman model, the effect of a 2-phonon Orbach process (Equation 2.43) was also explored. As discussed in Section 2.2.5,

the primary difference between the 2-phonon Orbach and Raman processes is whether the energy of the two phonons are below (Orbach) or above (Raman) the cutoff energy $k_B T_{Deb}$. MgO has a Debye temperature of about 740 K [184], so $k_B T_{Deb} = 64$ meV, which is below all possible intermediate states in Figure 4.1b. However, this temperature may not be valid for the local Ho-O bond. Regardless, the calculation of Orbach rates (Equation 2.43) also involves a sum over all intermediate states in the level diagram, but fails to reproduce an effective state that replicates the effect of the in-plane vibrational mode and reproduce the trends in Figure 4.5 as a function of temperature.

4.6 Outlook

Our measurement protocols demonstrate the zero-field stability of Ho single atom magnets and the existence of avoided level crossings at certain non-zero field values, allowing us to identify a ground state of $J_z = 8$. We have established a proof of principle experiment that demonstrates our ability to deliberately invert and thus write the magnetic state of a single atom magnet via QTM at an avoided level crossing. Our approach removes the need for high energy tunneling electrons, since the magnetization reversal can be fully induced by a controlled state mixing at an avoided level crossing. The only requirement for large scale implementation is the external control of the applied magnetic field.

In the case of the Ho SAM, reconciling the experimental observations across multiple studies [42, 47, 49, 51, 175, 183], using both local and ensemble techniques, with DFT calculations [51, 152, 183] requires specific knowledge of the higher energy states in the level diagram. Unfortunately, these states are difficult to access, as only states that participate directly in relaxation mechanisms are experimentally visible. For the states that participate indirectly in relaxation mechanisms, such as the 2-phonon Raman and Orbach processes, their location must be inferred from the envelope calculations of Equations 2.43 and 2.45. As we have seen, determining the correct crystal field parameters is not trivial, as many parameter sets exist that are all consistent with the experimental observations. This is evident not only in the two sets presented in Section 4.3, but also in the historical progression of Ho SAM studies listed above.

5 Engineering transition metal heterodimers

The properties of the Ho and Dy SAMs explored in Chapters 3 and 4 inform the search for new systems that exhibit similar characteristics—mainly, long spin lifetimes. For the former SAM, the strong Ho-O bond [49, 51, 152, 176] produces a large anisotropy barrier. This is reflected by the dominant axial terms in the crystal field that result in the first excited state lying 73 meV above the ground doublet. The weaker transverse terms limit state mixing and therefore, magnetization reversal via QTM through the barrier. The hyperfine coupling that occurs between nuclear and magnetic moments ensure zero-field stability, and offers a low-energy mechanism to induce state reversal. In addition, the high stiffness and high bandgap oxide decoupling layers limit scattering with electrons and phonons, further protecting the systems from thermally induced switching. For the latter SAM, the high symmetry of the C_{6v} adsorption site protects the ground state from direct mixing. The graphene decoupling layer prevents any phonon-induced reversals and limits the electron scattering from the Ir(111) substrate below. The large polarization of the valence shells exchange-coupled to the $4f$ shell allows for a large magnetoresistive current and thus, an efficient state reading and writing mechanism via SP-STM. With these properties in mind, this chapter motivates the study of a new system—the IrCo heterodimer adsorbed on graphene. Further, strategies to create and identify the heterodimer are discussed and executed.

Work contribution. *All STM measurements were taken by Dr. Curcella, Dr. Patthey, and myself. Analysis was done by Dr. Curcella and myself.*

5.1 Theoretical motivation

The properties of nanoscale magnetic systems composed of one or a few atoms are primarily calculated either by using semi-empirical quantum chemistry methods or with DFT-based methods. Methods based in quantum chemistry typically require approximations to capture electron correlations and minimize computational intensity. This allows for a direct determination of the multiplet structure, but requires empirical data to validate the approximations made. DFT-based methods also rely on approximations to capture exchange and correla-

tion effects, but the computational costs are much lower. Additionally, the charge and spin densities that are used in the calculation are not orbitally dependent, and therefore preclude determination of the multiplet structure. Regardless, DFT studies are a computationally efficient method of informing experimental investigations of the magnetic properties of adatoms and dimers. Using properties that the method can calculate, such as MAE and adsorption site, they can give insight into the potential for a system to possess long spin lifetimes. However, the validity and accuracy of these predictions are determined by the approximations used, among other considerations. Here, we briefly discuss the properties that DFT can predict, how they can inform our experimental investigations, and other related practicalities, in order to motivate our study of the IrCo heterodimer.

The atomic arrangement of dimers pose an intriguing possibility in the space of stable magnetic systems. Their geometry already lends a promising indicator of stability—dominant axial symmetry about their molecular axis. As was the case with the Ho SAM, dominant axial terms in the crystal field are instrumental to a large MAE. Ample DFT studies have been carried out for novel dimer systems composed of transition metals and/or rare-earths, in the hopes of finding new systems that exhibit long spin lifetimes [185–196]. These are the target of investigation because of their large magnetic moments in the case of $3d$ transition metals, strong spin-orbit coupling in the case of $5d$ transition metals, or both, in the case of $4f$ rare-earth metals. Generally, large magnetic moments and strong spin-orbit coupling are essential for a large MAEs. For practical applications, these dimers must be adsorbed on a surface, where their magnetic properties can change due to the surrounding crystal field, as discussed in Section 2.2.3. Regular DFT cannot directly obtain the strength of the crystal field, and therefore the total zero-field splitting of the magnetic states. Alternatively, the MAE can be determined by calculating the total energy difference between different orientations of the magnetic moment. In general, a large MAE implies a large total zero-field splitting. In the absence of state mixing and QTM, the larger the MAE, the more the system is protected against thermally-induced magnetization reversals. Thus, a large MAE is a necessity for stability.

In addition to the MAE, the symmetry of the adsorption site should also be considered. As exemplified by the Ho and Dy SAMs, the symmetry and strength of the crystal field determine the mixing of the magnetic states, which govern the available magnetization reversal pathways. While DFT cannot directly provide the strength of the transverse terms, the adsorption site can be determined by evaluating the total energy of each of the possible adsorption sites on a given surface. A similar procedure can be used to determine the adsorption geometry of the dimer. The resulting lowest-energy site and geometry informs the terms that should be included in crystal field Hamiltonian, and a general idea of the state mixing present in the system.

Furthermore, the choice of decoupling layer and substrate is critical in minimizing electron and phonon scattering. In the context of DFT, the dimer is adsorbed onto only one or a few atomic, free-standing layers, if any at all. The more layers are included, the more computationally intensive the calculation is. A majority of the studies consider a single graphene layer [186,

188, 190, 191, 193, 195], while others include just a benzene ring [187–189], or a monolayer of hexagonal boron nitride (*h*-BN) [192]. The gaseous-state calculations of MAE [185, 190, 194] are functionally useless to the surface scientist, or any feasible application requiring electrodes, although comparisons with the layer-included results are informative of the effects of the substrate layer(s), as pointed out in Refs. [190, 191]. While a single layer is more informative than none at all, practical applications require surface-supported decoupling layers. Hence, studies that include both the decoupling layer and a few atomic layers of supporting substrate are more comprehensive and may provide the most realistic predictions.

In choosing a system to experimentally validate, the three aforementioned considerations must be made. In addition, the accuracy of the MAE calculations, determined by the treatment of electron correlations, should also be evaluated. Typically, the magnetic anisotropy is dominated by contributions from the magnetocrystalline anisotropy (MCA) discussed in Section 2.2.3. This is fundamentally determined by the strength of the spin-orbit coupling. To illustrate, Wang *et al.* [197] originally proposed an approximation of the MCA energy E_{MCA} for axial symmetries under a second-order perturbation approach, proportional to the difference of the orbital moment matrix elements in the *z* and *x* directions, summed across the unoccupied (*u*) and occupied (*o*) states [194, 197, 198]:

$$E_{\text{MCA}} \approx \lambda^2 \sum_{u,o} \left[\frac{\langle u | L_z | o \rangle^2}{E_u - E_o} - \frac{\langle u | L_x | o \rangle^2}{E_u - E_o} \right] \quad (5.1)$$

where λ is the spin-orbit coupling strength of Section 2.2.2¹. From Equation 5.1, E_{MCA} is strongly dependent on the coupling and energy splitting of occupied and unoccupied states. Without accurate treatment of electron correlations, these values may not be accurate either. In the context of DFT, there are various approximations and/or corrections to capture correlations, such as introducing a Hubbard *U* energy correction, or modifying the functional form. However, even if an approximation and/or correction produces a prediction in agreement with empirical observations for one system, it is typically not transferable to other systems. Without any empirical validation, the next-best indicator is consistency among calculations using multiple different approximations and/or corrections. Thus, dimer systems where multiple studies calculate similar MAE values, using different methodologies, should carry more weight than those that do not. For a more thorough discussion on the validity of these computational methods applied to these systems, see Refs. [190, 199].

Table 5.1 consolidates the MAE calculations of several studies of transition metal homodimers and heterodimers performed in the gas phase and on various pristine carbon-based adsorption layers. In some cases, ranges are provided to reflect the different electron correlation approximations used in the calculations. Note that we do not include studies that rely on modified substrates, such as oxidized [193] or boron-doped graphene [195] or defective *h*-BN [192], as the practicality of reliably producing these systems poses an additional difficulty.

¹The value of λ is actually slightly modified from the spin-orbit coupling strength in Section 2.2.2. Here, it is the radial integral of the product of the spin-orbit coupling strength and the radial wave functions of state *o* and *u*. See Ref. [197] for more details.

Dimer	Calculated MAE/dimer (meV) in various configurations			
	gas	benzene	graphene	graphene/Cu(111)
Co ₂	7.1 [190] 30 [185]	50-330 (u-h) [187, 189]	-	-
Ir ₂	69.8 [190] 77 [192]	-	non-magnetic (u-h) [190] non-magnetic (u-h) [195]	1.0 (fl-br) [191] 42.4 (u-h) [191]
Pt ₂	46.3 [190]	-	23.2 (u-h) [190, 200] non-magnetic (fl-h) [200]	0.7 (fl-br)[191] 23.1 (u-br)[191]
PtCo	18.8 [190]	-	11.7 (u-h) [190]	7.0 (u-h) [191]
IrFe	-	31.5 (u-h) [195]	-	-
IrCo	69 [190] 142-230 [188]	248-289 (u-h) [188]	93 (u-h) [190] 198-327 (u-h) [188]	204 (u-h) [191]

Table 5.1: Calculated MAEs (meV/dimer) of transition metal dimers in various configurations. An upstanding configuration in the hollow site of the hexagonal ring is denoted as (u-h), while (u-br) indicates bridge site of the hexagonal ring. The same notation is used for the flat-lying (fl) geometry, whereby the dimer is parallel to the adsorption layer and the site refers to both the top and bottom atoms. For the heterodimers in the (u) configuration, the first species listed sits in the top position and the second closer to the adsorption layer. In all cases, the MAE is calculated as the difference in energy between a magnetization direction parallel to the dimer axis and perpendicular to the dimer axis. Ranges given express differences in electron correlation approximations. In the cases where two orientations are given (Ir₂ and Pt₂ on graphene/Cu(111) and Pt₂ on graphene), the first orientation corresponds to the ground state orientation. The second orientation is typically several tenths of an eV above the ground state and within energy ranges relevant to STM measurements.

This is discussed further later on. The configurational and magnetic properties of transition metal dimers on graphene were first explored by Johll *et al.* [186], where several important characteristics were elucidated. First, and perhaps unsurprisingly, the binding energy per atom of the dimers to the graphene are lower than the respective adatom case. In the context of STM studies, this implies that the dimers may be more mobile than their adatom counterparts, depending on their adsorption geometry. Second, the preferred configuration across all dimers adsorbed on graphene is an upright geometry, where the dimer axis is nearly perpendicular to the graphene plane and the bottom atom in the dimer is bound to the hollow site of the graphene. This has been confirmed by multiple studies, on graphene as well as on benzene rings. These results are tabulated in the corresponding columns of Table 5.1. Here, the notation (u-h) indicates an upstanding configuration with the bottom atom sitting in the 6-fold coordinated hollow site, (u-br) indicates an upstanding configuration with the bottom atom sitting in the bridge site between two carbon atoms, and (fl-h) and (fl-br) indicate the same for the flat-lying configuration. In this case, the dimer axis is parallel to the adsorption layer, and the adsorption site corresponds to both atoms in the dimer. These configurations are displayed in the schematics of Figure 5.1. More than one value given for the same geometry

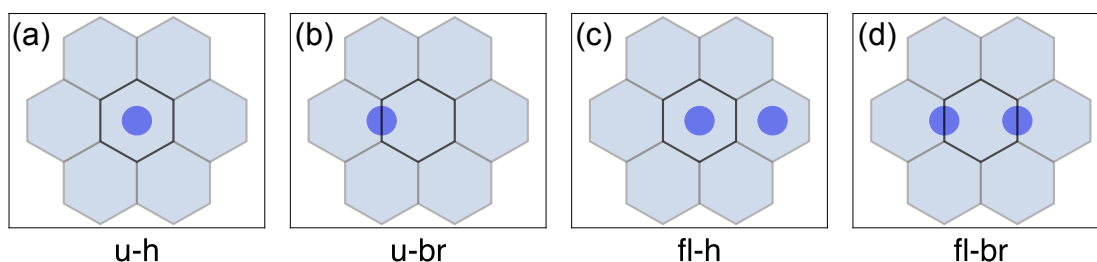


Figure 5.1: **Schematics of the adsorption site geometry of dimers on graphene.** Schematics (top-down view) of the different configurations used in Table 5.1: (a), upstanding in the hollow site (u-h), (b) upstanding in the bridge site (u-br), (c) flat-lying in the hollow site (fl-h), (d) flat-lying in the bridge site (fl-br). The bottom atom in the upstanding configurations in (a) and (b) is not visible.

reflects calculations from different studies relying on different methodologies. However, in the case of Ir_2 and Pt_2 on graphene/ $\text{Cu}(111)$ and Pt_2 on graphene, where multiple geometries are given, the first orientation (upper) corresponds to the ground state orientation and the second orientation (lower) is typically several tenths of an eV above this ground state, and within energy ranges relevant to STM measurements. In almost all cases [186–191, 200], the upstanding arrangement has the effect of enhancing the magnetic moment for the atom that sits furthest from the adsorption layer, relative to a flat-lying geometry. For the atom that sits closer to the adsorption layer, the opposite occurs, where the magnetic moment is reduced. In addition, charge transfer between the bottom atom and adsorption layer is common for many of the dimers [186].

The MAEs provided in Table 5.1 are calculated as the difference in energy between a magnetization direction parallel to the dimer axis and perpendicular to the dimer axis. In the gas phase, all dimers display anisotropy, due to the dominant axial symmetry intrinsic to the molecule. The larger values of Ir_2 and Pt_2 relative to Co_2 reflect the stronger spin-orbit coupling strength of the heavier $5d$ elements. When adsorbed on a benzene ring or on graphene, the dimers are subject to hybridization, charge transfer and crystal field effects that can either enhance or diminish the MAE. Clear differences can be seen for dimers that have $5d$ metal atoms sitting in the bottom site, closer to the adsorption layer, and those that have $3d$ metal atoms in the bottom site. For the heterodimers, the first atom listed is in the top site, while the second is in the bottom site (*i.e.*, TopBottom). Co_2 , PtCo , and IrCo all exhibit either a similar or enhanced MAE on benzene or graphene relative to the gas phase, while Ir_2 and Pt_2 exhibit a reduction or become non-magnetic altogether. This is consistent with bulk $5d$ metal systems where the extended orbitals hybridize with the surrounding ligand and quench the orbital moments. Evidently, placing a lighter, and less orbitally-extended $3d$ metal atom between the top atom and the adsorption layer better preserves the magnetic properties of the top atom, and the MAE of the dimer as a whole. For both the PtCo and IrCo heterodimers, the moment of the top atom is strongly enhanced with respect to their homodimer counterparts.

As mentioned previously, for practical purposes graphene needs to be surface-supported.

To determine whether this influences the properties of the dimers, Ref. [191] considers a graphene layer atop a Cu(111) substrate. The flat-lying state is the ground state for the $5d$ homodimers. This significantly reduces their MAE values to 1 meV or below. However, in both cases, a meta-stable upstanding configuration exists several tenths of an eV higher in energy than the ground state that partially restores that gas-like MAEs. For the heterodimers, the MAEs are minimally affected by the inclusion of the Cu(111) substrate because the adsorption geometry is maintained. Even for the Pt_2 dimer, the MAE in the upstanding configuration has an almost identical value on free-standing graphene and on surface-supported graphene. This suggests that the underlying metal substrate has little influence on the magnetic properties of dimers in the upstanding configuration. However, the substrate can influence the preferred adsorption geometry, which can then change the magnetic properties.

Clear from Table 5.1, the IrCo dimer possesses the highest calculated MAE at 204 meV. It is predicted to be upstanding on the graphene/Cu(111) surface and sit in the 6-fold coordinated hollow site of the graphene, with the Co atom sitting closer to the graphene and the Ir on top of Co. The Co atom transfers a large part of its orbital momentum to the Ir atom, which has a higher spin-orbit coupling, producing a higher MAE. These results are consistent for all adsorption layers considered, and have been confirmed by multiple studies relying on different methodologies [188, 190, 191]. As most of the magnetic moment lies in the top position of the dimer, the magnetic state mixing due to transverse terms in the crystal field should be largely mitigated. Thus, the high-lying Ir atom approaches a $C_{v\infty}$ symmetry, that should significantly hinder any magnetization reversals via QTM. The large MAE and upstanding geometry of IrCo heterodimer makes it the most promising magnetic system worthy of experimental investigation.

Other transition and rare-earth metal dimers, not included in Table 5.1, have similarly large predicted MAE values. However, they require substrates that are either oxidized, doped, or defective. IrTm, IrEr, and IrSm all possess MAEs greater than 135 meV when adsorbed to triple carbonyls on graphene [193]. The dimers are upstanding, and similar to the previous cases, the Ir atom sits in the top site, with the rare-earth sitting closer to the substrate. This study has not been verified with other methodologies, and creating a graphene sample with triple carbonyl groups introduces a host of other functional groups that may not be distinguishable with STM. For the dimers mentioned, adsorption to a quadruple carbonyl instead reduces the MAEs by more than a factor of 2 [193]. Thus, the complexity introduced by multiple functional groups instigates additional experimental challenges. In another study of Ir_2 dimers on graphene [195], if a boron atom replaces one of the 6 carbon atoms in the hexagonal ring, the dimers magnetic properties are restored, and possess an MAE of 130 meV. Similar to the un-doped graphene case, they prefer an upstanding configuration sitting in the hollow site. In addition, the boron tends to stabilize the upstanding configuration, increasing the energy difference between flat-lying and upstanding geometries. There are many techniques of producing boron-doped graphene in UHV with boron compositions of a few percent [201]. Choosing an *in situ* method that minimizes other surface contaminants and reduces experimental complexity is preferred for STM studies. Despite this, further studies using different DFT

methodologies are needed to confirm the restored magnetic properties of the Ir₂ dimer. In yet another study [192], the homodimer also has a large MAE of 126 meV when adsorbed on a boron vacancy site on *h*-BN. The dimer is again upstanding. Surface-supported single layers of *h*-BN on a variety of metal substrates can readily be produced via CVD [202–209] and boron vacancies of sufficiently large densities can be created via electron irradiation [210]. Also in this case, further studies should be done to confirm this MAE value. To summarize, using modified adsorption layers may provide an alternative pathway to creating atomic-scale magnetic systems with long spin lifetimes. However, the added complexity of introducing defects or other species in the experimental preparation makes the IrCo dimer on pristine graphene a much more attractive candidate to study, especially for comparable predicted MAEs.

For completeness, it is also worth noting a more recent study that predicted a high MAE for divalent lanthanide monoxide complexes on *h*-BN [196]. In contrast with the previous examples, they do not require modification of the adsorption layer. Most notably, the flat-lying DyO dimer has a predicted in-plane barrier exceeding 259 meV, primarily due to the strong crystal field produced by the oxygen, similar to the Ho SAM. The calculated energies of the low-lying multiplets of the DyO dimer are in agreement with previous spectroscopic data [211], implying a high degree of confidence in the predicted MAE. Future studies may consider investigation of this system.

5.2 Approaches for creation and identification

Two complementary active approaches are utilized to create and identify the IrCo heterodimer on graphene. Following the growth of the graphene layer on a metal substrate, the first active approach involves deposition of both species Co and Ir in sufficient quantities such that the formation of the dimer is statistically likely. Deposition of both species at 10 K should lead to the statistical growth of a multitude of species: Co, Ir, Co₂, Ir₂, IrCo, trimers, and larger clusters. By controlling the deposition amount of each species, the proportion of dimer species on the substrate can be tuned. The second active approach is via atomic manipulation of Co and Ir adatoms on the surface with the STM tip. If deposition amounts are small enough to guarantee an overwhelming majority proportion of adatom species, these can be manipulated for form dimers directly. *A priori*, the former approach is the easiest path towards creation, as the success of the latter is not necessarily guaranteed.

Passive techniques allow for further methods of identification. The active approaches discussed above involve direct influence over the proportion of dimer species on the substrate, while passive approaches rely on quantitative observations of the surface species already present. These observations include the apparent height of each species or any spectroscopic signatures that may be present. For example, the apparent heights of the Co₂, Ir₂, and IrCo dimers may all be unique and singularly-valued, allowing distinguishability through comparison of apparent height populations of samples prepared with Ir deposition alone, Co

deposition alone, and both Ir and Co depositions. Additionally, some species may display unique spectroscopic signatures, providing further means of identification.

These active and passive approaches are employed with the goal of creating and identifying the IrCo heterodimer. Following this, any magnetic signatures may be observed through the use of a magnetic tip, as was the case for the Dy and Ho SAMs in Chapters 3 and 4.

5.2.1 Statistical growth

Statistical growth occurs at deposition temperatures below which any thermally activated diffusion occurs. In this regime, the atoms simply stick to their impact site. Cluster growth in this regime is well-characterized by kinetic Monte Carlo (kMC) simulations. To briefly describe the technique [212], the behavior of any surface species is characterized by a discrete set of possible processes, each with corresponding rates. These are predefined, such that initial conditions are set, and the system is allowed to evolve for some time under the defined rates. Following this evolution, characterizations of the system, such as average cluster size, can be made. Deposition rates can also be included, where the total number of atoms on the surface increases. As an example, consider an atom adsorbed on a surface. The adsorption site is associated with a discrete number of adjacent sites, each with a corresponding energy barrier. Jumping over one of the barriers E_b to a new site can occur with rate $\nu_b = \nu_0 \exp(-E_b/k_B T)$, where E_b , ν_0 , and T are typically input parameters. The barrier height for diffusion to each adjacent site is not necessarily equal, but dependent on the local structure and environment. This is the case for adatoms on metal substrate-supported graphene [102, 213]. The probability of a given process, or jump over one of the barriers, is given by the magnitude of its rate relative to the rates of all other possible processes. A random number generator is used to determine which occurs, and the process is repeated for the new adsorption site. In this manner, diffusion over a 2D surface can be simulated, and further generalized to more than one atom. Conditions can be set so that when an atom finds itself adjacent to a filled site, a dimer is formed, and a new set of processes govern its evolution. For a range of coverages, kMC simulations have been used to accurately model the diffusion and distribution of adatoms, and formation of higher order clusters under a variety of growth conditions on 2D surfaces [214–219]. Of course, below a certain temperature, no thermally activated diffusion occurs, and the proportion of each species is solely governed by the amount deposited and the capture area of already adsorbed species. If an incident atom impinges the surface within the capture area of another adatom or cluster, coalescence occurs. This can be incorporated into the kMC models through conditionals. It is also worth noting that any transient mobility due to the dissipation of the adsorption energy across a few atomic sites may be present. However, it is only rarely observed for the deposition of gases [220, 221], and entirely absent in systems where metal is deposited on metal substrates [222, 223]. Whether it is present for metals deposited on metal substrate-supported graphene is unknown. Thus, kMC simulations can be used to inform our experimental investigations. Formation of the IrCo dimer requires sufficient coverage to form dimers, but not so much as to promote the formation of higher order clusters that complicate

species identification. By choosing coverages composed overwhelmingly of adatoms ($\approx 98\%$), with a small population of dimers ($\approx 2\%$), and negligible contribution of trimers ($\ll 1\%$), ideal growth conditions for creation and identification are promoted. A kMC simulation² for a hexagonal lattice such as graphene with isotropic barrier height reveals coverages around 5.5×10^{-3} ML result in these population proportions [214].

5.2.2 Choice of metal substrate

Cu(111) is used for the metal substrate in Ref. [191] primarily due to the free-standing nature of graphene when adsorbed on Cu(111), and the reduced computational complexity that arises when the two lattice constants can be treated as equal. Experimentally, other practical considerations must be made, primarily to the detriment of graphene on Cu(111). The temperature required to grow high-quality, single-domain graphene on Cu(111) is very close to the melting point [224–227], adding complexity to the experimental preparation. Additionally, in the studies of the Dy and Ho SAMs of Chapters 3 and 4, complementary XMCD measurements provided crucial information to understanding the magnetic properties of both systems. Thus, the ability to study the IrCo heterodimer with this technique is advantageous. Graphene filling factors of 1 are ideal for these ensemble measurements, as Co and Ir species deposited directly on the Cu(111) may have different magnetic signatures. This is also difficult to obtain with graphene grown on Cu(111) [224–228].

Fortunately, graphene can be grown on other metal substrates [140, 229–233]. In the context of the IrCo heterodimer, a weak graphene-substrate interaction is critical. Clear from Table 5.1, the MAE is preserved whether or not the Cu(111) substrate is included in the DFT study. This is primarily due to the upstanding configuration of the heterodimer, and the dominant contribution of the top-site Ir atom to the MAE [191]. In contrast, the geometric ground state of the homodimers in Table 5.1 do change with the inclusion of the Cu(111) substrate, influencing their magnetic properties. Whether this property is specific to Cu(111), or extends to other metal substrates has not been studied. However, graphene-copper hybridization is relatively weak [226], and the Co-graphene hybridization strong [191], resulting in the gas-like magnetic properties of the top-site Ir atom. A strong Co-graphene hybridization is also seen on an Ir(111) substrate [154], where the graphene-iridium hybridization is also weak [140]. Thus, the IrCo heterodimer may have very similar properties on graphene/Ir(111) as on graphene/Cu(111). In our experimental apparatus, we are able to produce a single layer of pristine, single-domain graphene on Ir(111) via CVD with a filling factor of 1 and little contamination [48, 50, 101, 102]. Therefore, we use it as our choice of substrate.

5.2.3 Beyond statistical growth

The growth conditions described in Section 5.2.1 may be ideal for creation and identification of the heterodimer, but by far do not represent the maximum possible population proportion

²See Figure 14b in Ref. [214].

relative to other species on the surface. This may not be ideal for ensemble XMCD measurements, where multiple magnetic species can convolute the signal from the primary species under study. Another benefit of choosing graphene/Ir(111) is its previous use as a template for self-assembly, through exploitation of the moiré pattern created by the lattice mismatch between the graphene and Ir(111) [48, 102, 234]. To maximize the population proportion of heterodimers, a growth procedure consisting of two deposition and annealing steps can be utilized. Co adatoms and Ir adatoms have different diffusion energy barriers E_b on graphene [213]. It is likely that this also is the case on graphene/Ir(111). As a result, the onset temperature of diffusion for each species is different. Diffusion within the moiré unit cell occurs at a lower temperature than diffusion between moiré cells, due to the higher energy barrier associated with the moiré relative to the graphene lattice sites [102]. If deposition is made in the statistical growth regime at coverages corresponding to an average of one adatom per moiré unit cell, a well-ordered superlattice will form at annealing temperatures between the onset temperatures of diffusion within the moiré cells and between the moiré cells, that results in an average of a single monomer per moiré cell. This procedure can be utilized for Ir and Co adatoms; whereby the species with the higher onset temperature of diffusion within the moiré cells is deposited and annealed first, creating a corresponding monomer superlattice. This is followed by deposition of the second species and a second annealing at the lower onset temperature of diffusion within the moiré cells. Because this temperature is lower for the second species relative to the first, the surface mobility of the first species remains constrained while the second species can diffuse towards the local minima within the moiré cell, ideally to where the first species is located, and form a heterodimer. Of course, this two-step procedure assumes no adatom-adatom interaction that inhibits dimer formation is present. If this is not the case, this process represents a potential pathway for the creation of a superlattice composed primarily of a single species: the heterodimer. It is not restricted to Ir and Co alone, but can be generalized to any two species with sufficiently different onset temperatures of diffusion within the moiré unit cells of substrate-supported graphene.

5.2.4 Atomic manipulation

As discussed in Section 2.1.3, atomic manipulation is a route for the construction of nanoscale objects. We explore the use of both families of atomic manipulation, parallel and perpendicular, using a W STM tip. At the coverages discussed in Section 5.2.1, the majority species should be adatoms. Manipulation is used, not only in attempt to create the IrCo heterodimer directly, but also Co_2 and Ir_2 . Doing so provides further verification of the characteristics of the homodimers, such that they can be distinguished from their monomer counterparts and the heterodimer itself.

5.3 Species observations

With all the previous considerations in mind, we perform STM measurements after the deposition of Co, Ir and both Co and Ir atoms on graphene/Ir(111). Both active and passive techniques are used to identify Ir, Co, Ir₂, Co₂, and IrCo, at or below coverages where only these species should be present.

5.3.1 Deposition of Ir alone

Figure 5.2a displays an apparent height histogram (187 total objects) of Ir deposited on graphene/Ir(111) at coverages between $0.7\text{--}1 \times 10^{-3}$ ML. Even at coverages well below 5.5×10^{-3} ML, two distinct apparent heights are observed: a lower species Ir_{low} around 200 pm and a higher species Ir_{high} around 280 pm. Figure 5.2b is an STM image displaying both species. Ir_{high} not only appears higher, but also consistently exhibits a larger lateral extension than Ir_{low}, regardless of the tip used. One might suspect the higher species to be the Ir₂ dimer, but upon bias pulses larger than ± 2 V in the vicinity of either species, alternation between Ir_{high} and Ir_{low} occurs. Figure 5.2b-c display two such alternations, where pulses of +2 V are applied in the vicinity of the two Ir_{high} species (indicated by the red ×), and a subsequent image at the same tunneling conditions is displayed in Figure 5.2c. The two Ir_{high} species present an apparent height now consistent with the other three Ir_{low} species. For comparison, the apparent height profiles of an Ir_{high} species (orange 2) and an Ir_{low} species (blue 1) are given in Figure 5.2d. Following the bias pulse, they both exhibit the same apparent height (Figure 5.2e). While only Ir_{high} → Ir_{low} is shown, the process is reversible, and does not depend on the sign of the bias pulse as long as it is greater than ± 2 V in magnitude. We therefore conclude that both species are Ir adatoms, and the difference in apparent height between the two species must be due to differences in adsorption site and/or charge state. While intriguing, discerning the origin of the difference is not directly relevant to the creation of the IrCo heterodimer.

Performing any perpendicular atomic manipulation on either the Ir_{high} or Ir_{low} typically result in the target adatom being picked up by the tip. This is confirmed by the increased scanning resolution achieved following the operation. Attempts at a subsequent dropping off of the atom are always unsuccessful, regardless of the particular tunneling parameters used. Neither species displays any consistent spectroscopic signatures in the energy range -500 meV to $+500$ meV. However, scanning the tip at high biases (in the range of the pulses used in Figure 5.2) not only results in adatoms switching between the high and low Ir adatoms, but in some cases, the creation of a new species not previously observed at these coverages. Figure 5.3 shows the result of such a manipulation. In Figure 5.3a, the STM image is populated with both Ir_{high} or Ir_{low} species. Three apparent height profiles from the image are displayed in Figure 5.3c. In particular, two Ir_{low} adatoms lie in close proximity to each other (indicated by the orange profile number 2). Following this image, a scan was then carried out at +2 V, before a subsequent image was taken at the same initial tunneling conditions (Figure 5.3b). Most notably, a new species appears at the location previously occupied by the two Ir_{low} adatoms.

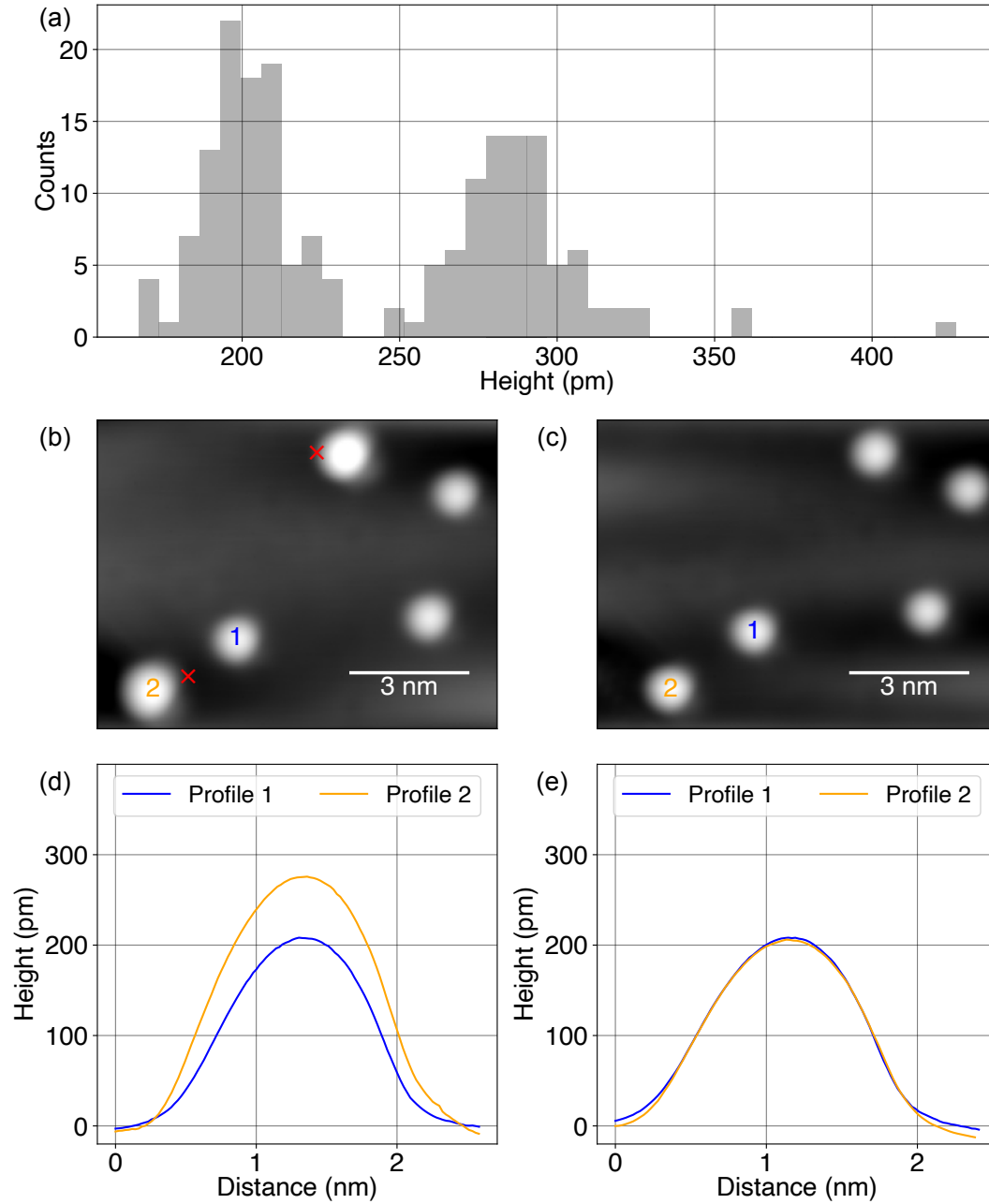


Figure 5.2: **Deposition of Ir on graphene/Ir(111).** (a), Apparent height histogram of Ir deposited on graphene/Ir(111) ($V_b = 150$ mV, $I_t = 100$ pA, $\Theta = 0.7\text{--}1 \times 10^{-3}$ ML, $T_{dep} \approx 10$ K, $T = 5$ K). (b,c), Sequence of STM images ($V_b = 150$ mV, $I_t = 100$ pA, $\Theta = 1 \times 10^{-3}$ ML, $T = 5$ K) showing the alternation between high and low species via +2 V bias pulse adjacent to adatom (red \times). Numbers indicate line profiles in (d) and (e). In (b), two Ir_{high} (lower left and upper middle) and three Ir_{low} (remaining) are present. Following the bias pulses, all five adatoms exhibit apparent heights of the low species (c). Although only $\text{Ir}_{high} \rightarrow \text{Ir}_{low}$ is shown, the process is reversible.

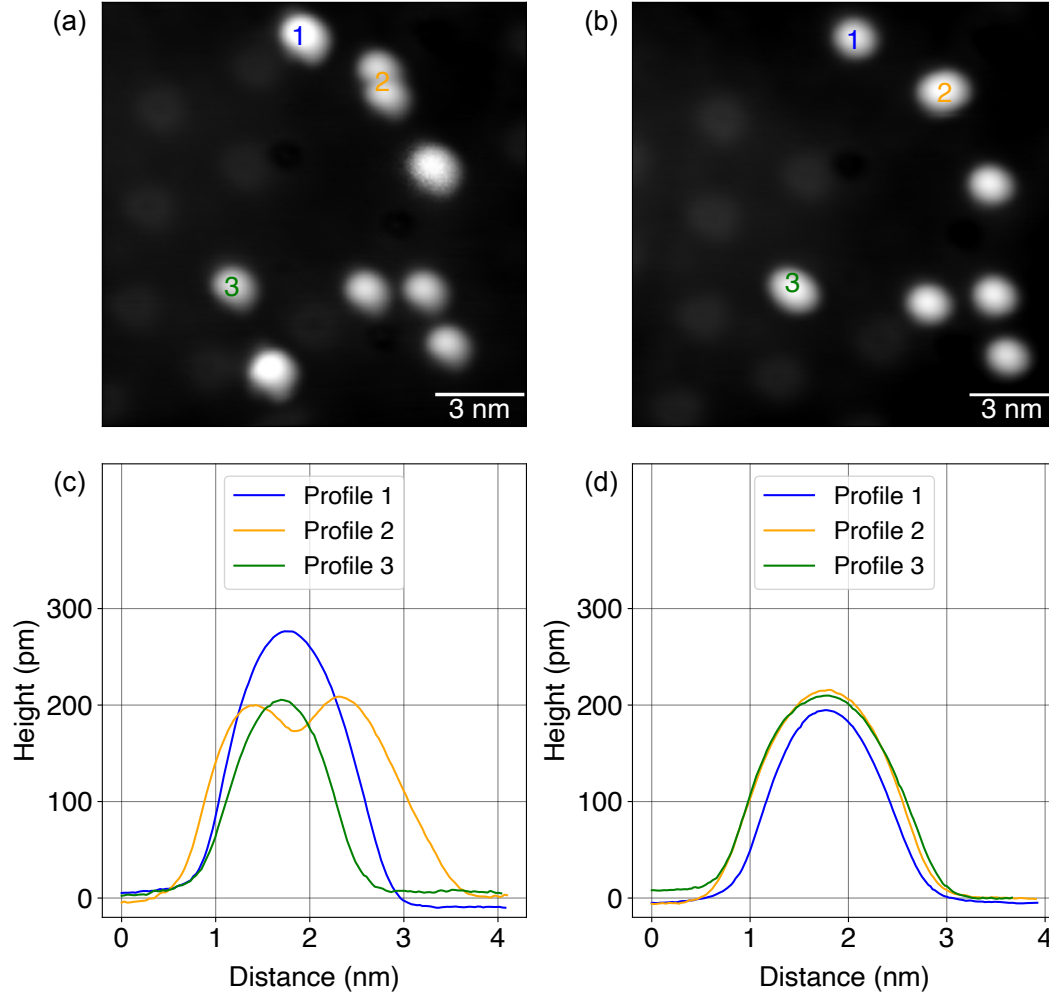


Figure 5.3: **Creation of Ir_2 dimers on graphene/Ir(111).** (a,b), Sequence of STM images ($V_b = 150$ mV, $I_t = 100$ pA, $\Theta = 1 \times 10^{-3}$ ML, $T_{dep} \approx 10$ K, $T = 5$ K) showing the creation of two Ir_2 dimers. A scan of the same sample area was taken at +2 V following the image in (a), and before the image in (b). Three apparent height profiles from (a) are pictured in (c): an Ir_{high} (blue 1), two Ir_{low} (yellow 2), and an Ir_{low} (green 3). Following the high bias scan, the same profiles are displayed in (d). The Ir_{high} changes to Ir_{low} (blue 1). The two Ir_{low} become a species not previously observed at these coverages, characterised by a slight increase in apparent height by ~ 15 pm and oblate shape (yellow 2). The same occurs for the Ir_{low} (green 3), where the Ir_{high} in the vicinity is also no longer present. The apparent height profiles 2 and 3 in (d) are taken along the semi-major axes of the oblate species.

The new species has a characteristic oblate shape, not previously observed at these coverages, and appears slightly higher (~ 15 pm) than Ir_{low} . Also notable, the same species also appears at the location previously occupied by an Ir_{low} adatom (green 3), while the Ir_{high} adatom at the bottom of the image has conspicuously disappeared. The apparent height profiles of the new species, taken along the semi-major axis, are displayed in Figure 5.3d. Taken along the semi-minor axes, they exhibit the same width as the Ir_{low} species. For comparison, the Ir_{low}

(blue 1) that was previously an Ir_{high} in Figure 5.3a is also pictured. The flat-lying geometry is also consistent with experimental observations of the Ir_2 dimer on graphene/Pt(111) [235]. The graphene-metal interaction that occurs for graphene/Pt(111) is weak [230], similar to graphene/Ir(111) and graphene/Cu(111), thus similar characteristics for the Ir_2 dimer are expected. The angle between the semi-major axes of the two dimers is approximately 120° , also consistent with a flat-lying geometry where both atoms are adsorbed in unit-cell-adjacent hollow-hollow, bridge-bridge, or atop carbon-carbon sites.

The observations illustrated in Figures 5.2 and 5.3 are consistent with Ir adatoms sitting in two possible adsorption sites on graphene/Ir(111), with apparent heights of around 200 pm and 280 pm, and Ir_2 dimers possessing a flat-lying geometry with apparent height of around 215 pm. At coverages of 1×10^{-3} ML, the species are overwhelmingly adatoms ($\gg 99.9\%$), consistent with kMC simulations of pure statistical growth [214]. For the adatoms, switching between sites is possible for tunnel biases above 2 V. It is unclear whether an excited upstanding state for the Ir_2 dimer exists, and this should be investigated further.

5.3.2 Deposition of Co alone

Figure 5.4a shows an apparent height histogram of Co deposited on graphene/Ir(111) at coverages of 5×10^{-3} ML. Similar to the Ir, two distinct apparent heights are observed: a lower majority species around 270 pm and a higher minority species around 350 pm. Two sets of apparent height profiles are displayed in Figure 5.4b, corresponding to the tunneling conditions in Figure 5.4a (S1: $V_b = 100$ mV, $I_t = 50$ pA), and the tunneling conditions in Figure 5.2a and Figure 5.4c-d (S2: $V_b = 150$ mV, $I_t = 100$ pA), for direct comparison to the Ir species. Reliable lateral manipulation of the lower Co species is possible with the W tip. This is done by approaching the tip adjacent to lower species, in a position opposite the desired direction of motion (*i.e.*, a push), by increasing the tunnel current to 7-9 nA ($V_b = 50$ mV) with the feedback loop closed. Moving the tip laterally at scan speed $v_t = 10$ nm/min "pushes" the Co species. An operation of this type can be used to push two of the lower species together, as pictured in Figure 5.4c-d, to create the higher species. We therefore conclude the higher species is the Co_2 dimer.

The observation of two species in the apparent height histogram of Figure 5.4a is consistent with a previous investigation of Co on graphene/Ir(111) for similar coverages³ [154]. The large percentage of Co_2 dimers ($\sim 20\%$) at coverages of 5×10^{-3} ML is much larger than kMC simulations indicate for the statistical growth regime ($\approx 2\%$). This implies that the onset temperature of diffusion must be between 5 K and the deposition temperature $T_{\text{dep}} \approx 10$ K, as both monomers and dimers are immobile during STM measurements. Diffusion across a few atomic sites must occur between the deposition and STM observation. Spectroscopic features are also observed for the lower species, similar to Co adatoms on graphene/Pt(111) [36]. In this case, the magnitude of the spectroscopic feature was found to be related to the number

³See Figure S3 in Ref. [154].

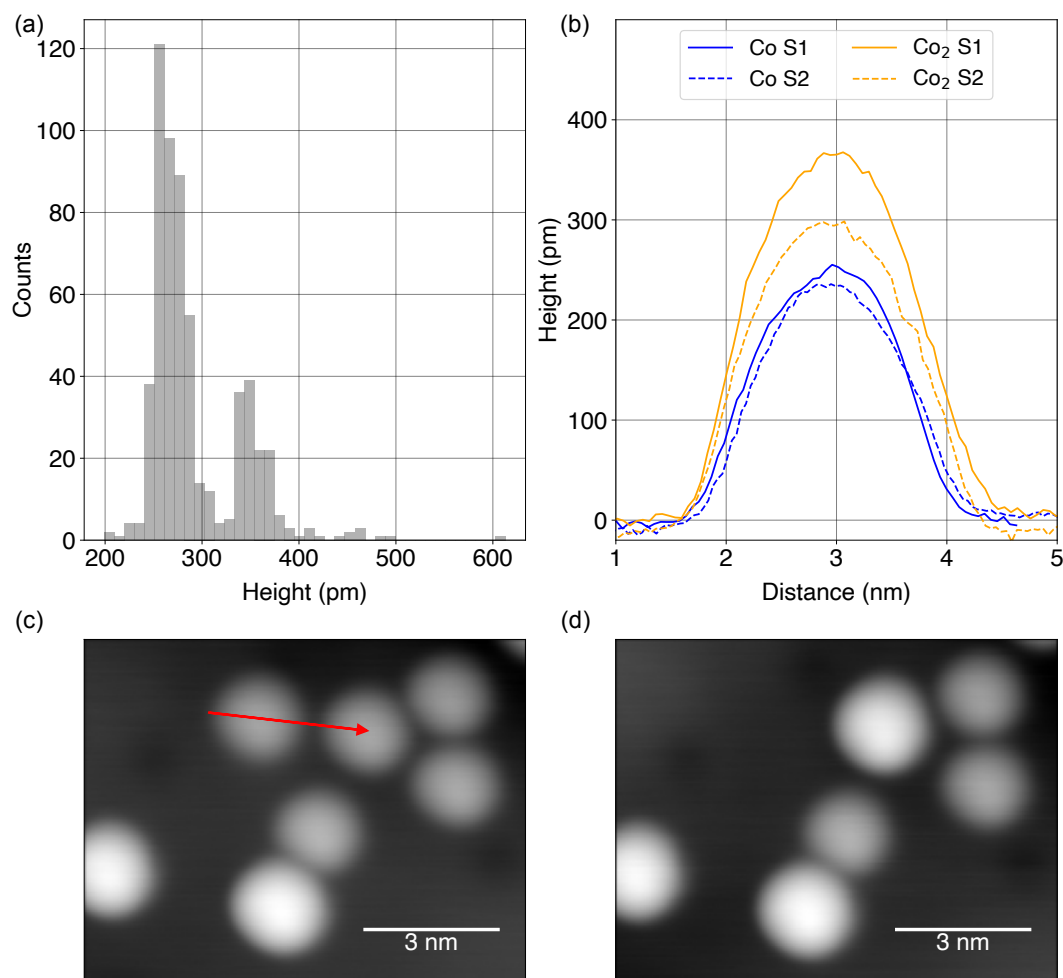


Figure 5.4: **Deposition of Co on graphene/Ir(111).** (a), Apparent height histogram of Co deposited on graphene/Ir(111) ($V_b = 100$ mV, $I_t = 50$ pA, $\Theta = 0.005$ ML, $T_{dep} \approx 10$ K, $T = 5$ K). (b), Apparent height profiles of Co and Co₂ at two different STM conditions, S1 ($V_b = 100$ mV, $I_t = 50$ pA) and S2 ($V_b = 150$ mV, $I_t = 100$ pA). (c,d), Sequence of STM images showing the creation of the Co₂ dimer via atomic manipulation ($V_b = 150$ mV, $I_t = 100$ pA, $\Theta = 0.005$ ML, $T = 5$ K). The red arrow in (c) indicates the path of the STM tip during the manipulation ($V_b = 50$ mV, $I_t = 7$ nA, scan speed of the tip $v_t = 10$ nm/min).

of hydrogen atoms coordinated with the Co adatom (*e.g.*, Co, CoH, CoH₂, and CoH₃). The hydrogen-coordinated species also exhibited a reduced apparent height, relative to bare Co. We observe similar characteristics for the lower Co species on graphene/Ir(111): variations in the magnitude of the spectroscopic features and a reduced apparent height on some of the objects. These observations are consistent with the lower species identified as the Co monomer and the higher species, the Co₂ dimer. The Co spectroscopic features are probably magnetic, as observed for the graphene/Pt(111) system [36], but they are not directly relevant to the creation of the IrCo heterodimer. On the other hand, approximately 5 - 10 % of the Co monomers exhibit a reduced apparent height, indicating a commensurate amount of hydrogen present. In addition, we note that we do not observe any spectroscopic signatures

on the Co₂ dimers.

5.3.3 Deposition of both Co and Ir

The depositions of Ir alone and Co alone allowed for the identification of the Ir and Co monomers, as well as the Ir₂ and Co₂ dimers. The Ir monomer has two possible adsorption sites. At tunneling conditions of $V_b = 150$ mV and $I_t = 100$ pA, these exhibit apparent heights around 200 pm and 280 pm, while Ir₂ dimers possess a flat-lying geometry with apparent height of around 215 pm. At the same tunneling conditions, the Co monomer exhibits an apparent height of around 240 pm, and the Co₂ dimers an apparent height of around 300 pm. Thus, upon deposition of both species in sufficient quantities, we expect additional species to appear, mainly the IrCo heterodimer, and with a much lower population proportion, the IrCo₂ trimer. Reducing the Co coverage to 1×10^{-3} ML reduces the ratio of Co₂ dimers to Co monomer to below 0.05. Assuming a similar capture radius for Co and Co₂, subsequent deposition of Ir at similar coverages to those used in Figures 5.2 and 5.3 will lead to the formation of IrCo₂ and IrCo with an identical population proportion of below 0.05, respectively. This ensures, by at least a factor of 20, heterodimer formation is more likely than IrCo₂ formation. At these total coverages, we estimate a heterodimer population proportion on the order of 1 % of all species.

In addition, reliable lateral manipulation of the Co monomers permits an attempt to form the IrCo heterodimer by "pushing" a Co adatom towards an Ir adatom. This procedure was rigorously attempted for both Ir_{low} and Ir_{high}. Unfortunately, at the scan parameters required to move the Co adatoms, the procedure consistently results in the Ir adatom being picked up by the STM tip.

Figure 5.5a-c displays three STM images of a new species observed following the deposition of both Co and Ir at these coverages. Roughly 1 is observed for every 100-200 Co, Co₂, and Ir species, consistent with expectations for the IrCo heterodimer. Under stable imaging conditions, the species exhibits apparent height around 400 pm, revealed by the height profiles in Figure 5.5d of the three objects indicated in Figure 5.5a-b. The profile of the fourth object in Figure 5.5c is too distorted to be meaningful. The objects are weakly bound to the graphene, as demonstrated by their tendency to jump several nanometers if perturbed strongly by the tip, and display a high degree of instability under typical tip scan speeds (~ 10 nm/s). These characteristics are consistent with the upstanding geometry of the IrCo heterodimer. In addition, DFT studies indicate the binding energy per atom for dimers is lower than the respective adatom case [186], implying that in an upstanding geometry with only the bottom Co bound to the graphene, the IrCo dimer is more weakly bonded than the Co monomer. The Co monomer is fairly mobile under tip manipulation, thus the IrCo susceptibility to tip perturbations is not surprising. If the tip is placed directly above, the species exhibit discrete changes in ΔZ , pictured in the TS trace in Figure 5.5e. The trace was taken above the fourth object in Figure 5.5c at tunneling conditions $V_b = 400$ mV, $I_t = 500$ pA. Below 300 mV, no

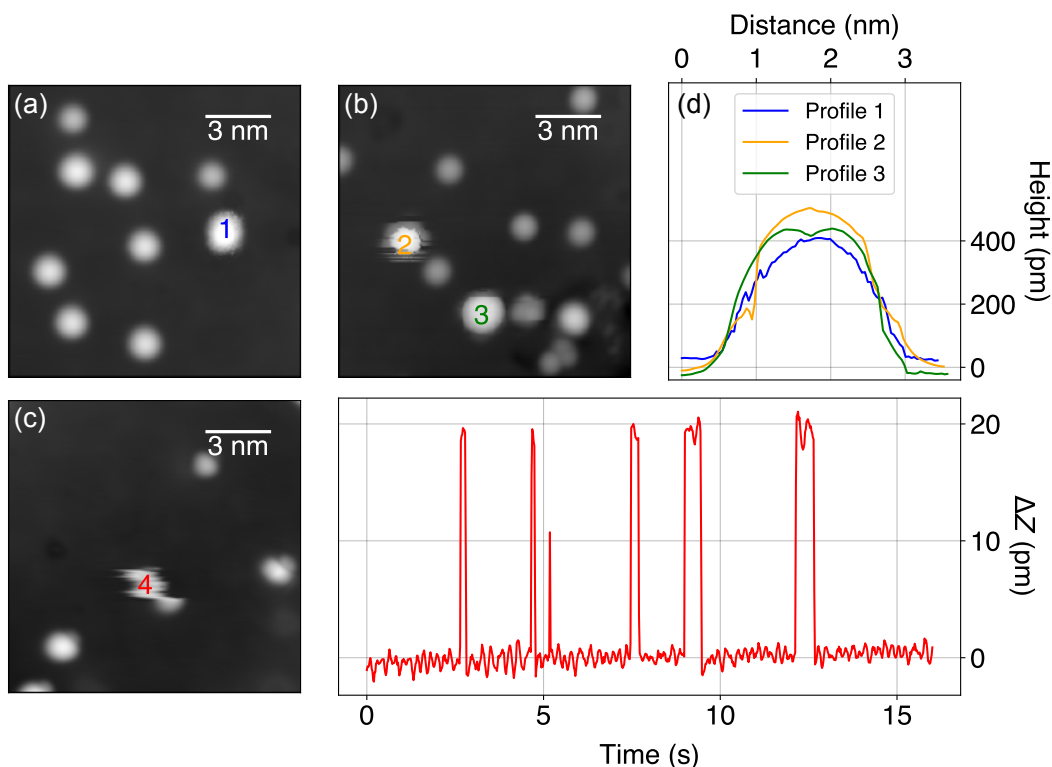


Figure 5.5: **Appearance of the IrCo heterodimer on graphene/Ir(111) with a non-magnetic tip.** (a-c), STM images showing the appearance of a larger species upon deposition of both Co and Ir ($V_b = 150$ mV, $I_t = 100$ pA, $\Theta_{Ir} = \Theta_{Co} = 1 \times 10^{-3}$ ML, $T_{dep} \approx 10$ K, $T = 5$ K). (d), Apparent height profiles of the higher species in (a) and (b). The profile of 4 in (c) is too distorted to be meaningful. (e), TS trace with feedback loop closed ($V_b = 400$ mV, $I_t = 500$ pA) taken above 4 in (c).

switching behavior is observed. A two-state TS trace is typical of all new species, although the ΔZ and threshold tunnel bias for switching may vary. As the tip used is non-magnetic (W), we suspect these are conformational rotations, where the dimer axis is no longer perpendicular to the graphene, or hopping between adsorption sites.

The previous considerations strongly indicate that this new species at around 400 pm apparent height is the IrCo heterodimer. To determine whether it is magnetic, we employ a MnNi tip, as was used to investigate the Dy and Ho SAMs in Chapters 3 and 4.

5.4 Magnetic signatures

Figure 5.6 displays several STM images of the IrCo species using a magnetic STM tip. In Figure 5.6a, two IrCo dimers are in close proximity to each other. They appear at around 400 pm (see profiles in Figure 5.6c), similar to the height exhibited with a non-magnetic tip. To determine whether the species exhibits any spin-dependent signal, a small amount of Dy atoms are deposited ($\Theta_{Dy} = 6 \times 10^{-4}$ ML), in order to test the polarization of the tip.

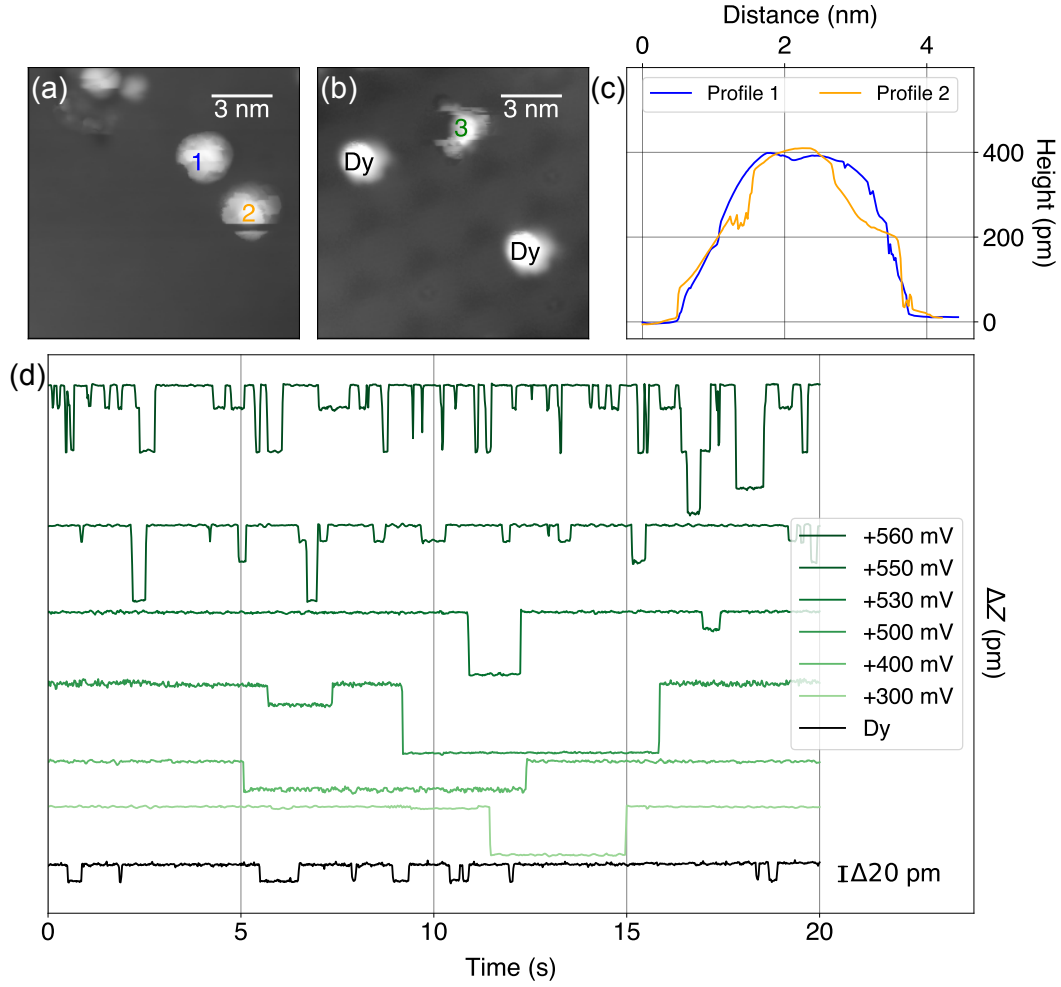


Figure 5.6: Appearance of the IrCo heterodimer on graphene/Ir(111) with a magnetic tip. (a-b), STM image showing two IrCo heterodimers ($V_b = 150$ mV, $I_t = 100$ pA, $\Theta_{Co} = 1 \times 10^{-3}$ ML, $\Theta_{Ir} = 2 \times 10^{-3}$ ML, $T_{dep} \approx 10$ K, $T = 5$ K). (b), IrCo heterodimer adjacent to two Dy adatoms (same conditions as (a), with additional deposition $\Theta_{Dy} = 6 \times 10^{-4}$ ML). The Dy adatoms appear at a similar height, but exhibit switching behavior in the conditions discussed in Chapter 3. (c), Apparent height profiles of the heterodimers in (a). The apparent height is the same whether using a magnetic tip or non-magnetic tip. (d), Series of TS traces taken on one of the Dy adatoms (black, $V_b = 8$ mV, $I_t = 10$ pA) and on the IrCo heterodimer (green, $V_b = 300 - 560$ mV, $I_t = 1$ nA) in (b) with the feedback loop closed. Traces are shifted for clarity. $\Delta Z = 20$ pm on the Dy trace for reference.

Figure 5.6b displays an unstable IrCo heterodimer (green 3) with two Dy adatoms in the vicinity. The tip polarization is confirmed by measuring above one of the Dy adatoms (black trace in Figure 5.6d, $V_b = 8$ mV, $I_t = 10$ pA). The Dy exhibit a two-state TS with $\Delta Z = 20$ pm, consistent with a finite, out-of-plane tip polarization. The tip is then moved above the IrCo heterodimer, and a multi-state TS is observed for a range of tunnel biases (green traces in Figure 5.6d, $V_b = 300 - 560$ mV, $I_t = 1$ nA). This is in contrast to the two-state TS consistently observed with a non-magnetic tip, suggesting a possible magnetic origin to the additional states. As the

tunnel bias is increased, the frequency of steps increases, consistent with excitations induced by tunnelling electrons. Also of note, the observed steps occur in multiples of $\Delta Z \approx 20$ pm, with the largest observed being 180 pm.

The observations in Figure 5.6d indicate a possible magnetic origin to the multi-state TS. However, it does not completely preclude a non-magnetic origin. To observe the TS, the onset tunnel bias for all tips is above 200 mV, consistent with the DFT-derived MAE value. However, further investigation, with both a magnetic and non-magnetic tip, are needed to confirm the observations in Figure 5.5e and Figure 5.6d.

5.5 Outlook

This chapter motivated the study of a new system– the IrCo heterodimer adsorbed on graphene, inspired by the DFT-derived upstanding geometry and high MAE, the enhanced magnetic moment of the top Ir atom, and the perfect axial symmetry. Further, the strategies to create and identify the heterodimer were elucidated, as well as procedures to maximize the heterodimer population on any metal-supported-graphene substrate. The initial strategies are then executed, where a combination of statistical growth and atomic manipulation allowed for successful identification of Ir and Co monomers, Ir₂ and Co₂ homodimers, and the IrCo heterodimer on graphene/Ir(111). The Ir₂ homodimer can be formed by via pulses or scanning at tunnel biases greater in magnitude than ± 2 V, and the Co₂ homodimer through lateral manipulation. The IrCo heterodimer is highly mobile on the graphene surface and displays conformational instability, consistent with its predicted upstanding geometry. Despite this, we have demonstrated that measurement via STM and SP-STM is possible. The heterodimer exhibits a two-state TS under a non-magnetic tip and a multi-state TS under a magnetic tip, indicating a possible magnetic origin to some of the observed steps in ΔZ . The onset tunnel bias which these occur is consistent with the MAE values calculated from DTF studies. Further studies are needed to confirm this magnetic origin, and the larger predicted MAE of the heterodimer. Methods of stabilizing the heterodimer can also be investigated: via doping of the graphene, or perhaps through the deposition of inert gases such as Xe placed in close proximity. Following this, the procedures for maximizing the heterodimer population can be executed, to allow for complementary XMCD measurements.

6 Outlook

The goal of this thesis was twofold: to use SP-STM to further advance the understanding of the interactions that determine the magnetic stability of the Dy and Ho SAMs, and to use insights from these systems to search for new systems exhibiting similar, if not more exceptional, magnetic characteristics. Here, the results elucidated in the preceding Chapters are briefly summarized to demonstrate the achievement of these goals, followed by a glimpse at future studies that may be done.

In Chapter 3, the necessity of including the intra-atomic exchange coupling to correctly describe spin lifetimes and reading/writing mechanisms in rare-earth adatoms was ascertained. In addition, both nuclear spin cases of Dy are compared, and shown to produce similar behavior in the temperature and bias ranges probed by SP-STM. The multiplicity of spin states upon inclusion of the hyperfine interaction necessitates the use of an efficient algorithm to differentiate the location and size of avoided level crossings. The Python programming language provides an efficient, easy-to-use environment to implement such an algorithm, and the entirety of scattering processes and Hamiltonian diagonalizations required for modelling spin systems. Furthermore, this allows for modeling of XMCD magnetization sweeps, which demonstrate that the chosen crystal field parameters reproduce critical characteristics of the experimental observations. In the light of these findings, all previous and future works should account for the intra-atomic exchange whenever several electronic shells show spin polarization.

In Chapter 4, novel measurement protocols are used to determine the zero-field stability of Ho SAMs, and the correct ground state model. Writing the magnetic state of a SAM via magnetic field sweeps across an avoided level crossing is a low-energy alternative to photon or electron-induced reversal mechanisms. Reconciling the experimental observations across multiple studies using both local and ensemble techniques [42, 47, 49, 51, 175, 183] with DFT calculations [51, 152, 183] requires specific knowledge of the higher energy states in the level diagram. Unfortunately, these states are difficult to access, as only states that participate directly in relaxation mechanisms are experimentally visible. For the states that participate indirectly in relaxation mechanisms, such as the 2-phonon Raman and Orbach processes,

their location must be inferred from the envelope calculations of Equations 2.43 and 2.45. As we have seen, determining the correct crystal field parameters is not trivial, as many parameter sets exist that are all consistent with the experimental observations. This is evident not only in the two sets presented in Section 4.3, but also in the historical progression of Ho SAM studies listed above.

In Chapter 5, the study of the IrCo heterodimer adsorbed on graphene was motivated with stability considerations derived from studies of the Dy and Ho SAMs, and DFT studies. Strategies of engineering these heterodimers using statistical growth and atomic manipulation were discussed and successfully implemented. The heterodimer is highly mobile on the graphene surface and displays conformational instability, consistent with its predicted upstanding geometry. Despite this, we have demonstrated that measurement via STM and SP-STM is possible. The heterodimer exhibits a two-state TS under a non-magnetic tip and a multi-state TS under a magnetic tip, indicating a possible magnetic origin to some of the observed steps in ΔZ . Additional study is needed to disentangle the observations made thus far. Promising future investigations are elucidated below.

For the IrCo heterodimer, further investigation into the TS exhibited under a non-magnetic and magnetic tip should be done. First, sufficient statistics of the two-state switching as a function of bias with a non-magnetic tip should be acquired across multiple heterodimers. This may clarify the origin and mechanism behind the switching signal, which propagates to the multi-state TS observed with a magnetic tip. Successful differentiation between signals with origins in conformational rotations or adsorption site alternations from signals of magnetic origin will allow for a validation of the high MAE value predicted by the DFT studies.

Concurrent with these investigations, the growth procedure elucidated in Section 5.2.3 can be attempted and verified using STM. If this is successful, XMCD investigations can be performed to further complement the SP-STM results.

In addition to the IrCo heterodimer, the DyO dimer discussed in Section 5.1 should also be explored. The consistency between the DFT calculations and experimental spectroscopy is indicative of valid calculations of the large MAE value.

Research in magnetism continues to be driven by technological innovation. Understanding the novel properties that arise as the size of functional devices approaches a few atoms or less is critical to the integrity and reliability of such devices. As demonstrated in this thesis, STM and SP-STM are viable techniques to derive magnetic information from systems on this scale. In turn, this knowledge informs the design of future systems, perpetuating the cycle of technological innovation and progress in fundamental physics research.

Bibliography

- ¹Aristotle, *Aristotle's on the soul: and, on memory and recollection*. (Green Lion Press, 2001).
- ²S. Kuo, *Dream pool essays* (HardPress, 2016).
- ³W. Gilbert, *De magnete* (Peter Short, 1600).
- ⁴T. Thomson, R. Phillips, E. Brayley, and B. H. Library, *The annals of philosophy* (Baldwin, Craddock, and Joy, 1820).
- ⁵D. Griffiths, *Introduction to electrodynamics* (Prentice Hall, 1981).
- ⁶P. Weiss, "La variation du ferromagnetisme avec la température", *C. R. Acad. Sci.* (1906).
- ⁷C. Blondel, A.-M. Ampère et la création de l'électrodynamique, 1820-1827 (Bibliothèque Nationale, 1982).
- ⁸M. Planck, "Ueber das Gesetz der Energieverteilung im Normalspectrum", *Ann. Phys.* **309**, 553–563 (1901) 10.1002/andp.19013090310.
- ⁹N. Bohr, "I. On the constitution of atoms and molecules", *Lond. Edinb.* **26**, 1–25 (1913) 10.1080/14786441308634955.
- ¹⁰W. Gerlach and O. Stern, "Der experimentelle Nachweis der Richtungsquantelung im Magnetfeld", *Zeits. f. Phys.* **9**, 349–352 (1922) 10.1007/BF01326983.
- ¹¹E. Schrödinger, *Collected papers on wave mechanics* (AMS Chelsea Pub., 2003).
- ¹²W. Heisenberg, "Über quantentheoretische Umdeutung kinematischer und mechanischer Beziehungen.", *Zeits. f. Phys.* **33**, 879–893 (1925) 10.1007/BF01328377.
- ¹³P. Dirac, "The quantum theory of the electron", *Roy. Soc. Proc.* **117**, 610–624 (1928) 10.1098/rspa.1928.0023.
- ¹⁴W. Heisenberg, "Zur Theorie des Ferromagnetismus", *Zeits. f. Phys.* **49**, 619–636 (1928) 10.1007/BF01328601.
- ¹⁵E. Stoner and E. Wohlfarth, "A mechanism of magnetic hysteresis in heterogeneous alloys", *Roy. Soc. Proc.* **240**, 599–642 (1948) 10.1098/rsta.1948.0007.
- ¹⁶P. Anderson, "Localized magnetic states in metals", *Phys. Rev.* **124**, 41–53 (1961) 10.1103/PhysRev.124.41.
- ¹⁷J. Hubbard, "Electron correlations in narrow energy bands", *Proc. R. Soc. A: Math. Phys. Eng. Sci.* **276**, 238–257 (1963) 10.1098/rspa.1963.0204.

- ¹⁸O. Pietzsch, A. Kubetzka, M. Bode, and R. Wiesendanger, “Real-space observation of dipolar antiferromagnetism in magnetic nanowires by spin-polarized scanning tunneling spectroscopy”, *Phys. Rev. Lett.* **84**, 5212–5215 (2000) 10.1103/PhysRevLett.84.5212.
- ¹⁹M. Pratzner, H. Elmers, M. Bode, O. Pietzsch, A. Kubetzka, and R. Wiesendanger, “Atomic-scale magnetic domain walls in quasi-one-dimensional Fe nanostripes”, *Phys. Rev. Lett.* **87**, 127201 (2001) 10.1103/PhysRevLett.87.127201.
- ²⁰A. Wachowiak, J. Wiebe, M. Bode, O. Pietzsch, M. Morgenstern, and R. Wiesendanger, “Direct observation of internal spin structure of magnetic vortex cores”, *Science* **298**, 577–580 (2002) 10.1126/science.1075302.
- ²¹W. Wulfhekel and J. Kirschner, “Spin-polarized scanning tunneling microscopy of magnetic structures and antiferromagnetic thin films”, *Ann. Rev. Mater. Res.* **37**, 69–91 (2007) 10.1146/annurev.matsci.37.052506.084342.
- ²²A. Kubetzka, O. Pietzsch, M. Bode, and R. Wiesendanger, “Magnetism of nanoscale Fe islands studied by spin-polarized scanning tunneling spectroscopy”, *Phys. Rev. B* **63**, 140407 (2001) 10.1103/PhysRevB.63.140407.
- ²³A. Yamasaki, W. Wulfhekel, R. Hertel, S. Suga, and J. Kirschner, “Direct observation of the single-domain limit of Fe nanomagnets by spin-polarized scanning tunneling spectroscopy”, *Phys. Rev. Lett.* **91**, 127201 (2003) 10.1103/PhysRevLett.91.127201.
- ²⁴M. Bode, O. Pietzsch, A. Kubetzka, and R. Wiesendanger, “Shape-dependent thermal switching behavior of superparamagnetic nanoislands”, *Phys. Rev. Lett.* **92**, 067201 (2004) 10.1103/PhysRevLett.92.067201.
- ²⁵O. Pietzsch, A. Kubetzka, M. Bode, and R. Wiesendanger, “Spin-polarized scanning tunneling spectroscopy of nanoscale Cobalt islands on Cu(111)”, *Phys. Rev. Lett.* **92**, 057202 (2004) 10.1103/PhysRevLett.92.057202.
- ²⁶O. Pietzsch, S. Okatov, A. Kubetzka, M. Bode, S. Heinze, A. Lichtenstein, and R. Wiesendanger, “Spin-resolved electronic structure of nanoscale Cobalt islands on Cu(111)”, *Phys. Rev. Lett.* **96**, 237203 (2006) 10.1103/PhysRevLett.96.237203.
- ²⁷S. Rusponi, N. Weiss, T. Cren, M. Eppel, and H. Brune, “High tunnel magnetoresistance in spin-polarized scanning tunneling microscopy of Co nanoparticles on Pt(111)”, *Appl. Phys. Lett.* **87**, 162514 (2005) 10.1063/1.2077856.
- ²⁸S. Krause, L. Berbil-Bautista, G. Herzog, M. Bode, and R. Wiesendanger, “Current-induced magnetization switching with a spin-polarized scanning tunneling microscope”, *Science* **317**, 1537–1540 (2007) 10.1126/science.1145336.
- ²⁹W. Hofer, K. Palotás, S. Rusponi, T. Cren, and H. Brune, “Role of Hydrogen in giant spin polarization observed on magnetic nanostructures”, *Phys. Rev. Lett.* **100**, 026806 (2008) 10.1103/PhysRevLett.100.026806.
- ³⁰S. Krause, G. Herzog, T. Stapelfeldt, L. Berbil-Bautista, M. Bode, E. Vedmedenko, and R. Wiesendanger, “Magnetization reversal of nanoscale islands: how size and shape affect the Arrhenius prefactor”, *Phys. Rev. Lett.* **103**, 127202 (2009) 10.1103/PhysRevLett.103.127202.

- ³¹A. J. Heinrich, J. Gupta, C. Lutz, and D. Eigler, “Single-atom spin-flip spectroscopy”, *Science* **306**, 466–469 (2004) 10.1126/science.1101077.
- ³²C. Hirjibehedin, C. Lutz, and A. J. Heinrich, “Spin coupling in engineered atomic structures”, *Science* **312**, 1021–1024 (2006) 10.1126/science.1125398.
- ³³A. Singha, F. Donati, F. Natterer, C. Wäckerlin, S. Stavrić, Z. Popović, Ž. Šljivančanin, F. Patthey, and H. Brune, “Spin excitations in a $4f-3d$ heterodimer on MgO”, *Phys. Rev. Lett.* **121**, 257202 (2018) 10.1103/PhysRevLett.121.257202.
- ³⁴C. Hirjibehedin, C. Lin, A. Otte, M. Ternes, C. Lutz, B. Jones, and A. J. Heinrich, “Large magnetic anisotropy of a single atomic spin embedded in a surface molecular network”, *Science* **317**, 1199–1203 (2007) 10.1126/science.1146110.
- ³⁵A. Otte, M. Ternes, K. von Bergmann, S. Loth, H. Brune, C. Lutz, C. Hirjibehedin, and A. J. Heinrich, “The role of magnetic anisotropy in the Kondo effect”, *Nat. Phys.* **4**, 847–850 (2008) 10.1038/nphys1072.
- ³⁶F. Donati, Q. Dubout, G. Autès, F. Patthey, F. Calleja, P. Gambardella, O. V. Yazyev, and H. Brune, “Magnetic moment and anisotropy of individual Co atoms on graphene”, *Phys. Rev. Lett.* **111**, 236801 (2013) 10.1103/PhysRevLett.111.236801.
- ³⁷M. Pivetta, F. Patthey, I. Di Marco, A. Subramonian, O. Eriksson, S. Rusponi, and H. Brune, “Measuring the intra-atomic exchange energy in rare-earth adatoms”, *Phys. Rev. X* **10**, 115417 (2020) 10.1103/PhysRevX.10.031054.
- ³⁸F. Meier, L. Zhou, J. Wiebe, and R. Wiesendanger, “Revealing magnetic interactions from single-atom magnetization curves”, *Science* **320**, 82–86 (2008) 10.1126/science.1154415.
- ³⁹S. Loth, M. Etzkorn, C. Lutz, D. Eigler, and A. J. Heinrich, “Measurement of fast electron spin relaxation times with atomic resolution”, *Science* **329**, 1628–1630 (2010) 10.1126/science.1191688.
- ⁴⁰S. Loth, K. von Bergmann, M. Ternes, A. Otte, C. Lutz, and A. J. Heinrich, “Controlling the state of quantum spins with electric currents”, *Nat. Phys.* **6**, 340–344 (2010) 10.1038/nphys1616.
- ⁴¹W. Paul, K. Yang, S. Baumann, N. Romming, T. Choi, C. Lutz, and A. J. Heinrich, “Control of the millisecond spin lifetime of an electrically probed atom”, *Nat. Phys.* **13**, 403–407 (2017) 10.1038/nphys3965.
- ⁴²F. Natterer, F. Donati, F. Patthey, and H. Brune, “Thermal and magnetic-field stability of Holmium single-atom magnets”, *Phys. Rev. Lett.* **121**, 027201 (2018) 10.1103/PhysRevLett.121.027201.
- ⁴³K. Tao, V. Stepanyuk, W. Hergert, I. Rungger, S. Sanvito, and P. Bruno, “Switching a single spin on metal surfaces by a STM tip: ab initio studies”, *Phys. Rev. Lett.* **103**, 057202 (2009) 10.1103/PhysRevLett.103.057202.
- ⁴⁴S. Krause, G. Herzog, A. Schlenhoff, A. Sonntag, and R. Wiesendanger, “Joule heating and spin-transfer torque investigated on the atomic scale using a spin-polarized scanning tunneling microscope”, *Phys. Rev. Lett.* **107**, 186601 (2011) 10.1103/PhysRevLett.107.186601.

- ⁴⁵S. Loth, S. Baumann, C. Lutz, D. Eigler, and A. J. Heinrich, “Bistability in atomic-scale antiferromagnets”, *Science* **335**, 196 (2012) 10.1126/science.1214131.
- ⁴⁶A. Khajetoorians, B. Baxevanis, C. Hübner, T. Schlenk, S. Krause, T. Wehling, S. Lounis, A. Lichtenstein, D. Pfannkuche, J. Wiebe, and R. Wiesendanger, “Current-driven spin dynamics of artificially constructed quantum magnets”, *Science* **339**, 55–59 (2013) 10.1126/science.1228519.
- ⁴⁷F. Natterer, K. Yang, W. Paul, P. Willke, T. Choi, T. Greber, A. J. Heinrich, and C. Lutz, “Reading and writing single-atom magnets”, *Nature* **543**, 226–228 (2017) 10.1038/nature21371.
- ⁴⁸R. Baltic, M. Pivetta, F. Donati, C. Wäckerlin, A. Singha, J. Dreiser, S. Rusponi, and H. Brune, “Superlattice of single atom magnets on graphene”, *Nano Lett.* **16**, 7610–7615 (2016) 10.1021/acs.nanolett.6b03543.
- ⁴⁹F. Donati, S. Rusponi, S. Stepanow, C. Wäckerlin, A. Singha, L. Persichetti, R. Baltic, K. Diller, F. Patthey, E. Fernandes, J. Dreiser, Ž. Šljivančanin, K. Kummer, C. Nistor, P. Gambardella, and H. Brune, “Magnetic remanence in single atoms”, *Science* **352**, 318–321 (2016) 10.1126/science.aad9898.
- ⁵⁰R. Baltic, F. Donati, A. Singha, C. Wäckerlin, J. Dreiser, B. Delley, M. Pivetta, S. Rusponi, and H. Brune, “Magnetic properties of single rare-earth atoms on graphene/Ir(111)”, *Phys. Rev. B* **98**, 024412 (2018) 10.1103/PhysRevB.98.024412.
- ⁵¹F. Donati, S. Rusponi, S. Stepanow, L. Persichetti, A. Singha, D. M. Juraschek, C. Wäckerlin, R. Baltic, M. Pivetta, K. Diller, C. Nistor, J. Dreiser, K. Kummer, E. Velez-Fort, N. Spaldin, H. Brune, and P. Gambardella, “Unconventional spin relaxation involving localized vibrational modes in Ho single-atom magnets”, *Phys. Rev. Lett.* **124**, 077204 (2020) 10.1103/PhysRevLett.124.077204.
- ⁵²C. Wäckerlin, F. Donati, A. Singha, R. Baltic, S. Rusponi, K. Diller, F. Patthey, M. Pivetta, Y. Lan, and S. Klyatskaya, “Giant hysteresis of single-molecule magnets adsorbed on a nonmagnetic insulator”, *Adv. Mater.* **28**, 5195–5199 (2016) 10.1002/adma.201506305.
- ⁵³J. Dreiser, R. Westerström, C. Piamonteze, F. Nolting, S. Rusponi, H. Brune, S. Yang, A. Popov, L. Dunsch, and T. Greber, “X-ray induced demagnetization of single-molecule magnets”, *Appl. Phys. Lett.* **105**, 032411 (2014) 10.1063/1.4891485.
- ⁵⁴G. Binnig, H. Rohrer, C. Gerber, and E. Weibel, “Surface studies by scanning tunneling microscopy”, *Phys. Rev. Lett.* **49**, 57–61 (1982) 10.1103/PhysRevLett.49.57.
- ⁵⁵R. Young, J. Ward, and F. Scire, “Observation of metal-vacuum-metal tunneling, field emission, and the transition region”, *Phys. Rev. Lett.* **27**, 922–924 (1971) 10.1103/PhysRevLett.27.922.
- ⁵⁶R. Young, J. Ward, and F. Scire, “The topografiner: an instrument for measuring surface microtopography”, *Rev. Sci. Instrum.* **43**, 999–1011 (1972) 10.1063/1.1685846.
- ⁵⁷C. Chen, *Introduction to scanning tunneling microscopy* (Oxford University Press, 2021).
- ⁵⁸I. Amato, “Candid cameras for the nanoworld”, *Science* **276**, 1982–1985 (1997) 10.1126/science.276.5321.1982.

- ⁵⁹R. Wiesendanger, *Scanning probe microscopy and spectroscopy: methods and applications* (Cambridge University Press, 1994).
- ⁶⁰J. Fisher and I. Giaever, "Tunneling through thin insulating layers", *J. Appl. Phys.* **32**, 172–177 (1961) 10.1063/1.1735973.
- ⁶¹I. Giaever, "Energy gap in superconductors measured by electron tunneling", *Phys. Rev. Lett.* **5**, 147–148 (1960) 10.1103/PhysRevLett.5.147.
- ⁶²I. Giaever, "Electron tunneling between two superconductors", *Phys. Rev. Lett.* **5**, 464–466 (1960) 10.1103/PhysRevLett.5.464.
- ⁶³I. Giaever and K. Megerle, "Study of superconductors by electron tunneling", *Phys. Rev.* **122**, 1101–1111 (1961) 10.1103/PhysRev.122.1101.
- ⁶⁴I. Giaever, H. Hart, and K. Megerle, "Tunneling into superconductors at temperatures below 1°K", *Phys. Rev.* **126**, 941–948 (1962) 10.1103/PhysRev.126.941.
- ⁶⁵I. Giaever and H. Zeller, "Superconductivity of small tin particles measured by tunneling", *Phys. Rev. Lett.* **20**, 1504–1507 (1968) 10.1103/PhysRevLett.20.1504.
- ⁶⁶I. Giaever, "Electron tunneling and superconductivity", *Rev. Mod. Phys.* **46**, 245–250 (1974) 10.1103/RevModPhys.46.245.
- ⁶⁷G. Gamow, "Zur Quantentheorie des Atomkernes", *Z. Physik* **51**, 204–212 (1928) 10.1007/BF01343196.
- ⁶⁸R. Fowler and L. Nordheim, "Electron emission in intense electric fields", *R. Soc.* **119**, 173–181 (1928) 10.1098/rspa.1928.0091.
- ⁶⁹J. Oppenheimer, "Three notes on the quantum theory of aperiodic effects", *Phys. Rev.* **31**, 66–81 (1928) 10.1103/PhysRev.31.66.
- ⁷⁰J. Bardeen, "Tunnelling from a many-particle point of view", *Phys. Rev. Lett.* **6**, 57–59 (1961) 10.1103/PhysRevLett.6.57.
- ⁷¹M. Cohen, L. Falicov, and J. Phillips, "Superconductive tunneling", *Phys. Rev. Lett.* **8**, 316–318 (1962) 10.1103/PhysRevLett.8.316.
- ⁷²J. Tersoff and D. Hamann, "Theory and application for the scanning tunneling microscope", *Phys. Rev. Lett.* **50**, 1998–2001 (1983) 10.1103/PhysRevLett.50.1998.
- ⁷³J. Tersoff and D. Hamann, "Theory of the scanning tunneling microscope", *Phys. Rev. B* **31**, 805–813 (1985) 10.1103/PhysRevB.31.805.
- ⁷⁴C. Chen, "Origin of atomic resolution on metal surfaces in scanning tunneling microscopy", *Phys. Rev. Lett.* **65**, 448–451 (1990) 10.1103/PhysRevLett.65.448.
- ⁷⁵R. Wiesendanger, "Spin mapping at the nanoscale and atomic scale", *Rev. Mod. Phys.* **81**, 1495–1550 (2009) 10.1103/RevModPhys.81.1495.
- ⁷⁶R. Laiho and H. Reittu, "Theory of scanning tunneling microscopy with spin-polarized electrons obtained from a semiconducting tip", *Surf. Sci.* **289**, 363–369 (1993) 10.1016/0039-6028(93)90667-9.

Bibliography

- ⁷⁷D. Wortmann, S. Heinze, P. Kurz, G. Bihlmayer, and S. Blügel, “Resolving complex atomic-scale spin structures by spin-polarized scanning tunneling microscopy”, *Phys. Rev. Lett.* **86**, 4132–4135 (2001) 10.1103/PhysRevLett.86.4132.
- ⁷⁸P. Tedrow and R. Meservey, “Spin-dependent tunneling into ferromagnetic nickel”, *Phys. Rev. Lett.* **26**, 192–195 (1971) 10.1103/PhysRevLett.26.192.
- ⁷⁹M. Jullière, “Tunneling between ferromagnetic-films”, *Phys. Lett. A* **54**, 225–226 (1975) 10.1016/0375-9601(75)90174-7.
- ⁸⁰M. Baibich, J. Broto, A. Fert, F. Van Dau, F. Petroff, P. Etienne, G. Creuzet, A. Friederich, and J. Chazelas, “Giant magnetoresistance of (001)Fe/(001)Cr magnetic superlattices”, *Phys. Rev. Lett.* **61**, 2472–2475 (1988) 10.1103/PhysRevLett.61.2472.
- ⁸¹G. Binasch, P. Grünberg, F. Saurenbach, and W. Zinn, “Enhanced magnetoresistance in layered magnetic structures with antiferromagnetic interlayer exchange”, *Phys. Rev. B* **39**, 4828–4830 (1989) 10.1103/PhysRevB.39.4828.
- ⁸²E. Gerstner, “Nobel Prize 2007: Fert and Grünberg”, *Nat. Phys.* **3**, 754–754 (2007) 10.1038/nphys779.
- ⁸³R. Wiesendanger, H. Güntherodt, G. Güntherodt, R. Gambino, and R. Ruf, “Observation of vacuum tunneling of spin-polarized electrons with the scanning tunneling microscope”, *Phys. Rev. Lett.* **65**, 247–250 (1990) 10.1103/PhysRevLett.65.247.
- ⁸⁴M. Bode, “Spin-polarized scanning tunnelling microscopy”, *Rep. Prog. Phys.* **66**, 523 (2003) 10.1088/0034-4885.
- ⁸⁵J. Stroscio and D. Eigler, “Atomic and molecular manipulation with the scanning tunneling microscope”, *Science* **254**, 1319–1326 (1991) 10.1126/science.254.5036.1319.
- ⁸⁶R. Celotta, S. Balakirsky, A. Fein, F. Hess, G. Rutter, and J. Stroscio, “Autonomous assembly of atomically perfect nanostructures using a scanning tunneling microscope”, *Rev. Sci. Instrum.* **85**, 121301 (2014) 10.1063/1.4902536.
- ⁸⁷D. Eigler and E. Schweizer, “Positioning single atoms with a scanning tunnelling microscope”, *Nature* **344**, 524–526 (1990) 10.1038/344524a0.
- ⁸⁸M. Crommie, C. Lutz, and D. Eigler, “Confinement of electrons to quantum corrals on a metal surface”, *Science* **262**, 218–220 (1993) 10.1126/science.262.5131.218.
- ⁸⁹L. Bartels, G. Meyer, and K. Rieder, “Basic steps of lateral manipulation of single atoms and diatomic clusters with a scanning tunneling microscope tip”, *Phys. Rev. Lett.* **79**, 697–700 (1997) 10.1103/PhysRevLett.79.697.
- ⁹⁰J. Kliewer, R. Berndt, and S. Crampin, “Scanning tunnelling spectroscopy of electron resonators”, *New J. Phys.* **3**, 22–22 (2001) 10.1088/1367-2630/3/1/322.
- ⁹¹K. Braun and K. Rieder, “Engineering electronic lifetimes in artificial atomic structures”, *Phys. Rev. Lett.* **88**, 096801 (2002) 10.1103/PhysRevLett.88.096801.
- ⁹²N. Nilius, T. Wallis, and W. Ho, “Development of one-dimensional band structure in artificial gold chains”, *Science* **297**, 1853–1856 (2002) 10.1126/science.1075242.

- ⁹³G. Nazin, X. Qiu, and W. Ho, “Atomic engineering of photon emission with a scanning tunneling microscope”, *Phys. Rev. Lett.* **90**, 216110 (2003) 10.1103/PhysRevLett.90.216110.
- ⁹⁴N. Nilus, T. Wallis, and W. Ho, “Building alloys from single atoms: AuPd chains on NiAl(110)”, *J. Phys. Chem. B* **108**, 14616–14619 (2004) 10.1021/jp049127r.
- ⁹⁵J. Stroscio and R. Celotta, “Controlling the dynamics of a single atom in lateral atom manipulation”, *Science* **306**, 242–247 (2004) 10.1126/science.1102370.
- ⁹⁶M. Ternes, C. Lutz, C. Hirjibehedin, F. Giessibl, and A. J. Heinrich, “The force needed to move an atom on a surface”, *Science* **319**, 1066–1069 (2008) 10.1126/science.1150288.
- ⁹⁷S. Fölsch, J. Yang, C. Nacci, and K. Kanisawa, “Atom-by-atom quantum state control in adatom chains on a semiconductor”, *Phys. Rev. Lett.* **103**, 096104 (2009) 10.1103/PhysRevLett.103.096104.
- ⁹⁸A. Khajetoorians, J. Wiebe, B. Chilian, and R. Wiesendanger, “Realizing all-spin-based logic operations atom by atom”, *Science* **332**, 1062–1064 (2011) 10.1126/science.1201725.
- ⁹⁹R. Gaisch, J. Gimzewski, B. Reihl, R. Schlittler, M. Tschudy, and W. Schneider, “Low-temperature ultra-high-vacuum scanning tunneling microscope”, *Ultramicroscopy* **42**, 1621 (1992) 10.1016/0304-3991(92)90495-6.
- ¹⁰⁰P. Forrester, T. Bilgeri, F. Patthey, H. Brune, and F. Natterer, “Antiferromagnetic MnNi tips for spin-polarized scanning probe microscopy”, *Rev. Sci. Instrum.* **89**, 123706 (2018) 10.1063/1.5042530.
- ¹⁰¹J. Coraux, A. N’Diaye, C. Busse, and T. Michely, “Structural coherency of graphene on Ir(111)”, *Nano Lett.* **8**, 565–570 (2008) 10.1021/nl0728874.
- ¹⁰²M. Pivetta, S. Rusponi, and H. Brune, “Direct capture and electrostatic repulsion in the self-assembly of rare-earth atom superlattices on graphene”, *Phys. Rev. B* **98**, 115417 (2018) 10.1103/PhysRevB.98.115417.
- ¹⁰³F. Natterer, F. Patthey, T. Bilgeri, P. Forrester, N. Weiss, and H. Brune, “Upgrade of a low-temperature scanning tunneling microscope for electron-spin resonance”, *Rev. Sci. Instrum.* **90**, 013706 (2019) 10.1063/1.5065384.
- ¹⁰⁴M. Born, W. Heisenberg, and P. Jordan, “Zur Quantenmechanik. II.”, *Zeits. f. Phys.* **35**, 557–615 (1926) 10.1007/BF01379806.
- ¹⁰⁵P. Dirac, “On the theory of quantum mechanics”, *Roy. Soc. Proc.* **112**, 661–677 (1926) 10.1098/rspa.1926.0133.
- ¹⁰⁶W. Heisenberg, “Mehrkörperproblem und Resonanz in der Quantenmechanik”, *Zeits. f. Phys.* **38**, 411–426 (1926) 10.1007/BF01397160.
- ¹⁰⁷M. Pryce, “A modified perturbation procedure for a problem in paramagnetism”, *Proc. Phys. Soc. A* **63**, 25–29 (1950) 10.1088/0370-1298/63/1/304.
- ¹⁰⁸S. Blundell, *Magnetism in condensed matter* (Oxford University Press, 2001).
- ¹⁰⁹R. Skomski, *Simple models of magnetism* (Oxford University Press, 2008).

Bibliography

- ¹¹⁰J. Coey, *Magnetism and magnetic materials* (Cambridge University Press, 2009).
- ¹¹¹K. Yang, W. Paul, F. Natterer, J. Lado, Y. Bae, P. Willke, T. Choi, A. Ferrón, J. Fernández-Rossier, A. J. Heinrich, and C. Lutz, “Tuning the exchange bias on a single atom from 1 mT to 10 T”, *Phys. Rev. Lett.* **122**, 227203 (2019) 10.1103/PhysRevLett.122.227203.
- ¹¹²K. Stevens, “Matrix elements and operator equivalents connected with the magnetic properties of rare earth ions”, *P. R. Soc. A* **65**, 209 (1952) 10.1088/0370-1298/65/3/308.
- ¹¹³M. Hutchings, *Point-charge calculations of energy levels of magnetic ions in crystalline electric fields*, Vol. **16**, Solid State Physics (1964), 227–273, 10.1016/S0081-1947(08)60517-2.
- ¹¹⁴J. Jensen and A. Mackintosh, *Rare earth magnetism: structures and excitations* (Oxford University Press, 1991).
- ¹¹⁵A. Abragam, *The principles of nuclear magnetism* (Clarendon Press, Oxford, 1961).
- ¹¹⁶R. Orbach, “Spin-lattice relaxation in rare-earth salts”, *Roy. Soc. Proc.* **264**, 458–484 (1961) 10.1098/rspa.1961.0211.
- ¹¹⁷A. Abragam and B. Bleaney, *Electron paramagnetic resonance of transition ions* (Clarendon Press, Oxford, 1970).
- ¹¹⁸E. Bartolomé, A. Arauzo, J. Luzón, J. Bartolomé, and F. Bartolomé, “Chapter 1 - magnetic relaxation of lanthanide-based molecular magnets”, in, Vol. 26, Handbook of Magnetic Materials (Elsevier, 2017), 1–289, 10.1016/bs.hmm.2017.09.002.
- ¹¹⁹D. Gatteschi, R. Sessoli, and J. Villain, *Molecular nanomagnets* (Oxford University Press, 2006).
- ¹²⁰M. Briganti, F. Santanni, L. Tesi, F. Totti, R. Sessoli, and A. Lunghi, “A complete *Ab Initio* view of Orbach and Raman spin-lattice relaxation in a Dysprosium coordination compound”, *J. Am. Chem. Soc.* **143**, 13633–13645 (2021) 10.1021/jacs.1c05068.
- ¹²¹E. Callen and H. Callen, “Magnetostriiction, forced magnetostriiction, and anomalous thermal expansion in ferromagnets”, *Phys. Rev.* **139**, A455–A471 (1965) 10.1103/PhysRev.139.A455.
- ¹²²F. Hartmann-Boutron, P. Politi, and J. Villain, “Tunneling and magnetic relaxation in mesoscopic molecules”, *Int. J. Mod. Phys. B* **10**, 2577–2637 (1996) 10.1142/S0217979296001148.
- ¹²³J. Villain, A. Würger, A. Fort, and A. Rettori, “Effet tunnel dans les systèmes magnétiques : de la description microscopique et déterministe à l’équation maîtresse”, *J. Phys. I* **7**, 1583–1594 (1997) 10.1051/jp1:1997156.
- ¹²⁴P. Politi, A. Rettori, F. Hartmann-Boutron, and J. Villain, “Tunneling in mesoscopic magnetic molecules”, *Phys. Rev. Lett.* **75**, 537–540 (1995) 10.1103/PhysRevLett.75.537.
- ¹²⁵A. Fort, A. Rettori, J. Villain, D. Gatteschi, and R. Sessoli, “Mixed quantum-thermal relaxation in Mn₁₂ acetate molecules”, *Phys. Rev. Lett.* **80**, 612–615 (1998) 10.1103/PhysRevLett.80.612.
- ¹²⁶M. Leuenberger and D. Loss, “Spin tunneling and phonon-assisted relaxation in Mn₁₂-acetate”, *Phys. Rev. B* **61**, 1286–1302 (2000) 10.1103/PhysRevB.61.1286.

- ¹²⁷E. Rastelli and A. Tassi, “Relaxation time of the nanomagnet Fe_4 ”, *Phys. Rev. B* **79**, 104415 (2009) 10.1103/PhysRevB.79.104415.
- ¹²⁸C. Cervetti, A. Rettori, M. Pini, A. Cornia, A. Repollés, F. Luis, M. Dressel, S. Rauschenbach, K. Kern, M. Burghard, and L. Bogani, “The classical and quantum dynamics of molecular spins on graphene”, *Nat. Mat.* **15**, 164–168 (2016) 10.1038/nmat4490.
- ¹²⁹A. Lunghi and S. Sanvito, “The limit of spin lifetime in solid-state electronic spins”, *J. Phys. Chem. Lett.* **11**, 6273–6278 (2020) 10.1021/acs.jpcllett.0c01681.
- ¹³⁰L. Falkovsky, “Phonon dispersion in graphene”, *J. Exp. Theor. Phys.* **105**, 397–403 (2007) 10.1134/S1063776107080122.
- ¹³¹J. Kondo, “Resistance minimum in dilute magnetic alloys”, *Progr. Theoret. Phys.* **32**, 37–49 (1964) 10.1143/PTP32.37.
- ¹³²J. Schrieffer and P. Wolff, “Relation between the Anderson and Kondo hamiltonians”, *Phys. Rev.* **149**, 491–492 (1966) 10.1103/PhysRev.149.491.
- ¹³³J. Appelbaum, “Exchange model of zero-bias tunneling anomalies”, *Phys. Rev.* **154**, 633–643 (1967) 10.1103/PhysRev.154.633.
- ¹³⁴J. Fernández-Rossier, “Theory of single-spin inelastic tunneling spectroscopy”, *Phys. Rev. Lett.* **102**, 256802 (2009) 10.1103/PhysRevLett.102.256802.
- ¹³⁵J. Fransson, “Spin inelastic electron tunneling spectroscopy on local spin adsorbed on surface”, *Nano Lett.* **9**, 2414–2417 (2009) 10.1021/nl901066a.
- ¹³⁶F. Delgado and J. Fernández-Rossier, “Spin dynamics of current-driven single magnetic adatoms and molecules”, *Phys. Rev. B* **82**, 134414 (2010) 10.1103/PhysRevB.82.134414.
- ¹³⁷M. Ternes, “Spin excitations and correlations in scanning tunneling spectroscopy”, *New J. Phys.* **17**, 063016 (2015) 10.1088/1367-2630/17/6/063016.
- ¹³⁸M. Ternes, “Probing magnetic excitations and correlations in single and coupled spin systems with scanning tunneling spectroscopy”, *Prog. Surf. Sci.* **92**, 83–115 (2017) 10.1016/j.progsurf.2017.01.001.
- ¹³⁹C. Zener, “Non-adiabatic crossing of energy levels”, *P. R. Soc. Lond. A-Conta* **137**, 696 (1932) 10.1098/rspa.1932.0165.
- ¹⁴⁰C. Busse, P. Lazić, R. Djemour, J. Coraux, T. Gerber, N. Atodiresei, V. Caciuc, R. Brako, A. N’Diaye, S. Blügel, J. Zegenhagen, and T. Michely, “Graphene on Ir(111): physisorption with chemical modulation”, *Phys. Rev. Lett.* **107**, 036101 (2011) 10.1103/PhysRevLett.107.036101.
- ¹⁴¹S. Hämmäläinen, M. Boneschanscher, P. Jacobse, I. Swart, K. Pussi, W. Moritz, J. Lahtinen, P. Liljeroth, and J. Sainio, “Structure and local variations of the graphene moiré on Ir(111)”, *Phys. Rev. B* **88**, 201406 (2013) 10.1103/PhysRevB.88.201406.
- ¹⁴²A. Curcella, D. Sblendorio, S. Rusponi, M. Pivetta, F. Patthey, and H. Brune, “Intra-atomic exchange driving the spin dynamics in rare-earth single-atom magnets”, *In preparation*. (2022).

Bibliography

- ¹⁴³S. Kasper, A. Ariciu, S. McAdams, H. Weihe, J. Bendix, F. Tuna, and S. Piligkos, "Toward molecular 4f single-ion magnet qubits", *J. Am. Chem. Soc.* **138**, 5801–5804 (2016) 10.1021/jacs.6b02702.
- ¹⁴⁴C. Goodwin, F. Ortu, D. Reta, N. Chilton, and D. Mills, "Molecular magnetic hysteresis at 60 Kelvin in Dysprosocenium", *Nature* **548**, 439–442 (2017) 10.1038/nature23447.
- ¹⁴⁵F. Guo, B. Day, Y. Chen, M. Tong, A. Mansikkamäki, and R. Layfield, "Magnetic hysteresis up to 80 Kelvin in a Dysprosium metallocene single-molecule magnet", *Science* **362**, 1400–1403 (2018) 10.1126/science.aav0652.
- ¹⁴⁶F. Donati, M. Pivetta, C. Wolf, A. Singha, C. Wäckerlin, R. Baltic, E. Fernandes, J. de Groot, A. Lamia, L. Persichetti, C. Nistor, J. Dreiser, A. Barla, P. Gambardella, H. Brune, and S. Rusponi, "Correlation between electronic configuration and magnetic stability in Dysprosium single atom magnets", *Nano. Lett.* **21**, 8266–8273 (2021) 10.1021/acs.nanolett.1c02744.
- ¹⁴⁷A. Singha, P. Willke, T. Bilgeri, X. Zhang, H. Brune, F. Donati, A. J. Heinrich, and T. Choi, "Engineering atomic-scale magnetic fields by Dysprosium single atom magnets", *Nat. Commun.* **12**, 4179 (2021) 10.1038/s41467-021-24465-2.
- ¹⁴⁸F. Liu, D. Krylov, L. Spree, S. Avdoshenko, N. Samoylova, M. Rosenkranz, A. Kostanyan, T. Greber, A. Wolter, B. Büchner, and A. Popov, "Single molecule magnet with an unpaired electron trapped between two lanthanide ions inside a fullerene", *Nat. Commun.* **8**, 16098 (2017) 10.1038/ncomms16098.
- ¹⁴⁹C. Gould, K. McClain, J. Yu, T. Groshens, F. Furche, B. Harvey, and J. Long, "Synthesis and magnetism of neutral, linear metallocene complexes of Terbium(II) and Dysprosium(II)", *J. Am. Chem. Soc.* **141**, 12967 (2019) 10.1021/jacs.9b05816.
- ¹⁵⁰V. Dubrovin, A. Popov, and S. Avdoshenko, "Magnetism in Ln molecular systems with 4f/valence-shell interplay (FV-magnetism)", *Chem. Commun.* **55**, 13963 (2019) 10.1039/C9CC06913E.
- ¹⁵¹R. Pederson, A. Wysocki, N. Mayhall, and K. Park, "Multireference ab initio studies of magnetic properties of Terbium-based single-molecule magnets", *J. Phys. Chem. A* **123**, 6996–7006 (2019) 10.1021/acs.jpca.9b03708.
- ¹⁵²V. Dubrovin, A. Popov, and S. Avdoshenko, "Valence electrons in lanthanide-based single-atom magnets: a paradigm shift in 4f-magnetism modeling and design", *Inorg. Chem. Front.* **8**, 2373–2384 (2021) 10.1039/D0QI01148G.
- ¹⁵³A. Delin, L. Fast, B. Johansson, J. Wills, and O. Eriksson, "Method for calculating valence stability in lanthanide systems", *Phys. Rev. Lett.* **79**, 4637–4640 (1997) 10.1103/PhysRevLett.79.4637.
- ¹⁵⁴F. Donati, L. Gragnaniello, A. Cavallin, F. Natterer, Q. Dubout, M. Pivetta, F. Patthey, J. Dreiser, C. Piamonteze, S. Rusponi, and H. Brune, "Tailoring the magnetism of Co atoms on graphene through substrate hybridization", *Phys. Rev. Lett.* **113**, 177201 (2014) 10.1103/PhysRevLett.113.177201.

- ¹⁵⁵F. Delgado, J. Palacios, and J. Fernández-Rossier, “Spin-transfer torque on a single magnetic adatom”, *Phys. Rev. Lett.* **104**, 026601 (2010) 10.1103/PhysRevLett.104.026601.
- ¹⁵⁶A. Sapozhnik, C. Luo, H. Ryll, F. Radu, M. Jourdan, H. Zabel, and H. Elmers, “Experimental determination of exchange constants in antiferromagnetic Mn₂Au”, *Phys. Rev. B* **97**, 184416 (2018) 10.1103/PhysRevB.97.184416.
- ¹⁵⁷S. Picozzi and A. Freeman, “Polarization reduction in half-metallic heusler alloys: the effect of point defects and interfaces with semiconductors”, *J. Phys. Condens. Matter* **19**, 315215 (2007) 10.1088/0953-8984/19/31/315215.
- ¹⁵⁸W. Ebenhöf, V. Ehlers, and J. Ferch, “Hyperfine-structure measurements on Dy¹⁶¹ and Dy¹⁶³”, *Zeits. f. Phys.* **200**, 84–92 (1967) 10.1007/BF01326084.
- ¹⁵⁹B. Thole, G. van der Laan, and G. Sawatzky, “Strong magnetic dichroism predicted in the $M_{4,5}$ X-ray absorption spectra of magnetic rare-earth materials”, *Phys. Rev. Lett.* **55**, 2086–2088 (1985) 10.1103/PhysRevLett.55.2086.
- ¹⁶⁰B. Thole, P. Carra, F. Sette, and G. van der Laan, “X-ray circular dichroism as a probe of orbital magnetization”, *Phys. Rev. Lett.* **68**, 1943–1946 (1992) 10.1103/PhysRevLett.68.1943.
- ¹⁶¹F. de Groot, “Multiplet effects in X-ray spectroscopy”, *Coord. Chem. Rev.* **249**, 31–63 (2005) 10.1016/j.ccr.2004.03.018.
- ¹⁶²E. Beaurepaire, H. Bulou, F. Scheurer, and J. Kappler, “Magnetism: a synchrotron radiation approach”, in, Vol. 697, Lecture Notes in Physics (Springer Berlin Heidelberg, 2006), 10.1016/bs.hmm.2017.09.002.
- ¹⁶³H. Brune and P. Gambardella, “Magnetism of individual atoms adsorbed on surfaces”, *Surf. Sci.* **603**, 1812–1830 (2009) 10.1016/j.susc.2008.11.055.
- ¹⁶⁴C. Piamonteze, U. Flechsig, S. Rusponi, J. Dreiser, J. Heidler, M. Schmidt, R. Wetter, M. Calvi, T. Schmidt, H. Pruchova, J. Krempasky, C. Quitmann, H. Brune, and F. Nolting, “X-treme beamline at SLS: X-ray magnetic circular and linear dichroism at high field and low temperature”, *J. Synchrotron Rad.* **19**, 661–674 (2012) 10.1107/S0909049512027847.
- ¹⁶⁵B. Uchoa, L. Yang, S. Tsai, N. Peres, and A. Castro Neto, “Orbital symmetry fingerprints for magnetic adatoms in graphene”, *New J. Phys.* **16**, 013045 (2014) 10.1088/1367-2630/16/1/013045.
- ¹⁶⁶B. Henke, J. Smith, and D. Attwood, “0.1–10-keV x-ray-induced electron emissions from solids—models and secondary electron measurements”, *J. Appl. Phys.* **48**, 1852–1866 (1977) 10.1063/1.323938.
- ¹⁶⁷B. Henke, J. Smith, and D. Attwood, “Secondary electron energy distributions for gold as excited by C K α (277 eV) and Al K α (1487 eV) X-rays”, *Appl. Phys. Lett.* **29**, 539–541 (1976) 10.1063/1.89176.
- ¹⁶⁸M. Bernstein and J. Smith, “Primary and secondary photoelectron yields induced by soft X-rays”, *IEEE Trans Nucl Sci* **26**, 4977–4983 (1979) 10.1109/TNS.1979.4330259.
- ¹⁶⁹B. Henke, J. Knauer, and K. Premaratne, “The characterization of X-ray photocathodes in the 0.1–10-keV photon energy region”, *J. Appl. Phys.* **52**, 1509–1520 (1981) 10.1063/1.329789.

- ¹⁷⁰H. Seiler, "Secondary electron emission in the scanning electron microscope", *J. Appl. Phys.* **54**, R1–R18 (1983) 10.1063/1.332840.
- ¹⁷¹J. Cazaux, "Correlation between the X-ray induced and the electron-induced electron emission yields of insulators", *J. Appl. Phys.* **89**, 8265–8272 (2001) 10.1063/1.1368867.
- ¹⁷²X. Zhang, C. Wolf, Y. Wang, H. Aubin, T. Bilgeri, P. Willke, A. J. Heinrich, and C. T., "Electron spin resonance of single iron phthalocyanine molecules and role of their non-localized spins in magnetic interactions", *Nat. Chem.* **14**, 59–65 (2022) 10.1038/s41557-021-00827-7.
- ¹⁷³G. Pacchioni, L. Gragnaniello, F. Donati, M. Pivetta, G. Autès, O. Yazyev, S. Rusponi, and H. Brune, "Multiplet features and magnetic properties of Fe on Cu(111): from single atoms to small clusters", *Phys. Rev. B* **91**, 235426 (2015) 10.1103/PhysRevB.91.235426.
- ¹⁷⁴S. McAdams, A. Ariciu, A. Kostopoulos, J. Walsh, and F. Tuna, "Molecular single-ion magnets based on lanthanides and actinides: design considerations and new advances in the context of quantum technologies", *Coord. Chem. Rev.* **346**, 216–239 (2017) 10.1016/j.ccr.2017.03.015.
- ¹⁷⁵P. Forrester, F. Patthey, E. Fernandes, D. Sblendorio, H. Brune, and F. Natterer, "Quantum state manipulation of single atom magnets using the hyperfine interaction", *Phys. Rev. B* **100**, 180405(R) (2019) 10.1103/PhysRevB.100.180405.
- ¹⁷⁶E. Fernandes, F. Donati, F. Patthey, S. Stavrić, Ž. Šljivančanin, and H. Brune, "Adsorption sites of individual metal atoms on ultrathin MgO(100) films", *Phys. Rev. B* **96**, 045419 (2017) 10.1103/PhysRevB.96.045419.
- ¹⁷⁷A. Agresti and B. Coull, "Approximate is better than "exact" for interval estimation of binomial proportions", *Am. Stat.* **52**, 119–126 (1998) 10.2307/2685469.
- ¹⁷⁸Y. Chen, J. Liu, W. Wernsdorfer, D. Liu, L. Chibotaru, X. Chen, and M. Tong, "Hyperfine-interaction-driven suppression of quantum tunneling at zero field in a Holmium(III) single-ion magnet", *Angew. Chem. Int. Ed.* **56**, 4996–5000 (2017) 10.1002/anie.201701480.
- ¹⁷⁹S. Stoll and A. Schweiger, "EasySpin, a comprehensive software package for spectral simulation and analysis in EPR", *J. Magn. Reson.* **178**, 42–55 (2006) 10.1016/j.jmr.2005.08.013.
- ¹⁸⁰M. Shiddiq, D. Komijani, Y. Duan, A. Gaita-Ariño, E. Coronado, and S. Hill, "Enhancing coherence in molecular spin qubits via atomic clock transitions", *Nature* **531**, 348–351 (2016) 10.1038/nature16984.
- ¹⁸¹N. Ishikawa, M. Sugita, and W. Wernsdorfer, "Nuclear spin driven quantum tunneling of magnetization in a new lanthanide single-molecule magnet: Bis(Phthalocyaninato)Holmium anion", *J. Am. Chem. Soc.* **127**, 3650–3651 (2005) 10.1021/ja0428661.
- ¹⁸²R. Giraud, W. Wernsdorfer, A. Tkachuk, D. Mailly, and B. Barbara, "Nuclear spin driven quantum relaxation in $\text{LiY}_{0.998}\text{Ho}_{0.002}\text{F}_4$ ", *Phys. Rev. Lett.* **87**, 057203 (2001) 10.1103/PhysRevLett.87.057203.
- ¹⁸³A. Singha, D. Sostina, C. Wolf, S. Ahmed, D. Krylov, L. Colazzo, P. Gargiani, S. Agrestini, W. Noh, J. Park, M. Pivetta, S. Rusponi, H. Brune, A. J. Heinrich, A. Barla, and F. Donati, "Mapping orbital-resolved magnetism in single lanthanide atoms", *ACS Nano* **15**, 16162–16171 (2021) 10.1021/acsnano.1c05026.

- ¹⁸⁴M. Beg, “Debye temperature of MgO powder by elastic neutron scattering”, *Acta Crystallogr. A* **32**, 154–156 (1976).
- ¹⁸⁵T. Strandberg, C. Canali, and A. MacDonald, “Transition-metal dimers and physical limits on magnetic anisotropy”, *Nat. Mater.* **6**, 648–651 (2007) 10.1038/nmat1968.
- ¹⁸⁶H. Johll, H. Kang, and E. Tok, “Density functional theory study of Fe, Co, and Ni adatoms and dimers adsorbed on graphene”, *Phys. Rev. B* **79**, 245416 (2009) 10.1103/PhysRevB.79.245416.
- ¹⁸⁷R. Xiao, D. Fritsch, M. Kuz'min, K. Koepernik, H. Eschrig, M. Richter, K. Vietze, and G. Seifert, “Co dimers on hexagonal carbon rings proposed as subnanometer magnetic storage bits”, *Phys. Rev. Lett.* **103**, 187201 (2009) 10.1103/PhysRevLett.103.187201.
- ¹⁸⁸R. Xiao, D. Fritsch, M. Kuz'min, K. Koepernik, M. Richter, K. Vietze, and G. Seifert, “Prediction of huge magnetic anisotropies of transition-metal dimer-benzene complexes from density functional theory calculations”, *Phys. Rev. B* **82**, 205125 (2010) 10.1103/PhysRevB.82.205125.
- ¹⁸⁹R. Xiao, D. Fritsch, M. Kuz'min, K. Koepernik, and M. Richter, “CoIr-carbon complexes with magnetic anisotropies larger than 0.2 eV: a density functional-theory prediction”, *Appl. Phys. Lett.* **97**, 232501 (2010) 10.1063/1.3520488.
- ¹⁹⁰P. Błoński and J. Hafner, “Magnetic anisotropy of heteronuclear dimers in the gas phase and supported on graphene: relativistic density-functional calculations”, *J. Condens. Matter Phys.* **26**, 146002 (2014) 10.1088/0953-8984/26/14/146002.
- ¹⁹¹P. Błoński and J. Hafner, “Cu(111) supported graphene as a substrate for magnetic dimers with a large magnetic anisotropy: relativistic density-functional calculations”, *J. Condens. Matter Phys.* **26**, 256001 (2014) 10.1088/0953-8984/26/25/256001.
- ¹⁹²J. Li, H. Wang, J. Hu, and R. Wu, “Search for giant magnetic anisotropy in transition-metal dimers on defected hexagonal boron nitride sheet”, *Chem. Phys.* **144**, 204704 (2016) 10.1063/1.4950952.
- ¹⁹³K. Zhang, Y. Li, Y. Liu, Y. Zhu, and L. Shi, “Giant magnetic anisotropy of rare-earth adatoms and dimers adsorbed by graphene oxide”, *Phys. Chem. Chem. Phys.* **19**, 13245 (2017) 10.1039/C7CP01641G.
- ¹⁹⁴X. Liang, X. Wu, J. Hu, J. Zhao, and X. Zeng, “Large magnetic anisotropy in chemically engineered iridium dimer”, *Commun. Phys.* **1**, 74 (2018) 10.1038/s42005-018-0078-4.
- ¹⁹⁵K. Zhang, Y. Li, Y. Liu, and Y. Zhu, “Prediction of quantum anomalous Hall effect and giant magnetic anisotropy in graphene with adsorbed Ir-based dimers”, *J. Appl. Phys.* **125**, 193903 (2019) 10.1063/1.5087927.
- ¹⁹⁶W. Zhang, A. Muhtadi, N. Iwahara, L. Ungur, and L. Chibotaru, “Magnetic anisotropy in divalent lanthanide compounds”, *Angew. Chem. Int. Ed.* **59**, 12720–12724 (2020) 10.1002/anie.202003399.
- ¹⁹⁷D. Wang, R. Wu, and A. Freeman, “First-principles theory of surface magnetocrystalline anisotropy and the diatomic-pair model”, *Phys. Rev. B* **47**, 14932–14947 (1993) 10.1103/PhysRevB.47.14932.

Bibliography

- ¹⁹⁸J. Hu and R. Wu, “Control of the magnetism and magnetic anisotropy of a single-molecule magnet with an electric field”, *Phys. Rev. Lett.* **110**, 097202 (2013) 10.1103/PhysRevLett.110.097202.
- ¹⁹⁹P. Błoński, A. Lehnert, S. Dennler, S. Rusponi, M. Etzkorn, G. Moulas, P. Bencok, P. Gambardella, H. Brune, and J. Hafner, “Magnetocrystalline anisotropy energy of Co and Fe adatoms on the (111) surfaces of Pd and Rh”, *Phys. Rev. B* **81**, 104426 (2010) 10.1103/PhysRevB.81.104426.
- ²⁰⁰P. Błoński and J. Hafner, “Geometric and magnetic properties of Pt clusters supported on graphene: relativistic density-functional calculations”, *J. Chem. Phys.* **134**, 154705 (2011) 10.1063/1.3577517.
- ²⁰¹C. Rao, K. Gopalakrishnan, and A. Govindaraj, “Synthesis, properties and applications of graphene doped with boron, nitrogen and other elements”, *Nano Today* **9**, 324–343 (2014) 10.1016/j.nantod.2014.04.010.
- ²⁰²M. Corso, W. Auwärter, M. Muntwiler, A. Tamai, T. Greber, and J. Osterwalder, “Boron nitride nanomesh”, *Science* **303**, 217–220 (2004) 10.1126/science.1091979.
- ²⁰³A. Preobrajenski, A. Vinogradov, and N. Mårtensson, “Monolayer of *h*-BN chemisorbed on Cu(111) and Ni(111): the role of the transition metal 3d states”, *Surf. Sci.* **582**, 21–30 (2005) 10.1016/j.susc.2005.02.047.
- ²⁰⁴M. Morscher, M. Corso, T. Greber, and J. Osterwalder, “Formation of single layer *h*-BN on Pd(111)”, *Surf. Sci.* **600**, 3280–3284 (2006) 10.1016/j.susc.2006.06.016.
- ²⁰⁵A. Preobrajenski, M. Nesterov, M. Ng, A. Vinogradov, and N. Mårtensson, “Monolayer *h*-BN on lattice-mismatched metal surfaces: on the formation of the nanomesh”, *Chem. Phys. Lett.* **446**, 119–123 (2007) 10.1016/j.cplett.2007.08.028.
- ²⁰⁶A. Goriachko, M. Knapp, H. Over, M. Corso, T. Brugger, S. Berner, J. Osterwalder, and T. Greber, “Self-assembly of a hexagonal boron nitride nanomesh on Ru(0001)”, *Langmuir* **23**, 2928–2931 (2007) 10.1021/la062990t.
- ²⁰⁷E. Čavar, R. Westerström, A. Mikkelsen, E. Lundgren, A. Vinogradov, M. Ng, A. Preobrajenski, A. Zakharov, and N. Mårtensson, “A single *h*-BN layer on Pt(111)”, *Surf. Sci.* **602**, 1722–1726 (2008) 10.1016/j.susc.2008.03.008.
- ²⁰⁸F. Natterer, F. Patthey, and H. Brune, “Resonant-enhanced spectroscopy of molecular rotations with a scanning tunneling microscope”, *ACS Nano* **8**, 7099 (2014) 10.1021/nn501999k.
- ²⁰⁹Q. Dubout, F. Calleja, G. Sclauzero, M. Etzkorn, A. Lehnert, L. Claude, M. Papagno, F. D. Natterer, F. Patthey, S. Rusponi, A. Pasquarello, and H. Brune, “Giant apparent lattice distortions in STM images of corrugated sp^2 -hybridised monolayers”, *N. J. Phys.* **18**, 103027 (2016) 10.1088/1367-2630/18/10/103027.

- ²¹⁰F. Murzakhanov, B. Yavkin, G. Mamin, S. Orlinskii, I. Mumdzhi, I. Gracheva, B. Gabbasov, A. Smirnov, V. Davydov, and V. Soltamov, "Creation of negatively charged boron vacancies in hexagonal boron nitride crystal by electron irradiation and mechanism of inhomogeneous broadening of boron vacancy-related spin resonance lines", *J. Nanomater.* **11**, 1373 (2021) 10.3390/nano11061373.
- ²¹¹C. Linton, D. Gaudet, and H. Schall, "Laser spectroscopy of dysprosium monoxide: observation and analysis of several low-lying electronic states", *J. Mol. Spectrosc.* **115**, 58–73 (1986) 10.1016/0022-2852(86)90275-4.
- ²¹²M. Leetmaa and N. Skorodumova, "KMCLib: a general framework for lattice kinetic monte carlo (KMC) simulations", *Comput. Phys. Commun.* **185**, 2340–2349 (2014) 10.1016/j.cpc.2014.04.017.
- ²¹³O. Yazyev and A. Pasquarello, "Metal adatoms on graphene and hexagonal boron nitride: towards rational design of self-assembly templates", *Phys. Rev. B* **82**, 045407 (2010) 10.1103/PhysRevB.82.045407.
- ²¹⁴H. Brune, "Microscopic view of epitaxial metal growth: nucleation and aggregation", *Surf. Sci.* **31**, 125–229 (1998) 10.1016/S0167-5729(99)80001-6.
- ²¹⁵K. Fichtorn, M. Merrick, and M. Scheffler, "A kinetic Monte Carlo investigation of island nucleation and growth in thin-film epitaxy in the presence of substrate-mediated interactions", *Appl. Phys. A* **75**, 17–23 (2002) 10.1007/s003390101051.
- ²¹⁶H. Ding, V. Stepanyuk, P. Ignatiev, N. Negulyaev, L. Niebergall, M. Wasniowska, C. Gao, P. Bruno, and J. Kirschner, "Self-organized long-period adatom strings on stepped metal surfaces: scanning tunneling microscopy, *ab initio* calculations, and kinetic Monte Carlo simulations", *Phys. Rev. B* **76**, 033409 (2007) 10.1103/PhysRevB.76.033409.
- ²¹⁷N. Negulyaev, V. Stepanyuk, W. Hergert, P. Bruno, and J. Kirschner, "Atomic-scale self-organization of Fe nanostripes on stepped Cu(111) surfaces: molecular dynamics and kinetic Monte Carlo simulations", *Phys. Rev. B* **77**, 085430 (2008) 10.1103/PhysRevB.77.085430.
- ²¹⁸X. Zhang, B. Miao, L. Sun, C. Gao, A. Hu, H. Ding, and J. Kirschner, "Atomic superlattice formation mechanism revealed by scanning tunneling microscopy and kinetic Monte Carlo simulations", *Phys. Rev. B* **81**, 125438 (2010) 10.1103/PhysRevB.81.125438.
- ²¹⁹R. Cao, X. Zhang, B. Miao, Z. Zhong, L. Sun, B. You, A. Hu, and H. Ding, "Self-organized Gd atomic superlattice on Ag(111): scanning tunneling microscopy and kinetic Monte Carlo simulations", *Surf. Sci.* **610**, 65–69 (2013) 10.1016/j.susc.2013.01.008.
- ²²⁰H. Brune, J. Wintterlin, R. Behm, and G. Ertl, "Surface migration of "hot" adatoms in the course of dissociative chemisorption of oxygen on Al(111)", *Phys. Rev. Lett.* **68**, 624–626 (1992) 10.1103/PhysRevLett.68.624.
- ²²¹H. Brune, J. Wintterlin, J. Trost, G. Ertl, J. Wiechers, and R. Behm, "Interaction of oxygen with Al(111) studied by scanning tunneling microscopy", *Chem. Phys.* **99**, 2128–2148 (1993) 10.1063/1.465278.

- ²²²S. Wang and G. Ehrlich, “Atom condensation on an atomically smooth surface: Ir, Re, W, and Pd on Ir(111)”, *Chem. Phys.* **94**, 4071–4074 (1991) 10.1063/1.460657.
- ²²³G. Ehrlich and W. Fumiya, “Atomic interactions on crystals: a review of quantitative experiments”, *Langmuir* **7**, 2555–2563 (1991) 10.1021/la00059a027.
- ²²⁴L. Gao, J. Guest, and N. Guisinger, “Epitaxial graphene on Cu(111)”, *Nano Lett.* **10**, 3512–3516 (2010) 10.1021/nl1016706.
- ²²⁵Y. Ogawa, B. Hu, C. Orofeo, M. Tsuji, K. Ikeda, S. Mizuno, H. Hibino, and H. Ago, “Domain structure and boundary in single-layer graphene grown on Cu(111) and Cu(100) films”, *J. Phys. Chem. Lett.* **3**, 219–226 (2012) 10.1021/jz2015555.
- ²²⁶H. Ago, K. Kawahara, Y. Ogawa, S. Tanoue, M. Bissett, M. Tsuji, H. Sakaguchi, R. Koch, F. Fromm, T. Seyller, K. Komatsu, and K. Tsukagoshi, “Epitaxial growth and electronic properties of large hexagonal graphene domains on Cu(111) thin film”, *Appl. Phys. Express* **6**, 075101 (2013) 10.7567/apex.6.075101.
- ²²⁷B. Li, D. Luo, L. Zhu, X. Zhang, S. Jin, M. Huang, F. Ding, and R. Ruoff, “Orientation-dependent strain relaxation and chemical functionalization of graphene on a Cu(111) foil”, *Adv. Mater.* **30**, 1706504 (2018) 10.1002/adma.201706504.
- ²²⁸F. Natterer, S. Rusponi, M. Papagno, C. Carbone, and H. Brune, “Optimizing long-range order, band gap, and group velocities for graphene on close-packed metal surfaces”, *J. Phys.: Condens. Matter* **24**, 314203 (2012) 10.1088/0953-8984/24/31/314203.
- ²²⁹J. Wintterlin and M. Bocquet, “Graphene on metal surfaces”, *Surf. Sci.* **603**, 1841–1852 (2009) 10.1016/j.susc.2008.08.037.
- ²³⁰P. Sutter, J. Sadowski, and E. Sutter, “Graphene on Pt(111): growth and substrate interaction”, *Phys. Rev. B* **80**, 245411 (2009) 10.1103/PhysRevB.80.245411.
- ²³¹P. Merino, M. Švec, A. Pinardi, G. Otero, and J. Martín-Gago, “Strain-driven moiré superstructures of epitaxial graphene on transition metal surfaces”, *ACS Nano* **5**, 5627–5634 (2011) 10.1021/nn201200j.
- ²³²M. Iannuzzi, I. Kalichava, H. Ma, S. Leake, H. Zhou, G. Li, Y. Zhang, O. Bunk, H. Gao, J. Hutter, P. Willmott, and T. Greber, “Moiré beatings in graphene on Ru(0001)”, *Phys. Rev. B* **88**, 125433 (2013) 10.1103/PhysRevB.88.125433.
- ²³³H. Tetlow, J. Posthuma de Boer, I. Ford, D. Vvedensky, J. Coraux, and L. Kantorovich, “Growth of epitaxial graphene: theory and experiment”, *Phys. Rep.* **542**, 195–295 (2014) 10.1016/j.physrep.2014.03.003.
- ²³⁴M. Petrović, P. Lazić, S. Runte, T. Michely, C. Busse, and M. Kralj, “Moiré-regulated self-assembly of Cesium adatoms on epitaxial graphene”, *Phys. Rev. B* **96**, 085428 (2017) 10.1103/PhysRevB.96.085428.
- ²³⁵B. Barker, A. Bradley, M. Ugeda, S. Coh, A. Zettl, M. Crommie, S. Louie, and M. Cohen, “Geometry and electronic structure of Iridium adsorbed on graphene”, *Phys. Rev. B* **99**, 075431 (2019) 10.1103/PhysRevB.99.075431.

Dante Philippe Sblendorio · San Diego, CA · +41 78 977 89 79 · d.sblend@gmail.com

Education

École Polytechnique Fédérale de Lausanne (EPFL) - Lausanne, VD, CH <i>Ph.D. in Physics</i> Dissertation: Magnetic Properties of Surface Adsorbed Metal Adatoms and Dimers	July 2022
Collegio Carlo Alberto (CCA) - Turin, TO, Italy <i>M.Sc. in Data Science for Complex Economic Systems</i>	May 2018
Loyola Marymount University (LMU) – Los Angeles, CA, USA <i>B.S. in Physics, Minor in Applied Mathematics, Philosophy</i> Thesis: Planar Array Field Assisted Positron Moderation	May 2014

Experience

Laboratory of Nanostructures at Surfaces, EPFL <i>Graduate Researcher for Prof. Harald Brune</i>	2018 - 22 Lausanne, VD, CH
<ul style="list-style-type: none">• Maintained and operated home-built low temperature (4K) scanning tunneling microscope (STM) to investigate the magnetic properties of single atoms and dimers adsorbed on insulating surfaces.• Utilized chemical vapor deposition (CVD) and physical vapor deposition (PVD) techniques to prepare various insulating thin films on single-crystal substrates.• Modelled spin dynamics of single-atom magnets using QuTip package in Python to determine relevant relaxation pathways and influence of electron and phonon scattering on spin lifetimes.	
Fixate IO, LLC <i>Subject Matter Expert</i>	2017 – 22 Remote
<ul style="list-style-type: none">• Authored 20+ peer-reviewed technical articles and tutorials on using Python for ML, AI, NLP, finance, data visualization and automation applications. Relevant code can be found at https://gitlab.com/dsblendio.• Sourced and processed data from APIs, databases, or analog detectors/satellites directly. Developed ML/AI models in Python for urban air pollution, solar weather, NFL and NCAA game outcomes, and more. Utilized classification, regression, clustering, neural net and time-series analysis techniques.	
Positron Dynamics, Inc. <i>Lead Experimentalist & Manager</i>	2013 - 17 Livermore, CA, USA
<ul style="list-style-type: none">• Managed 4-6 person teams. Oversaw multiple simultaneous experiments from design stages to analysis of results. Presented results to executives.• Authored Positron Dynamics' Radioactive Safety Program. Ensured program followed strict U.S. Nuclear Regulatory Commission standards and limits. Implemented safety and training program to all employees.• Designed and maintained experiments in antimatter cooling & capture. Developed and constructed Time-of-Flight mass spectrometer for deuterium cluster investigation. Handled radioactive material for antimatter production.• Designed & built optics system for a 24W Nd:YAG laser. Developed safety and training program.• Co-authored proposals for grants & small business vouchers from various governmental agencies.• Authored analysis programs in MATLAB, Python, & R for rapid signal processing and data analysis.• Successfully pitched to several venture capitalist firms. Resulted in \$200k investment.	

Skills

Computational: Python (<i>TensorFlow, pandas, scikit-learn, Matplotlib, SciPy, NumPy</i>), R, MATLAB
Technical: microscopy (STM, SP-STM), spectrometry (TOF-MS), spectroscopy (IETS), CNC milling, UHV maintenance, cryogenic systems, analog signal detection & processing, 3D CAD (Fusion360)

Publications

Selected Academic:

- **Sblendorio, D.** and Curcella, A. and Rusponi, S. and Pivetta, M. and Patthey, F. and Brune, H., *Intra-atomic exchange driving the spin dynamics in rare-earth single-atom magnets. In submission, 2022.*
- Forrester, P. and Patthey, F. and Fernandes, E. and **Sblendorio, D.** and Brune, H. and Natterer, F., *Quantum state manipulation of single atom magnets using the hyperfine interaction*, Phys.Rev.B, 2019

Selected Fixate IO articles (more can be found at www.activestate.com/blog/author/dantesblendorio/):

- [How to Predict NFL Winners with Python](#)
- [Predictive Modelling of Air Quality Using Python](#)
- [How to Build a Generative Adversarial Network to Identify Deepfakes](#)